Institute of Physics Polish Academy of Sciences

PhD thesis

Energy transfer mechanisms in stacks composed of a monolayer transition metal dichalcogenide and a Ruddlesden-Popper 2D perovskite

MSc Miriam Karpińska

Supervisors:

Prof. Paulina Plochocka-Maude

Dr hab. Łukasz Kłopotowski

Warsaw 2023

To My Wonderful Grandmother Basia
Dla Mojej Wspaniałej Babci Basi

Acknowledgements

I would like to express my gratitude to my partner Sebastian, my sister Wiktoria and my mother Urszula who always believed in me and without whom I would not be able to finish this dissertation.

I thank my two supervisors, Łukasz Kłopotowski and Paulina Plochocka, for introducing me to a wonderful world of physics and scientific work.

I thank my colleagues and teammates from the Institute of Physics Polish Academy of Sciences in Warsaw: Małgorzata Szymura, Magdalena Duda, Anna Borodziuk, Bożena Sikora, Pushkar Joshi, Adam Ćwilich, Piotr Baranowski, Wojciech Zaleszczyk, Piotr Wojnar, Zbigniew Adamus, Krzysztof Fronc, Paweł Czerwiński, Sergij Chusnutdinow, and from the National Laboratory of High Magnetic Fields in Toulouse: Nan Zhang, Joanna Urban, Nikodem Sokołowski, Jakub Jasiński, Katarzyna Posmyk, Shuli Wang, Mateusz Dyksik, Michał Baranowski, Krzysztof Gałkowski, Alessandro Surrente and Duncan K. Maude, for their kindness and help in measurements and fruitful discussions about physics.

I am also grateful to technicians and administration from the Institute of Physics Polish Academy of Sciences in Warsaw and from the National Laboratory of High Magnetic Fields in Toulouse for their support during my PhD studies.

Academic achievements

Publications

[1] M. Dyksik, M. Baranowski, A. Leblanc, A. Surrente, **M. Karpińska**, J. M. Urban, Ł. Kłopotowski, D. K. Maude, N. Mercier, and P. Plochocka, "Influence of oversized cations on electronic dimensionality of d-$MAPbI_3$ crystals", *J. Mater. Chem. C*, 2020, **8**, 7928-7934

[2] **M. Karpińska**, M. Liang, R. Kempt, K. Finzel, M. Kamminga, M. Dyksik, N. Zhang, C. Knodlseder, D. K. Maude, M. Baranowski, Ł. Kłopotowski, J. Ye, A. Kuc, and P. Plochocka, "Nonradiative Energy Transfer and Selective Charge Transfer in a $WS_2/(PEA)_2PbI_4$ Heterostructure", *ACS Applied Materials & Interfaces* 2021, **13**, 28, 33677-33684

[3] **M. Karpińska**, J. Jasiski, R. Kempt, J. D. Ziegler, H. Sansom, T. Taniguchi, K. Watanabe, H. J. Snaith, A. Surrente, M. Dyksik, D. K. Maude, Ł. Kłopotowski, A. Chernikov, A. Kuc, M. Baranowski, and P. Plochocka, "Interlayer excitons in $MoSe_2$/2D perovskite hybrid heterostructures - the interplay between charge and energy transfer", *Nanoscale* 2022, **14**, 8085-8095

[4] M. Szymura, M. Duda, **M. Karpińska**, T. Kazimierczuk, R. Minikayev, K. Sobczak, M. Parlińska-Wojtan, and Ł. Kłopotowski, "Low-Temperature Photoluminescence Dynamics Reveal the Mechanism of Light Emission by Colloidal $CuInS_2$ Quantum Dots", *J. Phys. Chem. C* 2023, **127**, 14, 6768-6776

Oral presentation

[1] **M. Karpińska et al.**, "Mechanism of Electronic Coupling in Hybrid Transition Metal Dichalcogenide-2D Perovskite Heterostructures", nanoGe Spring Meeting 2022, 7 - 11 March 2022, Online

Poster presentation

[1] **M. Karpińska et al.**, "Photoluminescence Dynamics of Colloidal $CuInS_2$ Nanocrystals", 48th International School & Conference on the Physics of Semiconductors "Jaszowiec 2019", 8-14 June 2019, Szczyrk, Poland

[2] **M. Karpińska et al.**, "Mechanism of electronic coupling in a two-dimensional hybrid monolayer transition metal dichalcogenide/2D perovskite stack", Optics of Excitons in Confined Systems (OECS 17), August 30th - September 2nd 2021, Online

[3] **M. Karpińska et al.**, "Electronic coupling in hybrid monolayer transition metal dichalcogenide/2D perovskite heterostructures", 49th International School & Conference on the Physics of Semiconductors "Jaszowiec 2021", 1-10 September 2021, Online

Awards

[1] **Young Researcher Award** for poster presentation "Mechanism of electronic coupling in a two-dimensional hybrid monolayer transition metal dichalcogenide/2D perovskite stack", Optics of Excitons in Confined Systems OECS 17, August 30th - September 2nd 2021, Online

Abstract

For many decades, heterostructures (HS) have been used to build devices with desired properties. Initially, HS were grown by epitaxial techniques, which required that the lattice constants of the constituent materials have similar values. This severely limited the number of materials that could be used together. Following the discovery of graphene in 2004, a new type of HS composed of van der Waals materials has emerged. Offering a remarkable degree of flexibility due to the relaxed lattice constant matching requirement, van der Waals stacks have become excellent candidates for a new generation of optoelectronic devices.

One example of a phenomenon important for future applications is the excitation transfer between the layers of the constituent materials in the HS. This can occur via two main pathways: charge transfer (CT) or energy transfer (ET). In this thesis, I compare the results obtained in the optical spectroscopy experiments and theoretical calculations toward understanding the mechanism of excitation transfer in HS composed of two different van der Waals materials - a 2D hybrid organic-inorganic perovskite and a monolayer transition metal dichalcogenide (TMD). The investigated stacks include: PEA_2PbI_4/WS_2, where PEA stands for phenylethylammonium (PEPI/WS_2), $PEA_2PbI_4/MoSe_2$ (PEPI/$MoSe_2$), and $BA_2PbI_4/MoSe_2$, where BA is butylammonium (BAPI/$MoSe_2$).

The footprints of the excitation transfer in the investigated stacks were manifested in the photoluminescence (PL), reflectivity, PL excitation and time-resolved PL measurements. All the experiments were conducted at a temperature of 5 K. The CT was evidenced by monitoring the excess carrier concentration by estimating the charged-to-neutral exciton PL intensity ratio in TMD. The signatures of the ET were observed as resonances in the PL excitation spectra in TMD. According to the density functional theory calculations performed by a collaborating group from the University of Dresden, all three HS exhibit a particular type II band alignment, where the hole transfer between perovskite and TMD is allowed, while the electron transfer is blocked. Based on the comparison of the results obtained in the experiments and DFT calculations, I concluded that in PEPI/WS_2 and BAPI/$MoSe_2$ stacks, both CT and ET occur, while PEPI/$MoSe_2$ stack exhibited signatures of only CT.

The obtained results have shown that the specific excitation transfer pathway in 2D perovskite/TMD stacks can be closed or opened by simply using different organic spacer

compounds in a perovskite material. The easy manipulation of the excitation transfer holds great promise for future applications of these HS in novel, ultrathin electronics.

Streszczenie

Przez wiele dziesięcioleci heterostruktury (HS) były wykorzystywane do budowy urządzeń o ściśle określonych właściwościach. Początkowo HS wytwarzano głównie technikami epitaksjalnymi, w których materiały składowe musiały posiadać zbliżone wartości stałych sieciowych, co istotnie ograniczało liczbę materiałów, które mogły być użyte razem. Po przełomowym wyizolowaniu grafenu w 2004 roku, nowy rodzaj HS opartych na materiałach van der Waalsa stał się nowym tematem badań. W związku z tym, że w HS van der Waalsa warunek dopasowania stałych sieciowych nie musi być spełniony, okazały się być one doskonałymi kandydatami do nowej generacji urządzeń optoelektronicznych.

Jednym z przykładów procesu istotnego z punktu widzenia przyszłych zastosowań jest przekaz wzbudzenia między warstwami materiałów składowych heterostruktury. Może się on odbywać na drodze przekazu ładunku (CT) lub przekazu energii (ET). Celem niniejszej rozprawy doktorskiej było zbadanie mechanizmu przekazu wzbudzenia w HS złożonych z dwóch różnych materiałów van der Waalsa - dwuwymiarowych hybrydowych perowskitów organiczno-nieorganicznych i monowarstwowych dichalkogenków metali przejściowych (TMD). Przedstawioną analizę oparto na porównaniu wyników otrzymanych w eksperymentach spektroskopii optycznej z wynikami obliczeń w ramach teorii funkcjonału gęstości (DFT). W tej rozprawie zbadane zostały następujące HS: PEA_2PbI_4/WS_2, gdzie PEA oznacza fenyloetyloaminę (PEPI/WS_2), $PEA_2PbI_4/MoSe_2$ (PEPI/$MoSe_2$), oraz $BA_2PbI_4/MoSe_2$, gdzie BA oznacza butyloaminę (BAPI/$MoSe_2$).

Przejawy przekazu wzbudzenia w badanych strukturach zostały zaobserwowane w pomiarach fotoluminescencji (PL), odbicia, widm wzbudzenia PL oraz PL rozdzielonej czasowo. Wszystkie doświadczenia przeprowadzono w temperaturze 5 K. CT zaobserwowano monitorując koncentrację nadmiarowych nośników poprzez określenie stosunku intensywności PL ekscytonów naładowanych do ekscytonów neutralnych w TMD. Przejawami ET były rezonanse zaobserwowane w widmach wzbudzenia PL w TMD. Według obliczeń DFT przeprowadzonych na potrzebę tych eksperymentów przez współpracującą grupę z Politechniki w Dreźnie, wszystkie trzy HS wykazują szczególne ułożenie pasm typu II, umożliwiające przekaz dziur i blokujące przekaz elektronów pomiędzy warstwami perowskitu i TMD. Porównując wyniki otrzymane w eksperymencie z wynikami DFT stwierdzono, że

w strukturach PEPI/WS_2 i BAPI/$MoSe_2$ zachodzi zarówno CT jak i ET, podczas gdy próbka PEPI/$MoSe_2$ wykazywała tylko CT.

Uzyskane wyniki pokazały, że kanał przekazu wzbudzenia w HS złożonych z dwuwymiarego perowskitu i monowarstwy TMD można otworzyć bądź zamknąć poprzez zastosowanie konkretnych związków organicznych budujących perowskit. Łatwa kontrola przekazu wzbudzenia wskazuje na możliwość wykorzystania tych HS w nowoczesnych, ultracienkich urządzeniach elektronicznych.

Contents

Introduction

Motivation

The structures fabricated by putting together different materials are now employed in many devices that surround us, such as transistors or diodes [1, 2]. One of the most popular techniques of heterostructure fabrication is the molecular beam epitaxy (MBE), a method that allows the deposition of thin films with atomically flat surfaces. Unfortunately, the heterostructures obtained by means of MBE have one important limitation - the constituent materials must possess comparable lattice constants. The difference between the lattice constants should be smaller than around 5 % to 10 % [3]. Otherwise, tensile or compressive strain at the interface will lead to the formation of numerous structural defects that can significantly degrade the optical and electronic properties of the whole structure.

Following the isolation of graphene by mechanical exfoliation, van der Waals materials composed of atomically thin covalently-bonded layers connected by van der Waals interactions, become a hot topic of research [4]. It turned out that their heterostructures can be obtained by simply putting the exfoliated layers on top of each other. Owing to weak van der Waals interactions at the interface, the requirement of similar lattice constants is relaxed in van der Waals stacks [5–8]. This facilitates the stacking of different materials into heterostructures with novel and exotic phenomena, such as moiré excitons, spin-polarized spatially indirect excitons or superconductivity [8–11]. The van der Waals stacks show promise for various applications in light emitting diodes [6], photodetectors [12], solar cells [13], transistors [14], sensors [15], photocatalyst devices [16], and many more.

Recently, a new type of van der Waals stacks composed of metal-halide perovskites and group-VI semiconducting transition metal dichalcogenides (TMDs) has become an important center of interest in the scientific community [13, 17–21]. Combining perovskites with their easily tunable properties and TMDs with their unique valley-dependent physics could potentially enable their application in new spintronic or electronic devices.

Till now, the research of perovskite/TMD stacks focused mostly on device properties. In 2016, Ma et al. [22] fabricated a photodetector based on MAPI ($CH_3NH_3PbI_3$) perovskite film grown on monolayer WS_2. In this heterostructure with type II band alignment,

a charge transfer (CT) across the interface resulted in a reduced device dark current and increased photocurrent compared to the device based solely on WS_2. Since 2016, apart from photodetectors, numerous studies on perovskite/TMD-based devices have been reported in the literature, including field-effect transistors [19] and solar cells [13, 23, 24], some of which exhibited a power conversion efficiency of over 10 % [25, 26]. Apart from the research on the performance of devices, there is also a limited number of studies focused on the fundamental physics of perovskite/TMD heterostructures. In 2018, Li and collaborators [1] analyzed the mechanism of excitation transfer in type I $CsPbBr_3$ quantum dot/WS_2 stack. The energy transfer (ET) with an efficiency of ~ 40 % was manifested as an enhancement by a factor of 12 of the WS_2 emission intensity at room temperature. Recently, Zhang et al. [27] reported fast (around 100 fs) and efficient (efficiency over 95 %) CT in type II $CsPbBr_3$ film /monolayer MoS_2 stack. Both efficiency and carrier transfer rate were comparable to those observed in TMD/TMD van der Waals stacks [28, 29].

In this thesis, I will investigate the stacks composed of a particular group of the perovskite/TMD heterostructures composed of hybrid organic-inorganic 2D perovskites and monolayer TMDs. Despite being known for less than a decade, interesting physical phenomena have already been observed in the 2D perovskite/TMD stacks - such as upconversion [30] or spin transfer [31]. In order to develop efficient optoelectronic devices, the comprehension of the fundamental processes in the heterostructure is first necessary. Unfortunately, our understanding of physics in 2D perovskite/TMD stacks is still not satisfactory. For instance, no consensus about the mechanism of excitation transfer between the constituent materials has so far been reached [31–35]. In 2020, Wang and collaborators [35] reported that the PEA_2PbI_4/WS_2 stack (PEA stands for phenylethylammonium) exhibits type II band alignment, where the photoexcited electrons are transferred from perovskite to TMD. The CT was confirmed by around 5 times larger photoresponsivity of the PEA_2PbI_4 (PEPI)/WS_2-based device in comparison to the device based only on WS_2. In some of the 2D perovskite/TMD heterostructures, the CT was manifested in the form of interlayer excitons [31, 33, 34]. On the other hand, Zhang et al. [32] proposed that in PEPI/WS_2 stack, the mechanism governing the excitation transfer is the non-radiative energy transfer (ET) from the ground perovskite exciton state to the excited TMD exciton state. Interestingly, the authors postulated that multiple perovskite layers contribute to the ET process which results in a large factor of the WS_2 emission enhancement.

The presented above inconclusive results about the mechanism of excitation transfer in 2D perovskite/TMD stacks are the main motivation for this thesis. The goal of this work was to establish the mechanism of excitation transfer and the factors that could control it in 2D perovskite/TMD stacks. This investigation was conducted by means of optical spectroscopy

experiments at low temperature. Specifically, I will study the excitation transfer mechanism in PEPI/WS_2, PEPI/$MoSe_2$ and BA_2PbI_4 (BAPI)/$MoSe_2$ stacks. I will show that the novel band alignment that is not observed in typical TMD/TMD structures enables both CT and ET. I will also demonstrate that the mechanism of excitation transfer between 2D perovskite and TMD can be manipulated by the selection of the appropriate organic spacer compound in the perovskite layer.

Outline of this work

This thesis is composed of 7 Chapters.

In Chapter 1, I present a theoretical introduction to the subject of the thesis. I introduce the concept of excitons in 3D and 2D semiconducting materials. I discuss also the optoelectronic properties of the monolayer TMDs and 2D perovskites, and the main mechanisms of excitation transfer in van der Waals heterostructures.

In Chapter 2, I present the description of the chemical vapor deposition growth of monolayer WS_2, and the synthesis of PEPI and BAPI perovskite crystals. I also describe in detail the steps of the preparation of the PEPI/WS_2, PEPI/$Mose_2$ and BAPI/$MoSe_2$ stacks.

In Chapter 3, I discuss the optical spectroscopy experimental setups that were employed to investigate the properties of the stacks.

In Chapter 4, I study the excitonic transitions in the constituent materials in each heterostructure by means of reflectance (RL) and photoluminescence (PL) experiments. This investigation is complemented by the studies of each stack with an optical microscope.

In Chapter 5, I present the theoretical and experimental investigations of the optoelectronic properties of the PEPI/WS_2 van der Waals stack. First, I introduce the predictions of the band alignment based on first principle calculations. Then, I show the results of the spectroscopic studies at low temperature. Finally, I discuss the observed effects and interpret them by comparison with the theory.

In Chapter 6, I present the theoretical and experimental investigations of the optoelectronic properties of the PEPI/$MoSe_2$ and BAPI/$MoSe_2$ stacks. I discuss the results of the density functional theory calculations and compare them with the results of the steady-state and time-resolved optical measurements.

In Chapter 7, I summarize the results of the optical spectroscopic experiments in all the investigated van der Waals stacks.

Theoretical background

This Chapter consists of four Sections. In the first Section, I will present a theoretical description of the hydrogen model of Wannier-Mott excitons in 3D and 2D semiconductors. Then, I will discuss the crystal structure, band structure and optical properties of semiconducting monolayer TMDs and 2D hybrid lead-halide perovskites. Finally, I will introduce the main pathways of the excitation transfer, namely, photon reabsorption, charge transfer, and Dexter and Förster energy transfer.

1.1 Excitons in semiconductors

1.1.1 Introduction

The characteristic feature of a semiconductor material is the presence of an energy bandgap. The interband electronic transitions are allowed only when the absorbed energy is equal to or higher than the size of the bandgap. In the absorption of photons, the electrons are promoted from the valence band (VB) to the conduction band (CB), leaving behind holes. The attractive electrostatic forces between the electron and hole lead to the formation of a quasiparticle known as exciton. The concept of excitons in solid-state materials was introduced theoretically in 1931 by Yakov Frenkel [36] and the signatures of excitons were observed for the first time in cuprous oxide (Cu_2O) in 1950 [37].

There are two main types of excitons. The Frenkel excitons exhibit Bohr radii comparable to the size of a single unit cell in a crystal. The electron-hole interaction is strong, resulting in exciton binding energies on the order of 1 eV. The Frenkel excitons are usually observed in semiconductors with low dielectric constants, such as ionic organic crystals (e.g. anthracene) [38, 39]. The second type, Wannier-Mott excitons, can be found in most inorganic semiconductors (like GaAs or CdTe). Their Bohr radii (on the order of several nm) considerably exceed the size of a unit cell in a material. As the electrons and holes are loosely bound together, the binding energies of the Wannier-Mott excitons are much smaller

than those of Frenkel excitons. Usually, they are in the range of a few meV to a few tens meV [40, 41].

In the following subsections, I will introduce the hydrogen model of the Wannier-Mott excitons in 3D and 2D semiconductor materials.

1.1.2 Excitons in 3D semiconductors

The attractive interaction between the electron and hole is described by the Coulomb potential [42]:

$$V(\mathbf{r_e}, \mathbf{r_h}) = -\frac{e^2}{4\pi\epsilon_0\epsilon|\mathbf{r_e} - \mathbf{r_h}|}, \tag{1.1}$$

where ϵ_0 (ϵ) is a dielectric constant of a vacuum (material), and $\mathbf{r_e}$ and $\mathbf{r_h}$ are the position vectors of electron and hole, respectively. The Hamiltonian of such a system will have the following formula [42]:

$$\hat{H}^{3D} = \frac{-\hbar^2}{2m_e^*}\nabla_e^2 - \frac{\hbar^2}{2m_h^*}\nabla_h^2 + V(\mathbf{r_e}, \mathbf{r_h}), \tag{1.2}$$

where the first two components describe the kinetic energy of the electron in the CB and hole in the VB, respectively, m_e^* (m_h^*) is the effective mass of the electron (hole), ∇^2 is the Laplacian operator. The subscripts e and h correspond to the electron and hole coordinates, respectively.

In an analogy to the hydrogen atom model, the Schrodinger equation with Hamiltonian from Eq. 1.2 can be solved by introducing the center-of-mass $\mathbf{R}$ and relative mass $\mathbf{r}$ coordinates:

$$\mathbf{R} = \frac{m_e^*\mathbf{r_e} + m_h^*\mathbf{r_h}}{m_e^* + m_h^*}, \mathbf{r} = \mathbf{r_e} - \mathbf{r_h}. \tag{1.3}$$

In the hydrogen model, the motion of the exciton center-of-mass

$$M = m_e^* + m_h^* \tag{1.4}$$

is the motion of a free particle, while the relative motion of exciton is the motion of a particle with mass μ given by

$$\frac{1}{\mu} = \frac{1}{m_e^*} + \frac{1}{m_e^*} \tag{1.5}$$

in a Coulomb potential

$$V(\mathbf{r}) = -\frac{e^2}{4\pi\epsilon_0\epsilon\mathbf{r}}. \tag{1.6}$$

Two decoupled and easily solvable Schrödinger equations are now obtained:

$$\frac{-\hbar^2}{2M}\nabla_{\mathbf{R}}^2\psi(\mathbf{R}) = E_R\psi(\mathbf{R}) \tag{1.7}$$

$$\frac{-\hbar^2}{2\mu}\nabla^2_{\mathbf{r}}\phi(\mathbf{r}) = E_r\phi(\mathbf{r}). \tag{1.8}$$

The solution to these two equations is the exciton wavefunction:

$$\Psi_{nlm}(\mathbf{R},\mathbf{r}) = \mathrm{A}e^{i\mathbf{KR}}R_{nl}(\mathbf{r})Y_{lm}(\Theta,\Phi), \tag{1.9}$$

where A is a normalization constant and $\mathbf{K}$ is the exciton center-of-mass wavevector (which is the sum of the electron and hole wavevectors). The n, l and m are the principal, angular momentum and magnetic quantum numbers, respectively. The R_{nl} and $Y_{lm}(\Theta,\Phi)$ are the associated Laguerre polynomials and spherical harmonics, respectively. The exciton energy is expressed as [43]:

$$E_n(\mathbf{K}) = E_g + \frac{\hbar^2\mathbf{K}^2}{2M} - \frac{R^*}{n^2}, \tag{1.10}$$

where E_g is a material bandgap, the second term represents the kinetic energy of the exciton center-of-mass and R^* is the exciton Rydberg given by:

$$R^* = \frac{\mu e^4}{8(h\epsilon_0\epsilon)^2} = \frac{\mu}{m_0\epsilon^2}Ry, \tag{1.11}$$

where m_0 is an electron rest mass and Ry $= -13.6$ eV is a hydrogen Rydberg constant. According to Eq. 1.10, in 3D semiconductors the exciton binding energy (E_b) is equal to R*.

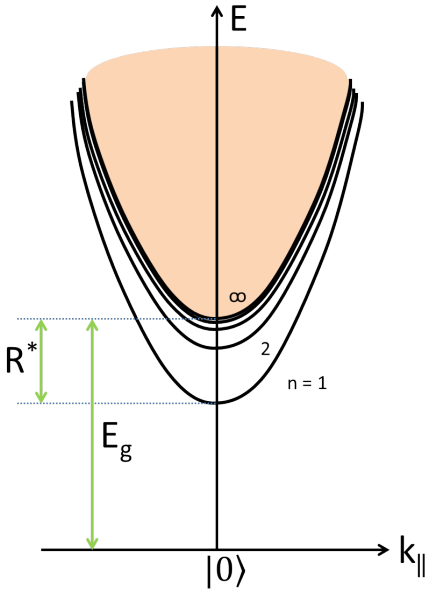

Figure 1.1: Schematic diagram showing the dispersion relations in 3D semiconductor for $n = 1$, 2 and 3 Wannier-Mott exciton states. The E_g is the energy bandgap. $|0\rangle$ denotes the ground state and $k_{\|}$ is the in-plane wavevector.

A schematic diagram showing $n = 1$, 2, 3 excitonic states in a bulk semiconductor is presented in Figure 1.1. In 3D materials, the exciton binding energy (e.g in GaAs

$\sim$ 4.9 meV, ZnTe $\sim$ 13 meV [41]) is usually smaller than thermal energy at room temperature ($\sim$ 25 meV). As the probability of exciton thermal dissociation is high, the excitonic transitions in bulk materials are usually observed only at low temperature.

1.1.3 Excitons in 2D semiconductors

When the dimensionality of 3D material is lowered to 2D, the excitons become confined to a plane of the potential well. Assuming an infinite quantum well structure, the 2D hydrogen model of excitons in the center-of-mass and relative coordinates is described by a Hamiltonian:

$$\hat{H}^{2D} = -\frac{\hbar^2 \nabla_{\mathbf{R_{2D}^2}}}{2M} - \frac{\hbar^2 \nabla_{\mathbf{r_{2D}^2}}}{2\mu} + V(\mathbf{r_{2D}}), \tag{1.12}$$

where $\mathbf{R_{2D}}$ and $\mathbf{r_{2D}}$ are the center-of-mass and relative coordinates in 2D, respectively, and $V(\mathbf{r_{2D}})$ is the Coulomb potential (see Eq. 1.6). By solving the Schrodinger equation with Hamiltonian from Eq. 1.12, the following exciton energy is obtained:

$$E_n(\mathbf{K}) = E_g + \frac{\hbar^2 \mathbf{K}^2}{2M} - \frac{R^*}{(n-1/2)^2}. \tag{1.13}$$

Therefore, the exciton binding energy in a 2D semiconductor is $E_b = 4R^*$, so it is 4 times larger than in a 3D semiconductor (Eq. 1.10) [40].

It is important to note that the exciton energy in atomically thin 2D materials usually deviates from the simple 2D hydrogen model. The discrepancies are, among others, caused by: dielectric screening [44] (this effect will be discussed in the subsequent part of this Chapter), band nonparabolicity [45], coupling to phonons [46] and exchange interactions [47].

1.2 Transition metal dichalcogenides

1.2.1 Introduction

In this thesis, I will focus on the subgroup of the 2D materials family, namely, the monolayer transition metal dichalcogenides (TMDs) with a general chemical formula MX_2, where M is a group-VI transition metal atom (W, Mo) and X is a chalcogen atom (S, Se). Despite being known for about a century [48], the numerous fascinating properties of TMDs and their great potential for applications have been discovered only in the last two decades. In 2010, Heinz and Wang groups [49, 50] have reported that monolayer MoS_2 exhibits strong emission intensity, undeniably proving that it is a direct bandgap semiconductor. A year later, Radisavljevic et al. [51] fabricated the first transistor based on monolayer MoS_2. At

room temperature, the device exhibited a large current on/off ratio ($\sim 10^8$), indicating good performance and low leakage power of the device. A promise for applications in ultrathin optoelectronic devices has quickly pushed forward the research of monolayer TMDs. This resulted in a discovery of many interesting physical phenomena that could be used in biosensors [52], energy storage devices [53], photonic devices [54], phototransistors [55], gas sensors [56], catalysts [57], and many more.

1.2.2 Crystal structure

The crystal structure of bulk TMD materials was described for the first time in 1923 by Dickinson and Pauling [48], who investigated a mineral of MoS_2 (known as molybdenite) with X-ray radiation.

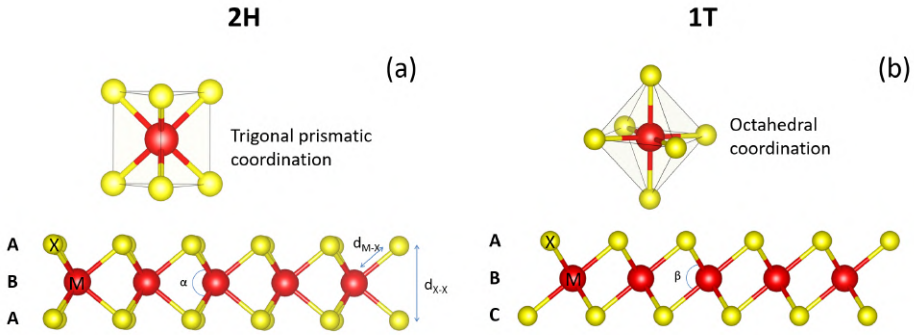

Figure 1.2: (a) - Geometry of trigonal prismatic coordination (top panel) and side view (bottom panel) in the 2H structure of monolayer TMDs. (b) - Geometry of octahedral coordination (top panel) and side view (bottom panel) in the 1T structure of monolayer TMDs. Red and yellow spheres represent the transition metal (M) and chalcogen atoms (X), respectively. d_{X-X} is the distance between chalcogen atoms from the subsequent atomic layers. d_{M-X} is the M-X bonding length. α and β denote the X-M-X bonding angle in 2H and 1T phase, respectively. The ABA and ABC denote different stacking sequences of the M and X sublattices. The crystal structures of the 2H and 1T phases are based on data from Ref. [58] and [59], respectively.

Monolayer TMDs are composed of a single layer of M atoms sandwiched between two layers of X atoms. They can crystallize in several structural polytypes in which M atoms are coordinated differently by chalcogens [60]. Two main crystal phases of monolayer TMDs are shown in Figure 1.2. In the thermodynamically stable honeycomb 2H phase, M atoms are coordinated by chalcogens in a trigonal prismatic geometry, as shown in the top panel in Figure 1.2 (a). The chalcogens from consecutive atomic sheets are aligned along the z-axis forming the ABA stacking sequence (where A indicates chalcogen and B - transition metal layer) [61, 62]. The ABA stacking is presented in the bottom panel in

Figure 1.2 (a). In contrast to the 2H phase, the 1T polytype is metastable. There are methods to obtain 1T monolayer TMDs (like intercalation with alkali metal cations - K^+, Li^+) but the proper stabilization (e.g. substitutional doping with Mn or Re) to prevent the transition to a more energetically favorable 2H phase has to be provided [63]. The 1T polytype exhibits octahedral M coordination which is presented in the top panel in Figure 1.2 (b). This coordination geometry results in a shift of X atoms from the subsequent layers along the x-axis, forming the ABC stacking sequence, as shown in the bottom panel in Figure 1.2 (b). Apart from distinct stacking ordering, in the 1T phase, the distance between chalcogens from neighboring layers is larger, whereas the angle of X-M-X bonding is smaller than in the 2H phase.

As will be discussed in the next subsection, the valence band maximum (VBM) and conduction band minimum (CBM) in monolayer TMDs is composed mainly of d orbitals of M atoms with a small contribution of p orbitals of X atoms [64–66]. The splitting of d orbitals strongly depends on the crystal phase symmetry and the TMDs can exhibit strikingly different electronic properties depending on the material polytype [67]. For instance, He and co-workers [68] have calculated that the 2H monolayer MoS_2 polytype is a direct bandgap semiconductor, whereas in the 1T phase, the bandgap disappears and MoS_2 exhibits metallic properties.

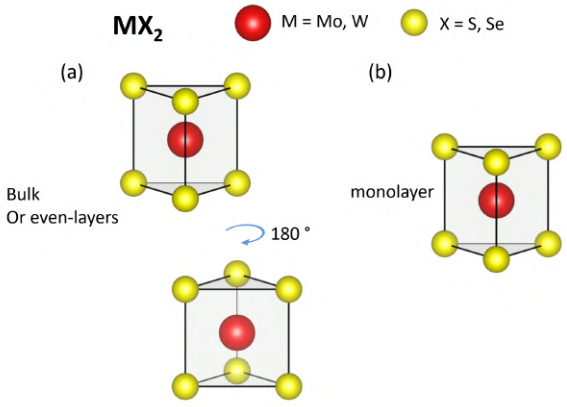

Figure 1.3: Atomic structure of the unit cell in (a) - bulk or even-layer and (b) - monolayer TMDs. Red and yellow spheres represent the transition metal and chalcogen atoms, respectively. Based on the crystal structure of 2H MoS_2 from Ref. [58].

In TMDs, the subsequent monolayers are rotated with respect to each other by 180° around the stacking axis, as presented in Figure 1.3 (a) [69, 70]. Therefore, in bulk and even-layer TMDs the crystal structure exhibits an inversion symmetry with the inversion center located between the subsequent monolayers. On the other hand, in the monolayer form (and other odd-layer TMDs), the inversion symmetry is broken which is clearly visible

in Figure 1.3 (b). The breaking of inversion symmetry in monolayer TMDs has an important impact on their electronic and optical properties as will be discussed in the following parts of this Chapter.

1.2.3 Band structure

The evolution of the TMD band structure from bulk to the monolayer form was analyzed theoretically [60, 64, 65, 71] and confirmed by experiment [72–74]. The schematic band structures in bulk and monolayer TMDs are presented in Figure 1.4 in the left and right panels, respectively. In bulk TMDs, the VBM is located at Γ high symmetry point, and the CBM is in-between K and Γ points of the Brillouin zone. Therefore, bulk TMDs are semiconductors with momentum-indirect bandgap as presented by the black arrow in the left panel. Note that another energy gap is located at the K point of the Brillouin zone (shown by the red arrow). This gap is momentum-direct but it is not a fundamental one. Importantly, when the thickness of the TMD material is reduced, the energy bands at Γ and between K and Γ points exhibit a considerable shift towards higher energies, while the shift of the gap at K point is much less pronounced. In the monolayer form, the TMD becomes a semiconductor with a momentum-direct gap at K point, as presented by the black arrow in the right panel in Figure 1.4.

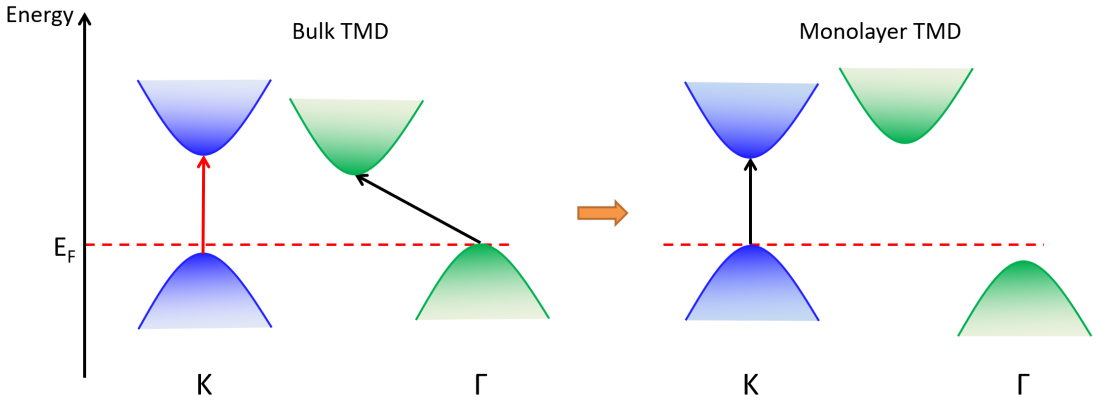

Figure 1.4: Schematic band structure diagram in bulk and monolayer TMDs. The black arrows indicate the fundamental electronic bandgaps. The red arrow represents the direct gap at the K point in bulk TMDs. Fermi level (E_F) is indicated by the red dashed line.

Therefore, when thinned down from bulk to the monolayer form, the TMD undergoes an indirect-to-direct bandgap change. Such variation of the band structure has been attributed to different orbital contributions at different points of the Brillouin zone [50, 66, 75]. In bulk TMDs, the VBM at Γ point is mainly composed of d_{z^2} orbitals of M atoms and p_z orbitals

of X atoms. The CBM in-between K and Γ points consists of $d_{x^2-y^2}$, d_{xy}, d_{z^2} orbitals of M, and p_x, p_y and p_z orbitals of X atoms. The spatial extension of p_z orbitals together with the small separation of X atoms from neighboring layers in the out-of-plane direction enables the mixing of p_z orbitals [75, 76]. This explains the strong dependence of the energy bands on the number of TMD layers. At K point, the VBM is built of $d_{x^2-y^2}$ and d_{xy} orbitals of M, and p_x and p_y orbitals of X atoms, while the CBM is composed of d_{z^2} orbitals of M with a small contribution of p_x and p_y orbitals of X atoms. These orbitals are spatially extended in the plane of a monolayer and their coupling with orbitals from other layers is small. As a result, the energy of the electronic bands at the K point depends weakly on the TMD thickness. This distinct thickness dependence of the energy bands at Γ, in-between K and Γ points, and at the K point of the Brillouin zone, enables the indirect-to-direct bandgap transformation in monolayer TMDs.

In monolayer TMDs, the VBM is composed of d orbitals of M with the magnetic quantum number $m_l = \pm 2$, and p_x and p_y orbitals of X with $m_l = \pm 1$ [70, 75–77]. Due to the large m_l of d orbitals, strong spin-orbit coupling (SOC), i.e. the coupling between the electron spin and its orbital momentum, is induced in these materials. The SOC together with breaking of the inversion symmetry, removes the spin degeneracy at K points of the Brillouin zone. In the VB, the SOC-induced band splitting is on the order of hundreds meV [66, 70, 78, 79]. On the other hand, the CB in monolayer TMDs consists mainly of d_{z^2} orbitals of M with $m_l = 0$ and a small contribution of p_x and p_y orbitals of X with $m_l = \pm 1$. The resulting spin-splitting in the CB in monolayer TMDs is an order of magnitude smaller than in the VB [66, 75, 77, 78]. The calculated spin-splitting in the VB and CB in monolayer TMDs is shown in Table 1.1:

Spin splitting in valence and conduction bands in monolayer TMDs (meV)

TMD	MoS_2	WS_2	$MoSe_2$	WSe_2
Δ_{soc}^{vb}	146 [80]	430 [81]	186 [78]	463 [78]
Δ_{soc}^{cb}	3 [80]	30 [81]	-21 [78]	38 [78]

Table 1.1: The DFT-calculated values of SOC-induced band splitting in the VB (Δ_{soc}^{vb}) and CB (Δ_{soc}^{cb}) in monolayer TMDs.

Kośmider et al. [78] have estimated the atomic contributions into SOC, using the basis of the localized functions similar to the atomic orbitals. The density functional theory (DFT) calculations have shown that the SOC in the CB is composed of two contributions with opposite signs - negative for X and positive for M atoms. Considering that the atomic SOC component is also dependent on the mass of the contributing atom (larger contribution for heavier atoms), the final sign of the spin-splitting in the CB can be either positive or negative,

depending on the combination of M and X atoms in monolayer TMD (e.g. in WS_2 and $MoSe_2$ in Table 1.1).

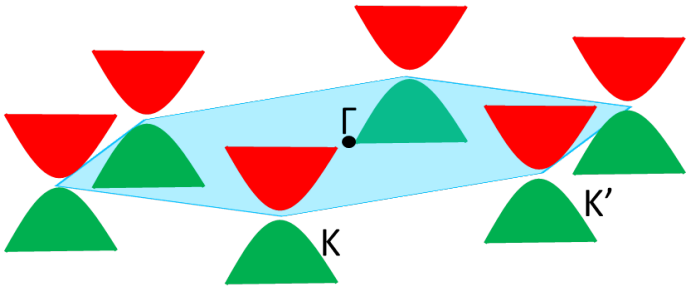

Figure 1.5: Schematic diagram of the VB (green) and CB (red) near the band edges in the Brillouin zone (blue hexagon) in monolayer TMDs. The spin-splitting is omitted.

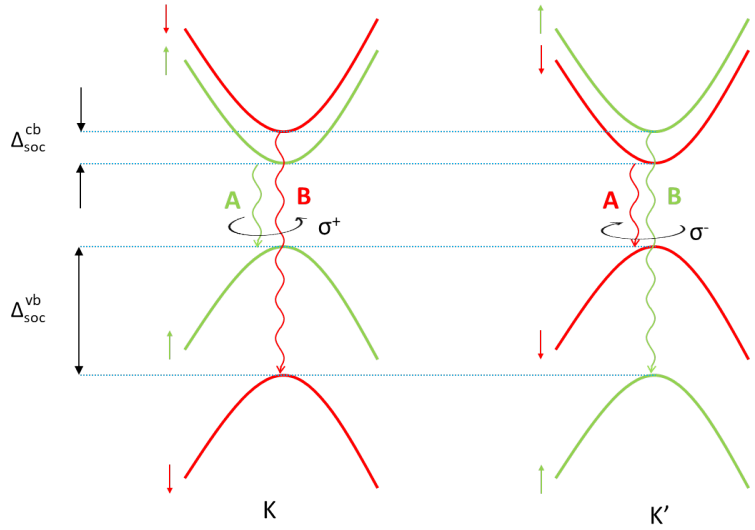

Figure 1.6: Valley and spin optical selection rules at K and K' points in monolayer $MoSe_2$. The Δ_{soc}^{vb} (Δ_{soc}^{cb}) is the SOC-induced spin-splitting in the VB (CB). The σ^+ and σ^- denote the emission of photons with right- and left-handed circular polarization, respectively. The green and red wavy arrows indicate the excitonic transitions in K and K' valleys.

In monolayer TMDs, there are six K points (called valleys) that are located at the corners of the hexagonal Brillouin zone, as shown in Figure 1.5 [64, 66, 79]. The time-reversal symmetry ensures that the SOC-induced spin-splitting at the neighboring energy-degenerate valleys is opposite [64, 66, 79]. Therefore, the neighboring valleys become inequivalent and are usually denoted as K and K' or K^+ and K^- [79]. At each valley two optical transitions are distinguished - exciton A and B (with exciton A having lower energy), as shown in Figure 1.6. In monolayer WS_2, WSe_2 and MoS_2, the SOC-induced spin-splitting in the CB is positive and the carriers at the VBM and CBM have opposite spins. Therefore, the lowest excitonic transitions in these materials are spin-forbidden. Conversely, in monolayer $MoSe_2$ with the negative spin-splitting in the CB, the lowest optical transition is spin-allowed [82].

In monolayer TMDs, both the orbital magnetic moment and spin at the band edges have opposite values at K and K' valleys [79, 83, 84]. Both are experimentally accessible physical quantities, so the carriers with specific spin and valley indices can be addressed and manipulated by external fields [85–87]. The coupling of spin to the specific valley introduces the valley-dependent optical selection rules, presented schematically in Figure 1.6 [84, 88]. The selection rules dictate that the carriers at the K and K' valleys are selectively excited by photons with opposite circular polarization. The large separation of the neighboring valleys in the momentum space and large spin-splitting in the VB effectively suppress the intervalley carrier scattering [89, 90]. This results in valley polarization that can be estimated from the degree of circular polarization of the emitted light, defined as $DCP = \frac{I_{\sigma+} - I_{\sigma-}}{I_{\sigma+} + I_{\sigma-}}$, where $I_{\sigma+}$ ($I_{\sigma-}$) is the right- (left-) handed circularly polarized emission intensity. Monolayer TMDs exhibit large DCP [84, 88, 91] which can be preserved even up to room temperature [92–94]. Recently, Morozov et al. [95] have reported that in monolayer WSe_2 with large electron doping levels the DCP at room temperature is ~ 61 %.

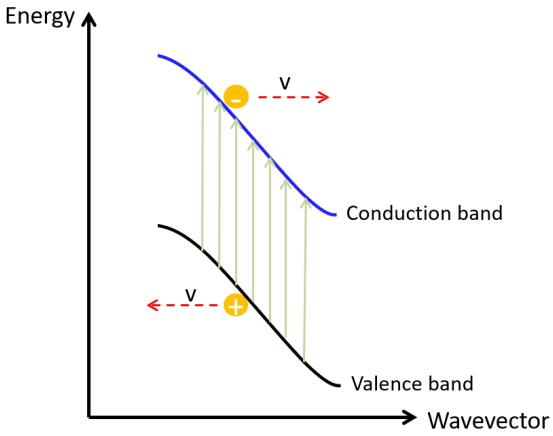

Figure 1.7: Schematic diagram of the band nesting region. The black and blue curves represent the VB and CB, respectively. The orange dots with the + (−) sign represent a hole (an electron). The green arrows indicate the electronic transitions with negligible momentum change. The v denotes the carrier velocity with the directions of movement indicated by the red dashed arrows.

Let me now briefly discuss another interesting region in the Brillouin zone in monolayer TMDs. Namely, there is a region called band nesting region that is schematically presented in Figure 1.7 [96–100]. The bands are considered nested when the gradient of energy difference $E_c - E_v$ (where E_c and E_v is the energy of the lowest unoccupied state in the CB and highest occupied state in the VB, respectively) is negligible, i.e. when the VB (black curve in Figure 1.7) and CB (blue curve) are almost parallel in the Brillouin zone [96]. In the optical transitions at the band nesting region, the hole and electron momentum difference is approximately 0, implying that the carriers move with the same velocities but in opposite

directions. The footprint of band nesting in monolayer TMDs can be experimentally observed as a strong absorption band in the UV spectral region (referred to as exciton C) and large optical conductivity [97, 99]. Kozawa et al. [97] have shown that at room temperature the monolayer MoS_2 can absorb at exciton C as much as ~ 20 % of the incoming light.

1.2.4 Optical properties

1.2.4.1 Dielectric screening

In Section 1.1, I have shown that in an ideal 2D semiconductor, the exciton binding energy is 4 times larger than in bulk. However, the real world is 3D and to accurately describe the optical properties of 2D materials, the impact of the surrounding environment also has to be considered. Here, I will discuss one of the most important effects that contribute to the discrepancy of the exciton binding energies in TMDs from the hydrogen model, namely the dielectric screening effect [101, 102].

In monolayer TMDs, the dielectric screening together with quantum confinement results in exceptionally large exciton binding energies that are on the order of hundreds of meV. This is an order of magnitude larger than in typical quantum well structures, such as III-V GaAs/AlAs or II-VI ZnCdSe/ZnSe [103, 104]. In Table 1.2, I present the experimentally obtained exciton binding energies in monolayer TMDs placed on SiO_2/Si substrate.

Exciton binding energies in monolayer TMDs (meV)

MoS_2	WS_2	$MoSe_2$	WSe_2
440* [105]	320 [44]	420 [106]	370 [107]

*on fused silica

Table 1.2: The exciton binding energies in monolayer TMDs on Si substrate covered by SiO_2 film.

The origin of this important enhancement of binding energies of excitons in monolayer TMD materials is qualitatively explained in a schematic diagram in Figure 1.8. In 3D material with dielectric constant ϵ_{3D}, the Coulomb interaction of electron and hole forming an exciton is screened by the electric field generated by neighboring carriers and atoms (i.e. dielectric screening). This is presented in the left panel in Figure 1.8, where the electric field lines that connect electrons and holes (shown as red-blue curves) are fully submerged in the material. The uniform dielectric screening in 3D materials results in large exciton Bohr radii and low exciton binding energies. In atomically thin monolayer TMDs, the excitons are confined to the TMD layer with dielectric constant ϵ_{2D}. When the monolayer is surrounded by materials with lower dielectric constants (ϵ_1 and ϵ_2 in Figure 1.8), the dielectric screening of the Coulomb interaction in the out-of-plane direction is much weaker than the screening in the in-plane

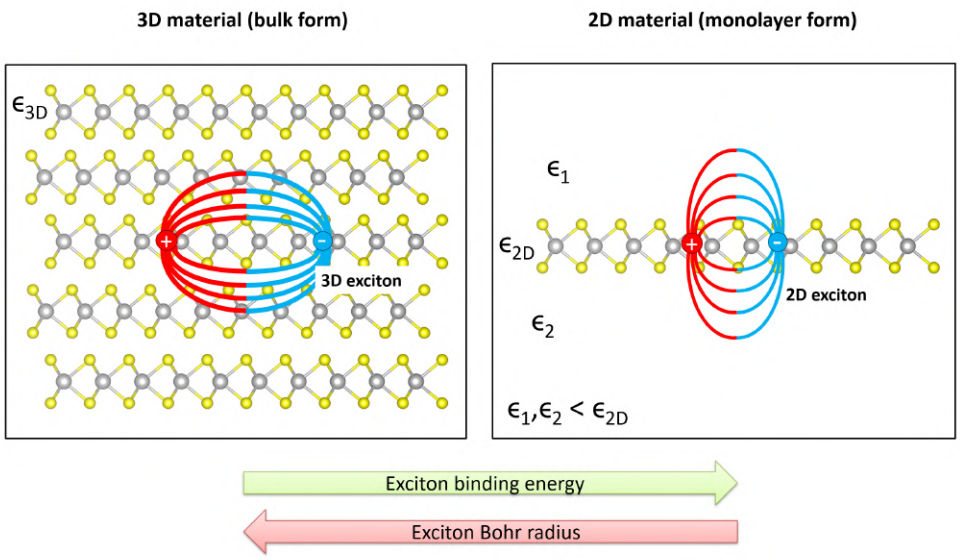

Figure 1.8: Schematic diagram showing the excitons in bulk (left panel) and monolayer (right panel) TMDs with dielectric constants ϵ_{3D} and ϵ_{2D}, respectively. Red-blue lines represent the electric field lines connecting electrons (with sign $-$) and holes (sign $+$). The ϵ_1 (ϵ_2) is a dielectric constant of material in contact with the top (bottom) surface of monolayer TMD.

(monolayer) direction. The weakened out-of-plane screening is the reason why in monolayer TMDs the electron-hole interaction is increased which results in an increase of exciton binding energies and reduced exciton Bohr radii compared to 3D material [108].

Assuming that the electrons and holes are point-like charges localized in the monolayer, the electron-hole interaction in monolayer TMD (the right panel in Figure 1.8) can be described by the potential developed by Keldysh and Rytova [101, 109–112]:

$$V(\mathbf{r_{2D}}) = \frac{-e^2}{8\epsilon_0 r_0}\left[H_0\left(\frac{\kappa \mathbf{r_{2D}}}{r_0}\right) - Y_0\left(\frac{\kappa \mathbf{r_{2D}}}{r_0}\right)\right], \tag{1.14}$$

where H_0 and Y_0 are the Struve and Bessel functions, respectively, $\kappa = (\epsilon_1 + \epsilon_2)/2$, and r_0 is the screening length defined as:

$$r_0 = 2\pi\chi_{2D}, \tag{1.15}$$

where χ_{2D} is the monolayer polarizability.

Importantly, the dielectric screening in monolayer TMDs described by Eq. 1.14 strongly depends on the electron-hole separation - it is larger when the distance between the carriers is smaller. The screening length is a parameter that indicates the inter-carrier distance limit below which the 2D hydrogen model cannot be applied to describe excitons. At the electron-hole separations larger than r_0, the electric field lines connecting electrons and holes mostly penetrate the material surrounding the monolayer. Consequently, the dielectric screening is reduced and the inter-carrier interaction is described by Coulomb potential

$\sim -1/\kappa r_{2D}$. For smaller inter-carrier separation, the electric field lines are mostly submerged in the monolayer with a large dielectric constant and only weakly permeate the environment. As a result, the dielectric screening is increased and the interaction potential scales as $\log(r_{2D}/r_0)$ [44, 112, 113]. Therefore, the discrepancy between the 2D hydrogen model and the model employing the Keldysh-Rytova potential will depend also on the exciton state number n. For instance, Chernikv et al. [44] have shown that in monolayer WS_2 deposited on the SiO_2/Si substrate the hydrogen model describes well the electron-hole interaction only for the states higher than $n = 2$.

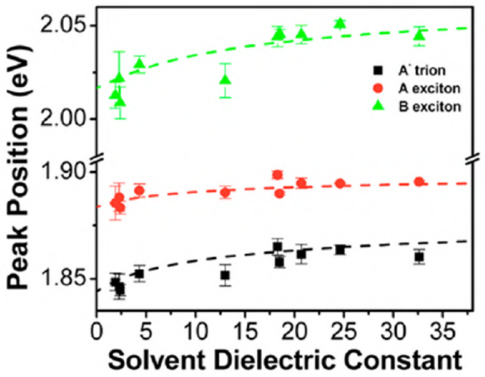

Figure 1.9: The dependence of the exciton A (red dots), exciton B (green triangles) and charged exciton (black squares) emission energy in monolayer MoS_2 on the dielectric constant of the environment. The monolayer was placed on the SiO_2/Si substrate and immersed in organic solvents with different dielectric constants. Adapted with permission from Ref. [114]. Copyright 2014 American Chemical Society.

It follows from the Eq. 1.14 that the dielectric constant of the environment has an important impact on the energy of excitonic peaks in monolayer TMDs [44, 108, 115]. Lin and collaborators [114] investigated the emission energies of the charged exciton (black squares in Figure 1.9), exciton A (red dots) and exciton B (green triangles) peaks in monolayer MoS_2 deposited on the SiO_2/Si substrate and immersed in an organic solvent with dielectric constant ranging from 1.89 to 32.6. It is clear that all the excitonic peaks in monolayer MoS_2 exhibit blueshift when the dielectric constant of the solvent increases. The energy shift can be as large as $\sim$ 40 meV.

1.2.4.2 Photoluminescence

Due to the quantum confinement and reduced dielectric screening discussed above, the optical response in monolayer TMDs is dominated by excitonic transitions.

In doped materials, the excess carriers interact with neutral excitons forming so-called charged excitons. Due to the presence of point defects with low formation energies

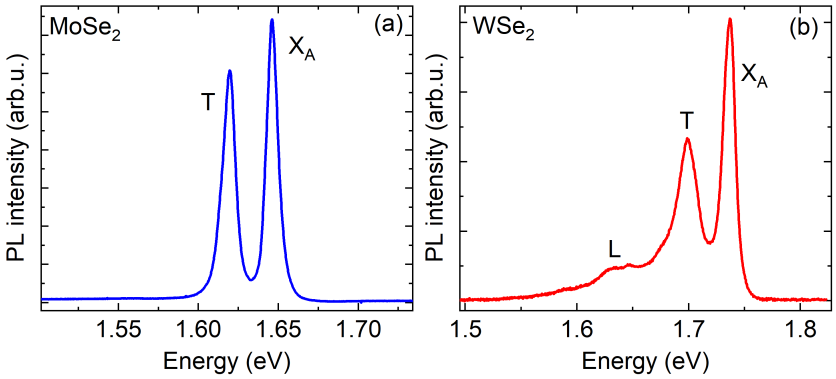

Figure 1.10: (a) - The PL spectrum in monolayer $MoSe_2$ at 5 K. (b) - The PL spectrum in monolayer WSe_2 at 5 K. The X_A (T) is the neutral (charged) exciton, and the L denotes the defect-bound exciton.

(such as chalcogen vacancies) that act as electron donors, monolayer TMDs tend to be naturally n-doped (with the exception of intrinsically p-doped monolayer WSe_2) [51, 116–119]. Therefore, in the PL spectrum of the monolayer TMDs, peaks related to the neutral excitons are accompanied by peaks of the charged excitons. The charged exciton emission is observed below the neutral exciton peak and the energy difference between the neutral and charged exciton peaks (i.e. the charged exciton dissociation energy, E_D) depends on the free carrier concentration in a material (i.e. the Fermi level energy, E_F) according to the formula [120]: $E_D = E_{X_A} - E_T = E_b + E_F$, where E_{X_A} (E_T) is the energy of neutral (charged) exciton PL peak and E_b is the binding energy of charged exciton defined as the dissociation energy in the limit of zero carrier concentration (i.e. where E_F is zero). In monolayer TMDs, the E_D is $\sim$ 30 meV which is an order of magnitude larger than in typical quantum well systems, such as GaAs [118, 121–123]. From the presented above formula it is clear that the larger the carrier density, the larger is the separation of neutral and charged exciton peaks [120, 123]. In monolayer TMDs, the E_D can be influenced by electrostatic gate doping or by the variation of the excitation power that enables the ionization of dopants on which the carriers get trapped at low temperatures [120, 123]. An example of the PL spectrum collected from monolayer $MoSe_2$ is shown in Figure 1.10 (a), where the neutral (X_A) and charged (T) exciton peaks with E_D of around 30 meV can be observed.

In monolayer TMDs, the structural defects - such as atomic vacancies, grain boundaries or wrinkles formed during the monolayer transfer process, introduce electronic states inside the bandgap [116, 117, 119]. The excitons can be trapped by these states and the emission energies of such bound excitons are observed below the neutral and charged excitonic transitions [82, 124, 125]. As the non-intentional defect states are usually distributed randomly in a material, the optical response of monolayer TMDs may be also highly

non-uniform [126, 127]. Importantly, the localized exciton peaks are usually observed in the emission spectra in monolayer TMDs with dark ground exciton state (MoS_2, WS_2 and WSe_2), where the carrier lifetime is long enough to enable the exciton localization on the states within the bandgap. This explains, why the PL spectra in MoS_2, WS_2 and WSe_2 are usually richer than in $MoSe_2$. For instance, in the PL spectrum in monolayer WSe_2 shown in Figure 1.10 (b), the peaks of neutral (X_A), charged (T) and bound (L) exciton peaks can be observed.

1.3 2D perovskites

1.3.1 Introduction

Perovskites, named after Russian mineralogist Lev Perovski, belong to a large family of materials with a general formula ABX_3 (where A denotes a large organic or inorganic cation, B is a small metal cation, and X - an anion). The cubic perovskite unit cell is presented in Figure 1.11 [128]. The A cations sit in the corners of a unit cell, while B cations are in the body-centered, and X anions - are in the face-centered positions. Therefore, the B and X ions form corner-sharing BX_6^{4-} octahedra with A cations filling the spaces between them.

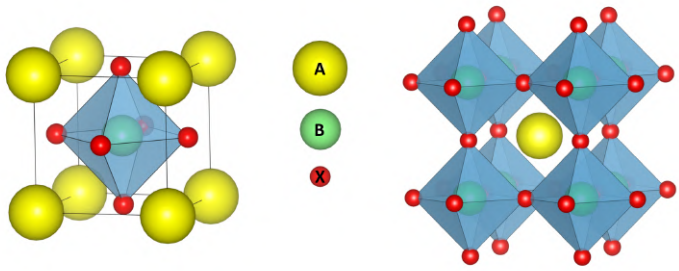

Figure 1.11: Perovskite crystal structure - cubic unit cell (left panel) and octahedra arrangement (right panel). The A represents organic or inorganic cation, B - metal cation, and X - oxide or halide anion. Generated from data from Ref. [128].

The first studied material with a perovskite structure was a mineral oxide $CaTiO_3$ [129]. Since its discovery in 1957, the research focused mostly on the full-inorganic perovskites exhibiting piezoelectric and ferroelectric properties, such as $LiNbO_3$, $PbTiO_3$ or $PbTiO_3$ [130–132]. In 1978, Weber [133] conducted the first crystallographic studies on hybrid organic-inorganic halide perovskites $CH_3NH_3PbX_3$, where an inorganic A cation was replaced by an organic methylammonium cation ($CH_3NH_3^+$ - MA), and X was halide anion Cl^-, Br^- or I^-. Three decades later, Kojima et al. [134] have fabricated the first perovskite-based

($CH_3NH_3PbI_3$ - MAPI) solar cell device with a power conversion efficiency (PCE) of 3.8 %. Since then, the potential of applying perovskites in optoelectronic devices has rekindled the interest in perovskite materials. In only 10 years, the PCE of the organic-inorganic halide perovskite-based solar cells was increased to over 25 % [135, 136]. Various interesting properties of perovskites and the availability of a variety of compounds that can be used in their synthesis, have given promises for applications not only in solar cells but also in lasers [137], photodetectors [138] or optical modulators [139], to name a few.

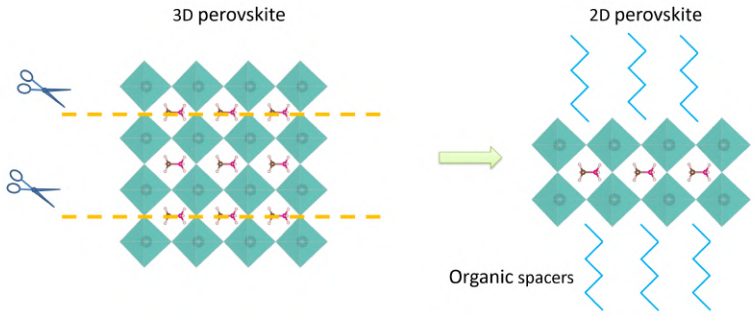

Figure 1.12: The schematic representation of the 2D perovskite crystal structure (right panel) obtained by cutting the octahedra layers from 3D perovskite (left panel). Generated based on data from Ref. [140].

Among a large class of perovskite materials, there is one particular group, namely, the 2D perovskites. They can be regarded as slabs cut out of 3D perovskites and linked in the out-of-plane direction by large organic spacer molecules, as presented in Figure 1.12. The 2D perovskites have a general formula $(RNH_3)_2A_{n-1}B_nX_{3n+1}$, where RNH_3^+ is an organic spacer monovalent cation with either aliphatic or aromatic alkyl group R (e.g. butyl, phenylethyl), A is a monovalent organic or inorganic cation (e.g. methylammonium, formamidinium, Cs^+), B is a divalent metal cation (such as Pb^{2+} or Sn^{2+}), X is a halide anion (Cl^-, I^-, Br^-), and $n = 1, 2...$ denotes a number of inorganic octahedra slabs between two subsequent organic spacer layers. The first 2D perovskites - $(C_9H_{19}NH_3)_2PbI_4$ and $(C_{10}H_{21}NH_3)_2CdCl_4$, were synthesized by Dolzhenko and collaborators in 1986 [141, 142]. What makes the family of 2D perovskites especially attractive is, among other things, a much lower degradation rate in the environmental conditions in comparison to their 3D counterparts. Therefore, the 2D perovskites could be used in solar cells as protective layers for the sensitive to temperature and moisture 3D perovskite absorber films [143, 144]. Other possible applications of 2D perovskite materials include: light-emitting devices [145], energy conversion and storage devices [146], lasers [147] and photodetectors [148].

1.3.2 Crystal structure

The thermodynamically stable perovskite structure has to fulfill several criteria. First, the charge of the constituent ions has to be balanced so that the net charge of the whole structure equals 0. If X is a halide ion, then A should be monovalent and B - a divalent cation. Alternatively, instead of two divalent B ions, a mixture of cations that overall give the same net charge can be used, e.g. one monovalent B' and one trivalent B" cation. Another important criterion applies to the size of A cation which has to be small enough to fit in the space between neighboring octahedra. Additionally, B cations must have a suitable size to enable their octahedral coordination by X anions [149].

The mentioned guidelines regarding the choice of constituent compounds apply to both 3D and 2D hybrid organic-inorganic perovskites. However, the 2D perovskite family offers a much broader selection of materials that can be used as organic spacers, since there is no restriction regarding the spacer length. The important limitation is for the spacer width to be within a specific range imposed by the B-X bonding length. If the size of the spacer ion is too large, there will be not enough space for it to fit between octahedra. In such a case, the structure will accept a lesser amount of spacer cations than is dictated by stoichiometry resulting in numerous structural defects. Conversely, if the spacers are too small, higher concentrations of spacer cations can be incorporated into the structure [150]. In a stable 2D perovskite material, an organic spacer also has to contain a terminal functional group that would enable directional non-covalent interactions with octahedra slabs. These groups

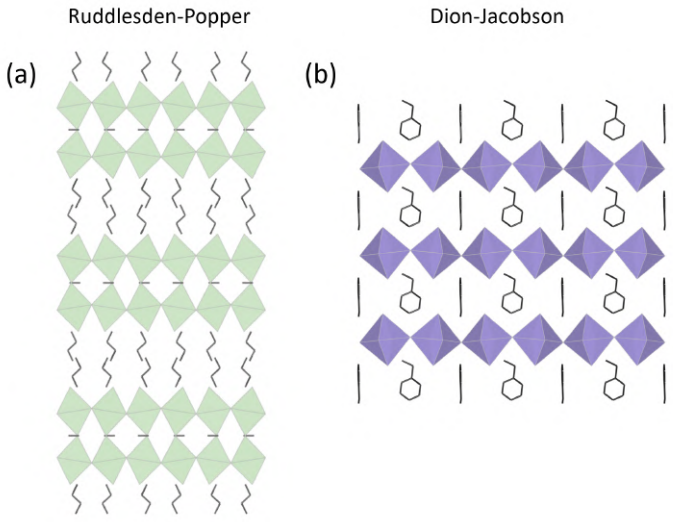

Figure 1.13: Crystal structure of (a) - Ruddlesden-Popper and (b) - Dion-Jacobson 2D perovskites. The green and violet colors indicate the inorganic octahedra. (a) - Based on data from Ref. [140]. (b) - Based on data from Ref. [151].

are usually RNH_3^+, where R denotes an aliphatic chain or aromatic ring. The ammonium groups form strong hydrogen bondings with halide anions and stabilize the connection of organic spacers with the octahedral framework. Therefore, the rigidity of the perovskite structure can be easily manipulated by choosing an organic spacer with a different number of ammonium groups [152].

Two main crystal structures of 2D perovskites - Ruddlesden-Popper and Dion-Jacobson are schematically presented in Figure 1.13. In Ruddlesden-Popper perovskites, each octahedra slab is connected with one organic spacer layer from the top and one layer from the bottom side along the stacking axis. In this arrangement, the spacer cations from the adjacent layers are linked with each other via van der Waals interactions which enables their easy exfoliation. In Dion-Jacobson perovskites, the subsequent octahedra slabs are connected with each other by a single layer of organic spacer cations. To enable simultaneous interactions with two inorganic slabs, the spacer compound has to terminate with two functional groups, one on each spacer end [153].

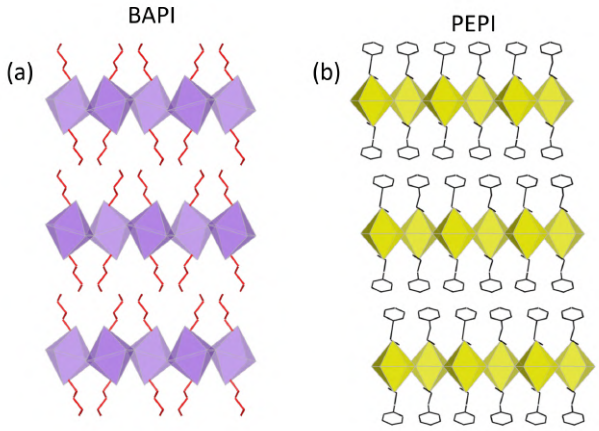

Figure 1.14: (a) - The crystal structure of low-temperature phase of BAPI perovskite along the stacking axis. The violet color indicates the PbI_6^{4-} octahedra and the BA^+ spacers are shown in red color. Based on data from Ref. [154]. (b) - The crystal structure of PEPI perovskite. The PEA^+ spacers and PbI_6^{4-} octahedra are shown in black and yellow colors, respectively. Based on data from Ref. [155].

Two of the most studied 2D perovskites are BA_2PbI_4 (BAPI) and PEA_2PbI_4 (PEPI), where BA stands for butylammonium and PEA for phenylethylammonium cations. Both PEPI and BAPI are the constituents of the van der Waals stacks that will be studied in this thesis. In Figure 1.14, I present the crystal structure of (a) - the low-temperature phase of BAPI perovskite and (b) - of PEPI perovskite. Both materials exhibit the Ruddlesden-Popper structure.

1.3.3 Band structure

In 2D perovskites, the inorganic octahedra slabs with narrow bandgap are sandwiched between two organic spacer layers with wide bandgap. This arrangement forms a multiple potential well structure, shown schematically in Figure 1.15 [156]. The 2D perovskites are sometimes referred to as "ideal" 2D systems with the large difference of the barrier and well bandgaps and naturally low interlayer roughness [157].

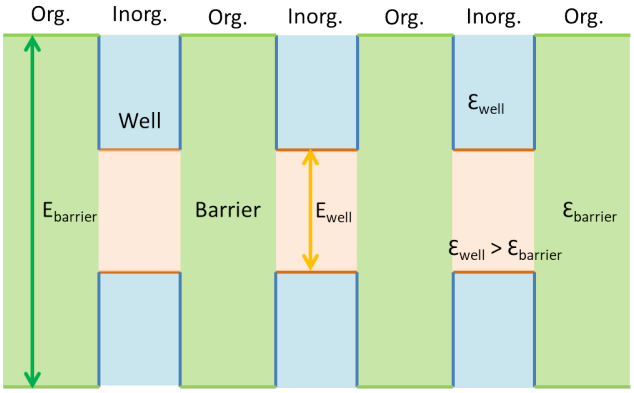

Figure 1.15: Schematic multiple quantum well structure in 2D perovskites. $E_{barrier}$ (E_{well}) denotes the barrier (quantum well) bandgap and $\epsilon_{barrier}$ (ϵ_{well}) is the dielectric constant of the barrier (quantum well).

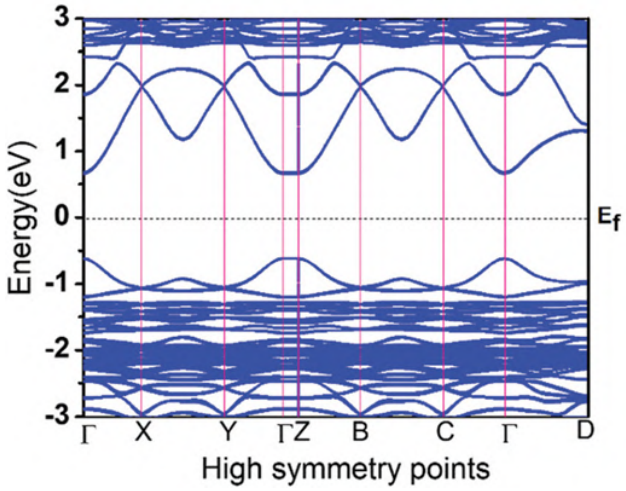

Figure 1.16: The band structure in PEPI perovskite. The E_f indicates the Fermi energy. Adapted from Ref. [158].

Lead-iodide 2D perovskites are momentum-direct bandgap semiconductors with a bandgap located at the Γ point of the Brillouin zone, as presented in the DFT-calculated band structure of PEPI in Figure 1.16 [158]. The VBM is composed of 5p orbitals of iodine with a small contribution of 6s orbitals of lead ions, and the CBM is built of 6p orbitals of lead cations [140, 159–162]. The bands with a large contribution of organic spacer orbitals appear

almost flat in the band structure (e.g. along Γ-Z direction in Figure 1.16) which indicates that the organic spacer orbitals overlap weakly with the octahedra slabs. Therefore, the carrier effective masses (given by the band curvatures) are large along the stacking direction which implies the good carrier confinement to the plane of inorganic octahedra slabs [140, 163].

In lead-iodide 2D perovskites, 6p orbitals of heavy Pb^{2+} cations induce strong SOC in the CB resulting in the lowering of the CBM by ~ 0.7 eV [159, 160, 164, 165]. In the VB, the energy bands are mainly built of 5p orbitals of much lighter I^- anions and the SOC is several times smaller than in the CB [165]. Overall, in 2D perovskites, the SOC effect reduces the perovskite bandgap by around 1 eV [164, 165].

1.3.4 Optical properties

As was discussed in the previous subsection, the 2D perovskites naturally form the structure of multiple quantum wells. Unlike in the epitaxially grown II-VI or III-V inorganic quantum wells, in 2D perovskites, the quantum confinement is accompanied by reduced dielectric screening dictated by the large difference of dielectric constants of the organic spacer layer and inorganic octahedra slab ($\epsilon_{barrier} < \epsilon_{well}$). Therefore, the carriers that are quantum confined to the inorganic slab are also subjected to the weak dielectric screening of organic spacer layers which results in strong binding of electrons and holes. Importantly, in 2D perovskites, the exciton binding energy can be easily tuned by using compounds with different dielectric constants. For instance, the experimental values of exciton binding

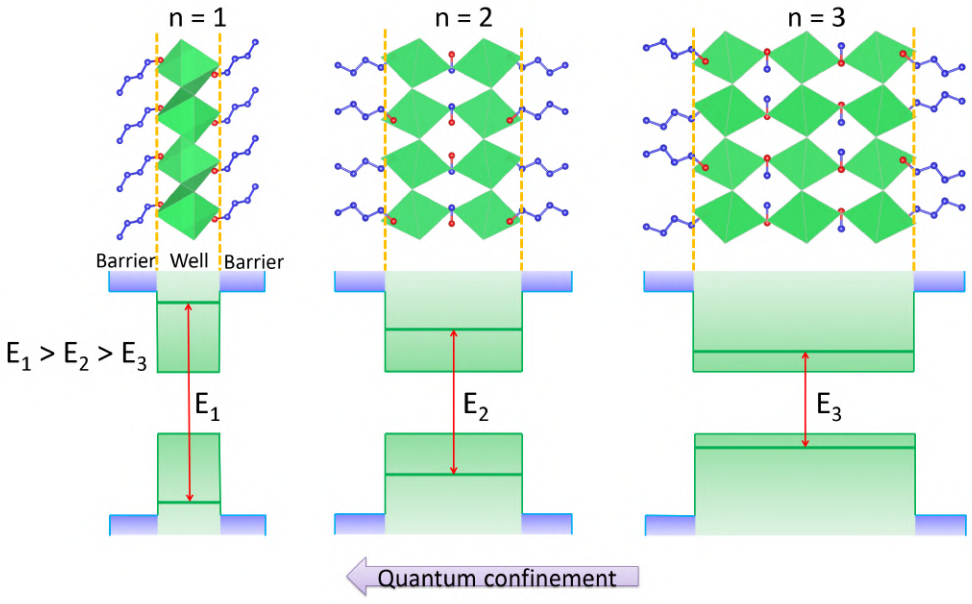

Figure 1.17: Schematic diagram showing the dependence of the bandgap E_n (n = 1, 2, 3) on the thickness of the quantum well in 2D perovskites. Based on data from Ref. [140, 155]

energies in PEPI and BAPI perovskites (that are composed of the same PbI_6^{4-} octahedra but different organic spacer cations - PEA^+ or BA^-) are 260 meV [166–168] and 470 meV [168], respectively. Overall, the exciton binding energy in 2D perovskites is one order of magnitude larger than in typical inorganic quantum well structures. Therefore, the optical transitions in 2D perovskites are dominated by excitons [103, 104], also at room temperature [167, 169].

An important advantage of 2D perovskite materials is that their electronic and optical properties are easily tunable. Like in other quantum well structures, in 2D perovskites, the size of the bandgap depends on the width of a potential well (i.e. the number of octahedra slabs between the subsequent spacer layers, n). This is clearly visible in Figure 1.17, where the larger well thickness (i.e. with larger n) results in a smaller bandgap (indicated by red double arrows). This effect can be also observed in room temperature PL spectra in $BA_2MA_{n-1}Pb_nI_{3n+1}$ (n = 1-5) perovskites shown in Figure 1.18. As the quantum well thickness increases, the perovskite emission energy gradually redshifts.

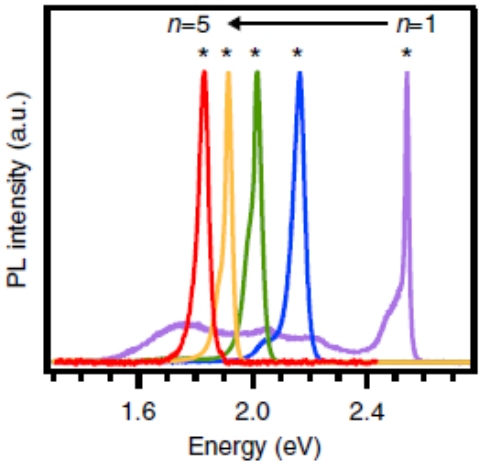

Figure 1.18: Room temperature PL spectra in $BA_2MA_{n-1}Pb_nI_{3n+1}$ (n = 1-5) perovskites. Adapted from Ref. [168]. Copy of the Creative Commons license can be found at: http://creativecommons.org/licenses/by/4.0/

Another way of engineering properties of 2D perovskites involves using different precursors in the synthesis process [170, 171]. As the VBM is mainly composed of halide orbitals from the inorganic octahedra, heavier halide anions would shift the VBM to lower energies. Consequently, the perovskite bandgap would be reduced, e.g. the calculated bandgap in PEA_2PbCl_4 is 3.19 eV, while in PEA_2PbBr_4 the bandgap is 2.76 eV [172]. By analogy, changing the metal cations modulates the energy of the CBM [173]. For instance, the bandgap of PEA_2PbI_4 is larger than that of PEA_2SnI_4 (2.608 eV vs. 2.084 eV) [166].

The organic spacer compound can also modify the bandgap of 2D perovskites by influencing the inorganic octahedra framework [174, 175]. The large impact of the organic spacers on the material properties was observed in two perovskites studied in this thesis.

The PEPI and BAPI perovskites are composed of the same PbI_6^{4-} inorganic octahedra but different organic spacer (PEA^+ in PEPI and BA^+ in BAPI) . The experimentally determined bandgap (at the temperature of $\sim$ 4 K) in PEPI and BAPI perovskite is around 2.61 eV and 3.02 eV, respectively [166, 168]. This large difference of the bandgaps can be explained by the different impact of the organic spacer on the Pb-I-Pb bonding angles and Pb-I bonding lengths via the interactions of -NH_3^+ groups with iodine anions from PbI_6^{4-} octahedra slabs [158, 163, 166, 176, 177]. In BAPI perovskite, the octahedra are tilted with respect to the stacking axis, as was shown in Figure 1.14 (a). The large deviations of the equatorial Pb-I-Pb angle from 180° changes the overlap of the iodine and lead orbitals and increases the perovskite bandgap [175, 176, 178, 179]. The more pronounced octahedral distortion in BAPI than in PEPI results in the smaller bandgap of the latter.

1.4 Excitation transfer in van der Waals stacks

1.4.1 Introduction

Layered van der Waals materials like TMDs or 2D perovskites can be easily stacked and form heterostructures. The electronic coupling between the constituent layers gives rise to physical phenomena that strongly influence the electronic and optical properties of van der Waals stacks. In this Section, I will discuss two processes that enable the excitation transfer between the constituents of heterostructures, namely, the charge and energy transfer.

1.4.2 Charge transfer

The calculated energies of the VB and CB edges with respect to the vacuum level in monolayer TMDs are presented in Figure 1.19 [180–182]. It is clear that the stacks composed of any two monolayer TMDs have a type II band alignment with the VBM and CBM located at K valleys but in different materials [183, 184]. Together with the flat and smooth, atomically thin interfaces, this forms an excellent environment for a fast and efficient charge transfer (CT) to a material with lower energy VBM (transfer of holes) or CBM (transfer of electrons) [5, 8, 9, 185, 186]. In TMD stacks, the CT occurs on $\sim$ 100 fs timescale which is much faster than the lifetime of intralayer excitons in TMDs ($\sim$ 10 ps) [28, 187, 188]. The fast CT in TMD stacks is driven by the large band offsets - e.g. in MoS_2/WSe_2 the VB and CB offset is 1.01 eV and 0.67 eV, respectively [180]. Small interlayer distances (in MoS_2/WSe_2 $\sim$ 6 Å) additionally facilitate the transfer process [183]. The mechanism of CT in the fs regime is not yet fully understood. However, several hypotheses trying to explain the ultrafast nature

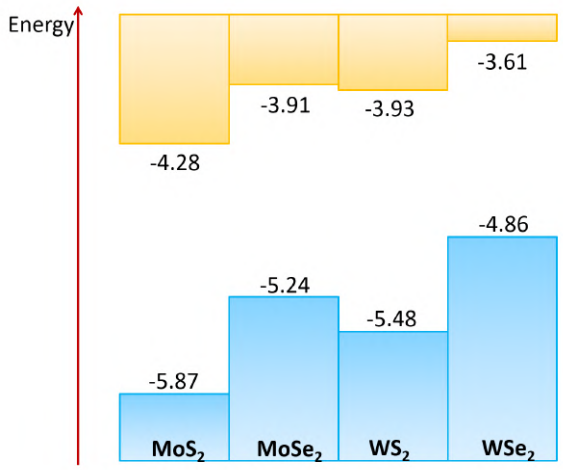

Figure 1.19: The band alignments in monolayer TMDs calculated with respect to the vacuum level. Based on Ref. [180].

of this phenomenon, have so far been made in the literature [189, 190]. For instance, Zhu and collaborators [190] have proposed that the transfer of carriers between K valleys in van der Waals stacks involves the intermediate state located at another wavevector in the Brillouin zone. The CT via this state, common to both constituents, is possible with the assistance of phonons.

The CT in TMD stacks leads to the formation of low-energy interlayer excitons (IXs) in which the electrons and holes localized in different materials are bound across the interface. The binding energy of IXs in TMD stacks is on the order of $\sim$ 100 meV which shows great potential for future optoelectronic devices operating at room temperature [7, 8, 191–194].

For the first time, the IXs were observed by Rivera et al. [8] in $WSe_2/MoSe_2$ stack. The low-temperature PL spectra in $WSe_2/MoSe_2$ stack are shown in Figure 1.20 (a). The IX peak is redshifted with respect to intralayer excitons in the constituent monolayers. This is a result of the relaxation of the carriers to their respective band minima, as presented by curved arrows in Figure 1.20 (b). The large electron-hole distance in IXs reduces the overlap of carrier wavefunctions in comparison to intralayer excitons. The reduced transition dipole moment of IX importantly decreases its oscillator strength which is manifested by long IX lifetimes [195, 196]. The PL decay of IX in $WSe_2/MoSe_2$ stack is shown in Figure 1.20 (c). The fit with the monoexponential function gives the IX PL decay time of 1.8 ns. This is two orders of magnitude larger than the decay times of intralayer excitons in monolayer TMDs [92, 197]. The long PL decay times of IXs could potentially enable the Bose-Einstein condensation of IXs [198, 199].

Due to the suppressed intervalley scattering in monolayer TMDs, in TMD stacks the carriers are transferred to their respective band extrema preserving the valley polarization

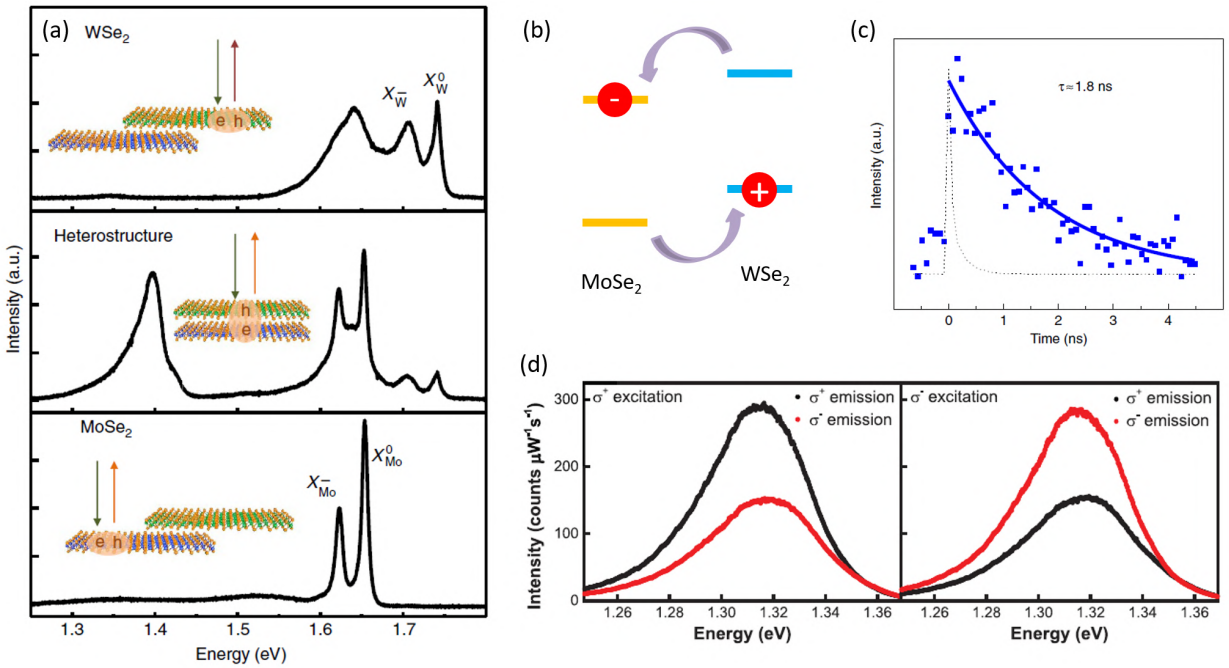

Figure 1.20: (a) - The PL spectra in monolayer TMDs (upper and bottom panels), and in the heterostructure region (middle panel) in $WSe_2/MoSe_2$ stack. The $X^-_{W/Mo}$ and $X^0_{W/Mo}$ denote the charged and neutral excitons, respectively. The subscripts indicate the monolayer: WSe_2 (W subscript) and $MoSe_2$ (Mo subscript). (b) - Schematic band alignment in $WSe_2/MoSe_2$ stack. Violet curved arrows indicate the CT. Red dots with $-$ and $+$ signs represent the electron and hole, respectively. (c) - The PL decay of IX (blue dots) with the monoexponential fit (blue curve). The dashed curve is the instrument response function. (d) - Circularly-polarized PL spectra of IX in $WSe_2/MoSe_2$ stack under σ^+- (left panel) and σ^-- (right panel) circularly polarized excitation. (a), (c) - From Ref. [8]. Reproduced with permission from Springer Nature. (d) - From Ref. [9]. Reprinted with permission from AAAS.

[9]. The carriers bind into IXs and then recombine maintaining the excitation polarization. This is clearly visible in the circular polarization-resolved PL spectra of IX in $WSe_2/MoSe_2$ stack shown in Figure 1.20 (d).

In the IXs the spatially separated carriers form an interfacial dipole moment which enables the modification of the IX properties by external fields [89, 200, 201]. Rivera et al. [9] have shown that the electric field applied across the $WSe_2/MoSe_2$ stack enables the change of the band offsets and leads to either red- or blueshift of the IX energy, depending on the orientation of the IX dipole and applied external bias. For instance, the IX energy shift of ~ 60 meV was observed in $WSe_2/MoSe_2$ stack by applying a bias of 70 V [9]. The external electric field was shown to affect also the PL decay time, polarization and diffusion of IXs showing potential for applications in optical communication and signal-processing devices [9, 202, 203].

1.4.3 Energy transfer

In van der Waals stacks with type II band alignment, the dominating mechanism of excitation transfer between monolayers is via the CT [8, 9, 185]. However, for certain heterostructure configurations, e.g. when monolayers are separated by thin insulating hexagonal boron nitride (hBN) layers, the CT can be suppressed. Another mechanism then starts dominating in the system, namely, the energy transfer (ET) [29, 204, 205].

The ET is a process in which the energy of a donor compound (D) in its excited state is transferred to an acceptor compound (A) which is in the ground state. As a result, D relaxes to the ground state, while A is excited to the higher energy state. The transfer can take place via either a radiative or non-radiative pathway.

The radiative ET is the process in which the photoexcited D relaxes to its ground state by the emission of photons. The photons are absorbed by A, promoting it to the excited state. The radiative ET can be expressed by the following formulae [206]:

$$\begin{aligned} D^* &\rightarrow D + \hbar\omega \\ \hbar\omega + A &\rightarrow A^*, \end{aligned} \tag{1.16}$$

where * indicates the excited state and $\hbar\omega$ denotes the energy of the photon emitted by D and later absorbed by A. The efficiency of the process of radiative ET depends on the D-A spatial separation and the PL quantum yield of D. The process takes place only if the D-A distance is equal to or larger than the wavelength of the photon emitted by D [206].

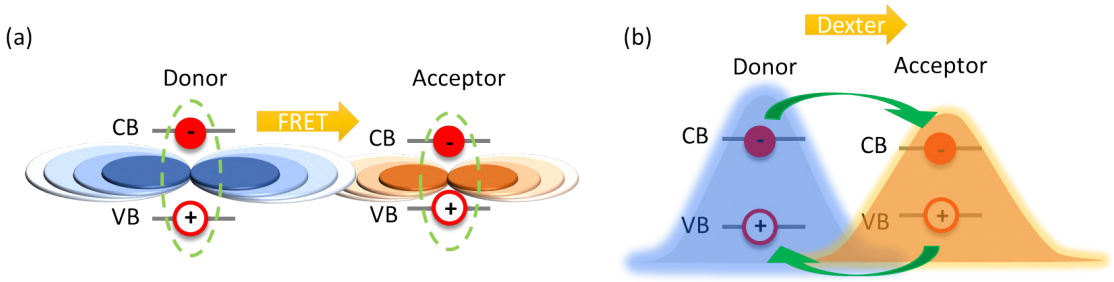

Figure 1.21: (a) - Mechanism of FRET. The electric dipole of D and A is shown in blue and orange color, respectively. (b) - Mechanism of Dexter ET. The carrier wavefunction in D (A) is indicated by blue (orange) color. Red circles (dots) represent holes (electrons). Green curved arrows indicate the carrier transfer between D and A. Orange arrows indicate the transfer via FRET and Dexter ET mechanism.

The non-radiative ET can take place via Förster resonant ET (FRET) or Dexter ET, the mechanisms of which are presented schematically in Figure 1.21 [204, 207–209]. In FRET - (a), the transfer of photoexcited exciton energy from D to A is mediated by dipole-dipole interactions, where the externally induced transition dipole in D oscillates and generates

a dipole in A. Therefore, the process can involve only dipole-allowed transitions in D and A [207, 209, 210]. The rate of FRET, k_{FRET}, is strongly dependent on the D-A distance (r) [206]:

$$k_{FRET} = \frac{1}{\tau_D}\left(\frac{R_0}{r}\right)^{\alpha}, \tag{1.17}$$

where τ_D is the radiative decay time of D (when A is absent) and R_0 denotes the Förster distance (when $r = R_0$, the FRET rate is equal to D decay rate). The α is an exponent dependent on the dimensionality of D and A. In 2D-2D heterostructures, the rate of FRET is proportional to $\sim r^{-4}$ ($\alpha = 4$) [211]. The FRET is usually observed in structures, where the spatial separation between the materials with D and A states is in the range from $\sim$ 1 nm to $\sim$ 10 nm [206, 212].

The efficiency of FRET can be estimated as [32, 206]:

$$\beta_{FRET} = 1 - \frac{I_{DA}}{I_D} = \frac{k_{FRET}}{k_r + k_{nr} + k_{FRET}} = 1 - \frac{\tau_{DA}}{\tau_D}, \tag{1.18}$$

where I_{DA} (I_D) is the emission intensity of D when A is present (emission intensity of D with no A), k_r (k_{nr}) is the rate of radiative (nonradiative) processes in D and τ_{DA} (τ_D) is the radiative decay time of D when A is present (when A is absent). According to this formula, the FRET will be efficient in the structures, where the radiative decay time of D in the presence of A is shorter than the decay time in D without A.

Despite type II band alignment, in TMD/TMD stacks the fast and efficient ET via FRET can take place next to the CT [204, 210]. The signatures of FRET were observed by Kozawa et al. [204] in $MoSe_2/WS_2$ stacks. The estimated rate of FRET was around three orders of magnitude faster than in, e.g. wide barrier-separated GaAs quantum wells [204, 213]. Xu and collaborators [210] have shown that FRET can also emerge by inserting the insulating hBN between the TMD monolayers. In WS_2/a-hBN/MoS_2 stacks (where a denotes the number of hBN layers), the FRET was observed in stacks with 2-5 layers of hBN. For 0 and 1 hBN layers, the CT was the main mechanism of excitation transfer. Above 5 hBN layers, the interlayer coupling was negligible and stacks behaved as two separate TMD monolayers.

Another mechanism of non-radiative ET is Dexter ET, in which the electrons and holes are simultaneously exchanged between D and A states, as shown in the right panel in Figure 1.21 (b) [214]. This process is mediated by carrier exchange interactions and strongly depends on the overlap of D and A carrier wavefunctions. The limiting D-A distance in Dexter ET is $\sim$ 1 nm [214]. As opposed to FRET, Dexter ET does not depend on the transition oscillator strength in D and A. Therefore, the process can involve dark exciton states which may be used for brightening of dark excitons in van der Waals stacks [29, 211].

The rate of Dexter ET for molecular D and A is described by a formula [211]:

$$k_{DET} = KJ \exp \frac{-2r}{L}, \tag{1.19}$$

where K denotes the experimental constant dependent on D and A orbital interactions, J is the normalized spectral overlap integral, r is the D-A distance and L represents the sum of D and A van der Waals radii (which indicates the minimum distance between D and A molecules).

Dexter ET was observed by Wu et al. [29] in stacks composed of monolayer $MoTe_2$ with either mono- or bilayer WSe_2. The estimated efficiency of Dexter ET was $\sim$ 97 %. Such ultrafast ET rate (on the order of 200 fs) was ascribed to the fast CT which is typical to the TMD/TMD stacks [28, 29].

Synthesis and sample preparation

In this Chapter, I will describe the samples studied in this thesis. I will shortly discuss the synthesis methods used to obtain the constituent materials of the stacks. I will also present the steps of the fabrication process of the investigated heterostructures.

2.1 Introduction

In this thesis, I study three heterostructures - PEPI/WS_2, PEPI/$MoSe_2$ and BAPI/$MoSe_2$. The PEPI/WS_2 stack was fabricated by Michteld Kamminga from the group of Graeme Blake and Minpeng Liang from the group of Jianting Ye at the University of Groningen. The PEPI/$MoSe_2$ stack was prepared by Matan Menahem from the group of Omer Yaffe at the Weizmann Institute of Science and by Jonas Ziegler from the group of Alexey Chernikov at the University of Regensburg. The BAPI/$MoSe_2$ stack was fabricated by Pabitra Nayak from the group of Henry Snaith at the University of Oxford and by Jonas Ziegler from the group of Alexey Chernikov at the University of Regensburg.

Each heterostructure was composed of (1) a monolayer TMD flake and (2) a multilayer 2D perovskite flake. The whole stack was encapsulated by multilayer hexagonal boron nitride (hBN) obtained by: (i) exfoliation from bulk crystal purchased from HQ graphene (in case of PEPI/WS_2 sample) or (ii) provided by Takashi Taniguchi and Kenji Watanabe from National Institute for Materials Science in Japan (PEPI/$MoSe_2$ and BAPI/$MoSe_2$ samples). Each stack was placed on a silicon substrate with SiO_2 top layer.

2.2 PEPI/WS_2

The schematic structure of PEPI/WS_2 stack is shown in Figure 2.1. The monolayer WS_2 flake (blue color) partly covered the multilayer 2D PEPI perovskite flake (yellow). This structure was placed on the bottom hBN flake (brown), covered by the top hBN flake (red), and placed on SiO_2/Si substrate (green). Such arrangement of materials allowed optical

access to three characteristic regions: perovskite and TMD (from now on I will refer to these parts of flakes as bare), and the heterostructure (HS) region (white dashed oval in Figure 2.1).

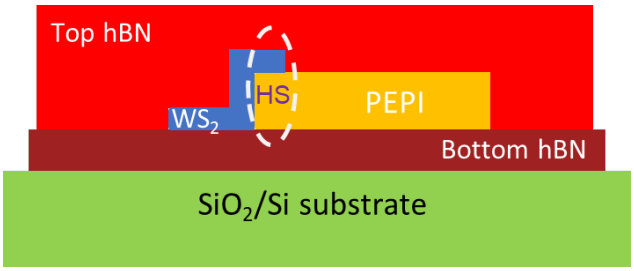

Figure 2.1: The schematic structure of PEPI/WS_2 stack. The HS region is indicated by a white dashed oval.

Encapsulation in hBN is one of the methods used to improve the optical quality of the TMD flakes [215]. Cadiz and co-workers [216] have shown that upon encapsulation in hBN, monolayer TMDs exhibit a significant enhancement of the emission intensity and reduction of the photoluminescence (PL) and reflectance (RL) linewidths. These effects have been ascribed to the unique roles that the insulating hBN can play when encapsulating TMD. First, the hBN layer acts as a spacer between the rough surface of the substrate (e.g. SiO_2 film) and the TMD, leading to a reduction of defect density in the latter [217]. Apart from protecting TMD from the surface imperfections of the substrate, the hBN layer can also suppress the undesired charge transfer from the substrate to TMD [218]. Additionally, the capping layer of hBN has been shown to protect the flakes from environmental contamination by oxygen and water molecules [219]. The remarkable effect that the encapsulation has on the optoelectronic properties of TMDs (such as decrease of the peak linewidths) enables a distinction of many excitonic transitions and is indispensable in the studies of subtle physical effects such as exciton fine structure [220–222]. The encapsulation in hBN is now widely used to improve the quality of various van der Waals materials and their stacks [223, 224]. In 2D perovskites, encapsulation in hBN has been shown to significantly reduce the process of material degradation [225, 226].

The synthesis of PEPI single crystals for PEPI/WS_2 sample was conducted by Machteld Kamminga at the University of Groningen. The employed growth technique exploited the difference in solution densities as described in detail in Ref. [227] and is based on the method developed by Mitzi et al. [228]. In the synthesis of PEPI, a high-density PbI_2/HI solution was injected into the bottom of a long glass tube. The less-dense absolute methanol was added on top of PbI_2/HI. Due to a significant difference in densities, a distinct interface was formed between the solutions. The phenylethylamine was then added dropwise to the mixture. Precursors slowly diffused at the interface, initiating the process of perovskite

growth. Single crystals of PEPI were collected after 5 days. Each step of the synthesis was conducted at room temperature.

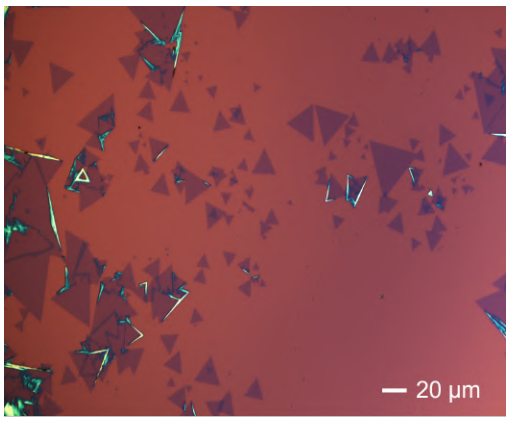

Figure 2.2: Triangular monolayer WS_2 flakes after the CVD synthesis on the SiO_2/Si substrate. The white horizontal bar indicates the distance of 20 µm.

The WS_2 flakes were grown on the SiO_2/Si substrate by Minpeng Liang at the University of Groningen. Monolayer WS_2 was obtained by means of the molten-salt-assisted CVD method, previously described by Zhou et al. [229]. The growth procedure started with the mixing of metal precursor WO_3 in a powder form with NaCl salt. The NaCl salt plays two important roles. First, it reduces the melting point of a tungsten precursor WO_3. Additionally, the reaction product of NaCl with WO_3 (i.e. tungsten oxychloride) facilitates the process of TMD flake formation. The compound mixture was placed in an aluminum oxide boat and put in a quartz tube inside a furnace. The sulfur precursor powder was placed in another boat in the furnace upstream. The Ar mixed with H_2 was used as a carrier gas. The growth temperature for WS_2 was about 750 °C to 850 °C and the growth process lasted around 3 minutes. The high growth rate facilitated the formation of large (on the order of 30 µm) monolayer WS_2 flakes, as shown in Figure 2.2.

After the TMD and perovskite synthesis were completed, the next step of the stack fabrication was the mechanical exfoliation of hBN and PEPI crystals, conducted by Minpeng Liang at the University of Groningen. The exfoliation was carried out using Scotch tape in a glovebox filled with Ar gas. The levels of H_2O and O_2 were kept low (less than 0.1 ppm) in order to prevent material contamination and degradation.

An atomic force microscopy (AFM) image collected in ambient conditions enabled the assessment of the quality of the exfoliated perovskite flakes. The AFM image (provided by Minpeng Liang) of one of the exfoliated PEPI flakes is shown in Figure 2.3. The measured surface area was 5 µm x 5 µm. The step-like features indicate that the regions of the perovskite flake exhibited different thicknesses.

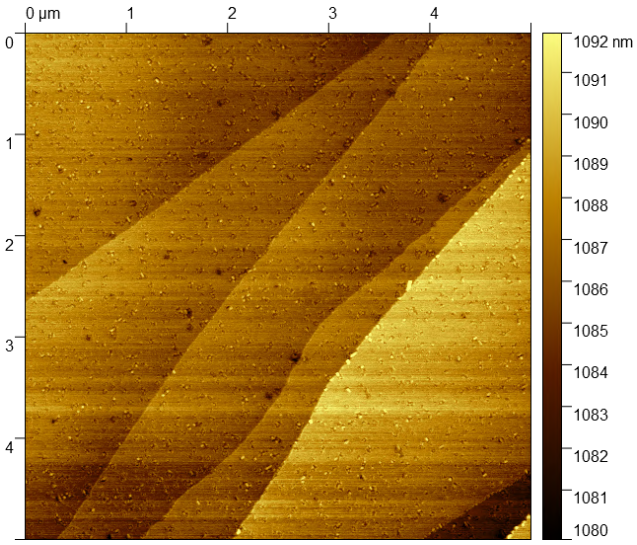

Figure 2.3: The AFM image of one of the exfoliated PEPI perovskite flakes. The image was collected in ambient conditions following the mechanical exfoliation of PEPI. The color bar indicates different heights of the flake.

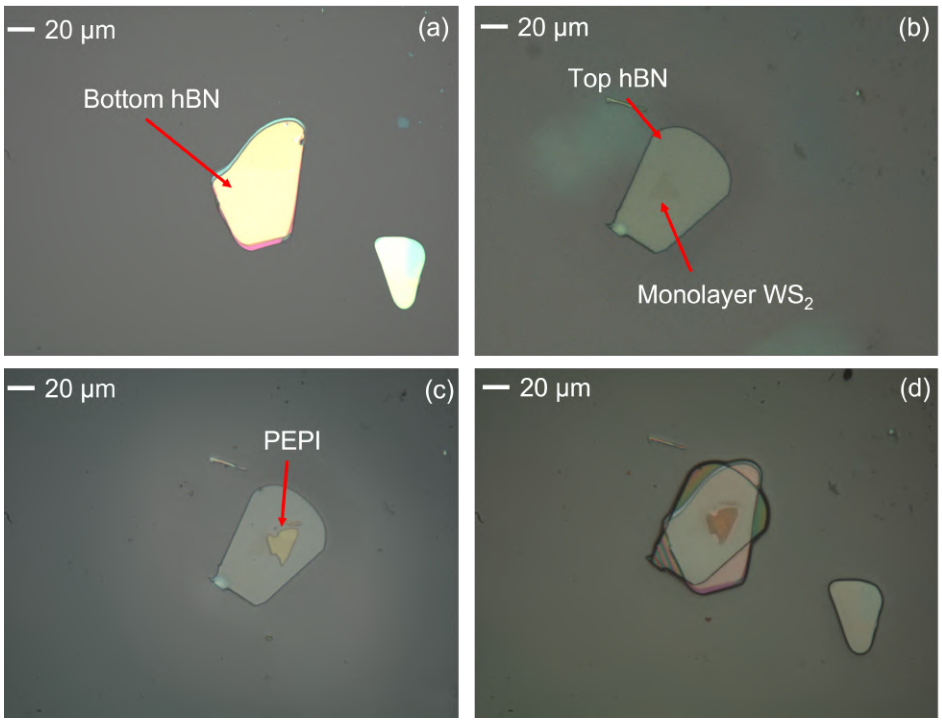

Figure 2.4: The process of PEPI/WS_2 stack preparation. (a) - The bottom hBN flake is placed on the SiO_2/Si substrate. (b) - The WS_2 flake is stamped on the top hBN flake. (c) - The PEPI flake is stamped on WS_2. (d) - The structure is stamped on the bottom hBN flake. The white horizontal bars indicate the distance of 20 µm. The red arrows indicate the respective flakes.

The stages of PEPI/WS_2 stack preparation are shown in Figure 2.4. The stack fabrication was performed by Minpeng Liang at the University of Groningen. First, the bottom hBN flake was placed on the SiO_2/Si substrate (panel (a)). Next, the top hBN flake was picked up

by a stamp covered in polycarbonate film (PC) and heated up to 80 °C. The hBN was then used to lift WS_2 at 110 °C - (panel (b)). In the following step, the PEPI flake was picked up at 40°C - (panel (c)). Finally, the structure was stamped on the bottom hBN flake, as shown in panel (d). Heating up the PC-covered stamp ensured strong adhesion between the subsequent flakes. In the end, chloroform was used to dissolve the remnants of the PC film from the stack.

2.3 PEPI/$MoSe_2$ and BAPI/$MoSe_2$

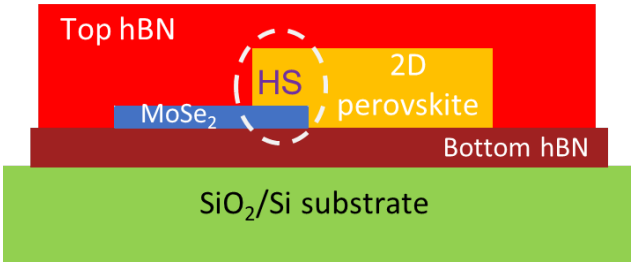

Figure 2.5: The schematic diagram of PEPI/$MoSe_2$ and BAPI/$MoSe_2$ stacks. The HS region is indicated by a white dashed oval.

The schematic structure of PEPI/$MoSe_2$ and BAPI/$MoSe_2$ stacks is shown in Figure 2.5. The PEPI or BAPI perovskite flake (yellow color) partly covered the monolayer $MoSe_2$ flake (blue), allowing optical access to the bare flakes and the HS region (white dashed oval). Each stack was sandwiched between the top (red) and bottom (brown) hBN flakes and placed on separate SiO_2/Si substrates (green).

The PEPI crystals were synthesized by Matan Menahem from the Weizmann Institute of Science. The growth of PEPI single crystals was conducted using a different method than the one described in Section 2.2. The procedure, based on Ref. [230], was described in detail in Ref. [231]. Briefly, the lead precursor PbO was dissolved in a mixture of HI and H_3PO_2. The solution was then heated up to 110 °C and mixed with PEA neutralized by HI. During the cooling process of this mixture to room temperature at a rate of 2 K/hour, the PEPI plate-like single crystals were grown. In the end, the crystals were washed in diethyl ether and dried in the vacuum oven.

The synthesis of BAPI perovskite was developed and performed by Pabitra Nayak at the University of Oxford. In this method, butylammonium iodide was first mixed with PbI_2 in a chlorinated solvent. A suspension was formed to which a solution of primary amine was added. The mixture was then heated up to 55 °C. The process of crystal formation started after staying for several minutes at this temperature. After the synthesis, the solvent was evaporated and orange BAPI crystals with sizes on the order of several mm were collected.

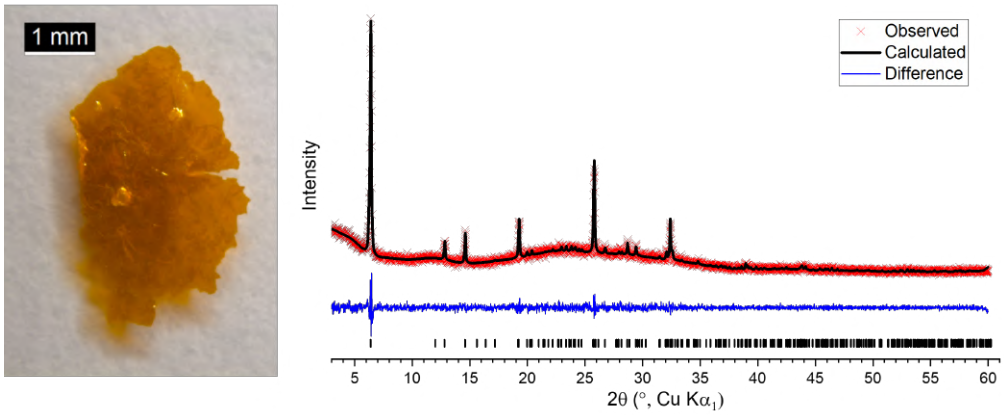

Figure 2.6: Left panel - Image of the as-synthesized BAPI crystal. The white horizontal bar represents the distance of 1 mm. Right panel - Pawley fit (black curve) of the powder XRD data (red crosses) to the reported BAPI crystal phase (black vertical lines). The difference between the calculated and observed curves is shown as a blue curve.

The image of the as-grown BAPI crystal is shown in the left panel in Figure 2.6.

Powder X-ray diffraction (XRD) was conducted in order to determine the crystal structure and assess the purity of the BAPI crystal. The XRD experiment was performed by Harry Sansom from the University of Oxford. The results of XRD measurements are shown in the right panel in Figure 2.6. The Pawley fit (black curve) of the XRD data (red crosses) was calculated with TOPAS-Academic V7 software. A Pawley fit is obtained by using known unit cell parameters of the material as initial parameters. The fitted peak positions are then adjusted by changing the unit cell parameters. The blue curve in Figure 2.6 represents the difference between the calculated profile based on the experimental data and the reported data of BAPI structure [232]. The unit cell parameters obtained from the fit enabled to determine that BAPI perovskite crystallizes in an orthorhombic system which agrees well with the literature [178, 232]. The absence of additional peaks in the XRD data implies that the impurity phases are not present.

After the synthesis, the TMD, perovskite and hBN flakes were exfoliated from their respective bulk crystals using the method developed by Castellanos-Gomez et al. [233]. Namely, the flakes were transferred to a polydimethylsiloxane (PDMS)-covered glass to reduce the possibility of flake contamination by the Scotch tape, and stamped one on top of the other. The exfoliation and stacking of PEPI/$MoSe_2$ and PEPI/$MoSe_2$ stacks were conducted by Jonas Ziegler at the University of Regensburg.

The optical microscope images of the subsequent transfer steps are shown in Figure 2.7 for PEPI/$MoSe_2$, and in Figure 2.8 for BAPI/$MoSe_2$ stack. For both samples, the bottom hBN flake was first exfoliated at ambient conditions on PDMS. Then, it was stamped on the

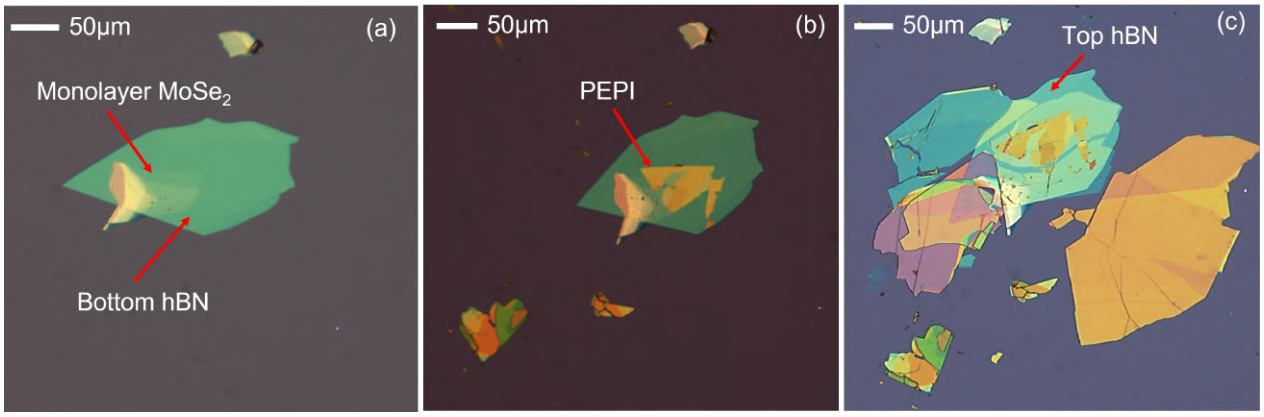

Figure 2.7: The process of PEPI/$MoSe_2$ stack fabrication. (a) - The bottom hBN was exfoliated and stamped on SiO_2/Si substrate. Then, the $MoSe_2$ flake was stamped on the bottom hBN. (b) - The PEPI flake was stamped on top of $MoSe_2$. (c) - The top hBN flake was stamped on top of the rest of the structure. The horizontal bars represent a distance of 50 μm. The red arrows indicate the respective flakes.

SiO_2/Si substrate, previously heated to 90 °C to facilitate the flake adhesion (panel (a) in Figure 2.7 and 2.8). Subsequently, the hBN was annealed at 180 °C for around 1-2 hours. The annealing was carried out to increase the interface homogeneity between the hBN and the substrate. Thermal treatment enabled also the removal of the organic remnants from the stamp and any other contaminants that aggregate into bubbles on the surface of the flakes during the transfer process [234]. In the next step, the $MoSe_2$ flake was exfoliated on PDMS,

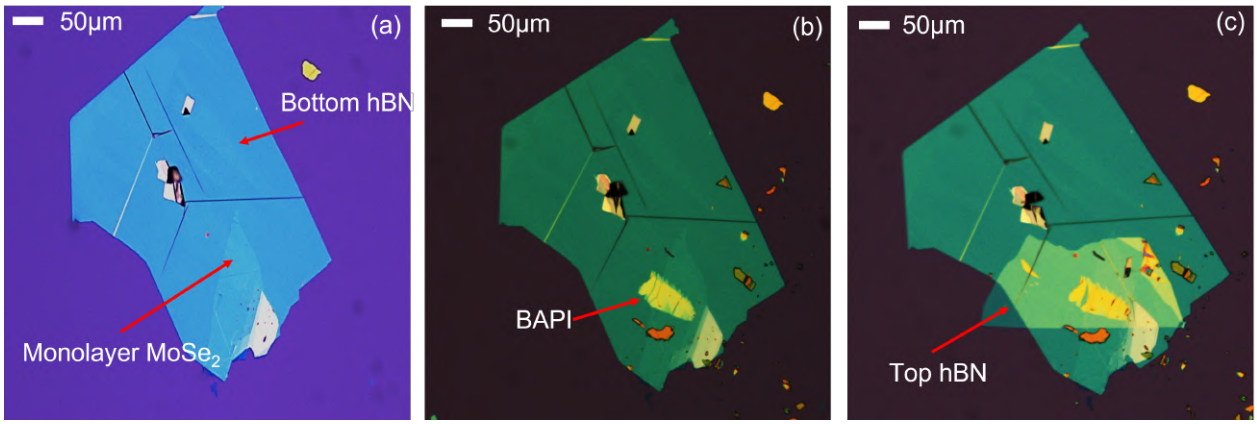

Figure 2.8: The process of BAPI/$MoSe_2$ stack fabrication. (a) - The bottom hBN was exfoliated and stamped on SiO_2/Si substrate. Then, the $MoSe_2$ flake was stamped on the bottom hBN. (b) - The BAPI flake was stamped on top of $MoSe_2$. (c) - The top hBN flake was stamped on the rest of the structure. The horizontal bars represent a distance of 50 μm. The red arrows indicate the respective flakes.

followed by stamping on the bottom hBN flake at 70 °C and annealing at 150°C for about 2 to 3 hours. Then, the PEPI or BAPI perovskite was exfoliated from its respective bulk

crystal and stamped on the $MoSe_2$ flake (panel (b) in Figure 2.7 and 2.8. Care was taken to only cover a part of the $MoSe_2$ flake. No additional heating was used in order to prevent the thermal degradation of perovskites. In the end, the encapsulation with the top hBN flake was immediately performed without further annealing (panel (c) in Figure 2.7 and 2.8).

Experimental methods

In this Chapter, I discuss the experimental methods that were used to study van der Waals stacks presented in this thesis. I begin with a description of steady-state optical spectroscopy setups. In the subsequent section, I present the details of optical spectroscopy experiments in the time domain.

3.1 Steady-state optical spectroscopy

3.1.1 Introduction

The absorption transitions of the samples were studied in the RL and the emission transitions - in the PL experiments. The RL and PL spatial mapping techniques were used to study the optical response as a function of position in the plane of the stack. Finally, I used the photoluminescence excitation (PLE) method to investigate the potential excitation transfer between the constituent materials of the stack.

The measurements were performed at the Institute of Physics Polish Academy of Sciences in Warsaw, the National Laboratory of High Magnetic Fields in Toulouse and at the Faculty of Fundamental Problems of Technology at the Wroclaw University of Technology.

Before going into a detailed description of the experimental methods, I will first discuss the general features of the steady-state spectroscopy setup. It is important to note that different experimental setups were used in the laboratories mentioned above. In Figure 3.1, I present the schematic diagram that shows all of the employed experimental techniques. The colored dashed boxes indicate the following parts of the steady-state spectroscopy equipment: I - sample placed in a cryostat (enclosed by the blue dashed box), II - excitation part (green box), III - spatial filter (violet box), IV - sample visualization (brown box), V - detection part (red box) and VI - data processing equipment (cyan box).

All experiments were carried out at a temperature of 5 K. The samples were glued with a silver paste on a cold finger of liquid helium-cooled cryostat (shown in the blue box in

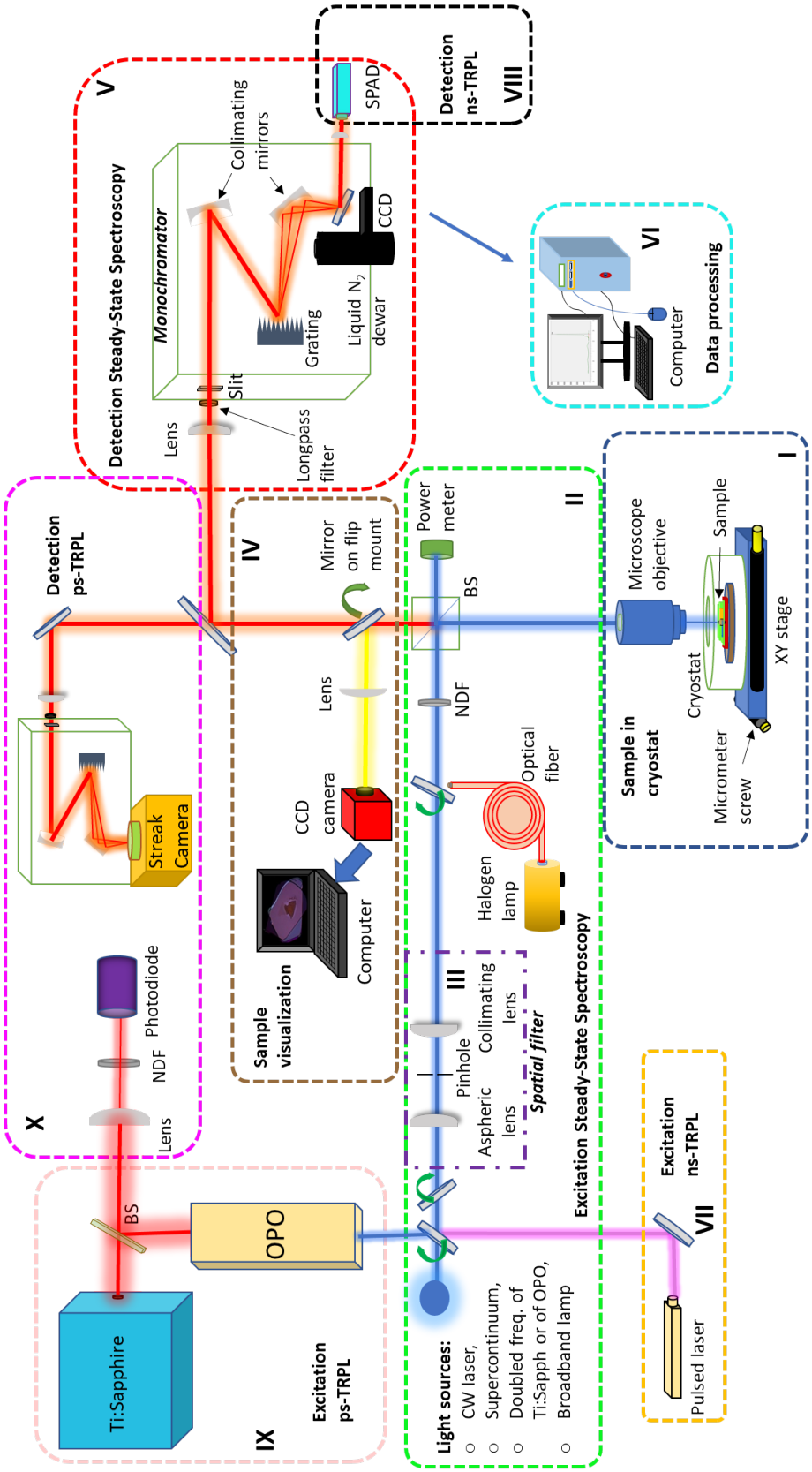

Figure 3.1: General scheme representing the employed experimental techniques.

Figure 3.1). The role of the silver paste, apart from fixing the sample position, was to ensure good thermal contact for the uniform cooling of the sample. The cryostat screwed through the transfer tube to the helium storing dewar allowed the measurements in the temperature range from 4 K to 300 K. Cold finger was connected to the rhodium-iron resistance sensor which enabled monitoring of the sample temperature via the temperature controller. To adjust the position of the incident beam on the sample, the cryostat was mounted on an XY motorized stage moved either manually or by computer-manipulated microscrews with a minimum step size of 100 nm.

To carry out the optical experiments in the selected region of the stack, the visualization of the sample surface was required. A halogen lamp was used for illumination for the real-time observation of the sample. The sample image was produced on a CCD camera connected to the computer (shown in brown box in Figure 3.1). An example of the sample image is shown on the screen of the schematic computer in the brown box.

The experiments were conducted in the free beam backscattering geometry where the excitation signal to and the detection signal from the sample propagated along the same path but in opposite directions. The incident beam was reflected by a set of silver mirrors and by either 50:50 or 30:70 non-polarizing beamsplitter (BS), shown in the green box. The power of the excitation laser beam was monitored on the power meter placed behind the BS, and controlled by a variable neutral density filter (NDF). The beam was focused on the surface of the sample with a microscope objective with a numerical aperture of 0.5 or 0.55 with a focal length of 3.6 mm or 2 mm, respectively, and a working distance of 13 mm.

The detection signal was collected by the same microscope objective as the one used for excitation and directed to the lens that focused the beam on the entrance of either 0.3 m- or 0.5 m-long monochromator (red box). A longpass edge filter was used to eliminate the exciting laser light. Inside a monochromator, the photons were reflected off the collimating mirror and dispersed by the 300 or 600 l/mm grating. Finally, the beam was focused on either an electrically- or liquid nitrogen-cooled CCD camera.

3.1.2 PL spectroscopy

In the PL experiment, the following excitation sources were used: (i) continuous wave (CW) laser diode with excitation wavelength (λ_{exc}) of 473 nm, (ii) CW gas laser with λ_{exc} = 488 nm, (iii) CW single-mode fiber-coupled laser diode with λ_{exc} = 633 nm, (iv) CW laser diode with λ_{exc} = 640 nm, (v) frequency-doubled output of tunable mode-locked Ti:sapphire laser (λ_{exc} tunable from 340 nm to 540 nm) or (vi) frequency-doubled output of the optical parametric oscillator (OPO) synchronously pumped by Ti:sapphire (λ_{exc} tunable from

500 nm to 800 nm).

To achieve a diffraction-limited spot size on the order of 1 µm, it is necessary to work with a single-mode Gaussian beam. Since most of the sources used in the experiments were multimode, the excitation beam was first guided through a spatial filter (shown in the violet box in Figure 3.1) before being directed to the sample. In a spatial filter, the beam was focused by an aspheric lens on a pinhole with a diameter of 20 µm, and collimated by the second lens placed behind the pinhole. This ensured that the external parts of the beam containing higher modes were cut out from the fundamental Gaussian mode. The beam diameter of $\sim$ 1 µm was at least an order of magnitude smaller than the dimensions of the constituent flakes in the studied van der Waals stacks. Therefore, their properties could be probed separately with small crosstalk only close to the flake edges.

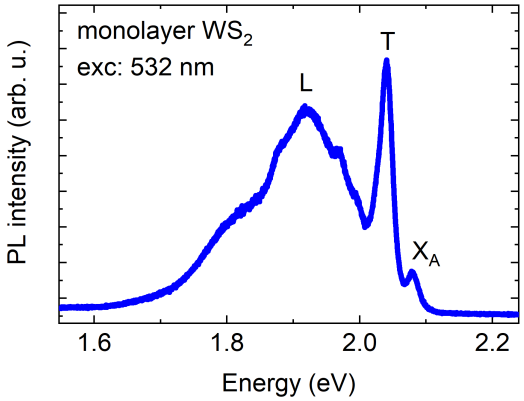

Figure 3.2: The PL spectrum of monolayer WS_2 encapsulated in hBN.

The typical PL spectrum in the hBN-encapsulated monolayer WS_2 at $\sim$ 5 K is shown in Figure 3.2. The observed peaks correspond to the neutral (X_A), charged (T) and localized (L) excitons.

3.1.3 RL spectroscopy

In the RL experiment, the sample was illuminated with broadband white light from either a tungsten halogen lamp (low energy spectral range 500 nm - 800 nm) or a xenon lamp (high energy spectral range 450 nm - 550 nm).

Due to the chromatic aberrations of the lenses and microscope objective, it is a challenge to focus white light into a spot of a size of $\sim$ 1 µm. To minimize the illumination area on the sample, the white light was collected from the lamp with an optical fiber with a core diameter of either 50 µm or 200 µm. When using the fiber with a core diameter of 200 µm, the beam was guided through the spatial filter and focused with a microscope objective as in the PL experiment. Alternatively, the white light was collimated with a lens with a long

focal length ($f_{lens} = 150$ mm) and focused with a microscope objective ($f_{obj} = 3.6$ mm). This way, the image of the fiber end on the sample was compressed by a factor of $f_{lens}/f_{obj} \sim 42$. In the following subsection, I will estimate the white light spot size in the RL experiment.

The samples studied in this thesis are partly reflective multilayer stacks deposited on a thin (thickness on the order of λ_{exc}) SiO_2 layer on a reflective silicon substrate. The light that is reflected at the interface between the constituent materials of the stack undergoes either constructive or destructive interference. As a result, the raw RL spectrum consists of the response of the sample superimposed on broad Fabry-Perot oscillations. To disentangle the RL signal of the sample from the raw RL response, I calculate the reflectance contrast (RC) [82, 235, 236]:

$$RC = \frac{R - R_{bg}}{R_{bg}}, \tag{3.1}$$

where R is the as-measured RL spectrum and R_{bg} is the background reflectance.

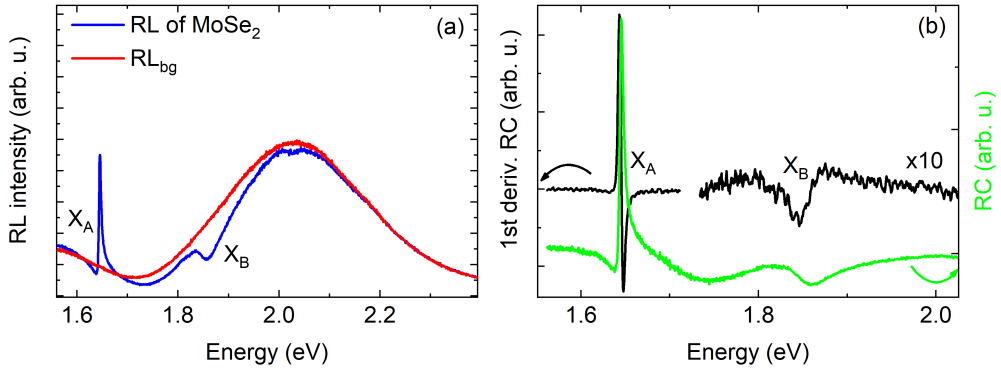

Figure 3.3: (a) - The RL spectrum in monolayer $MoSe_2$ encapsulated in hBN (blue curve). The background RL spectrum collected on hBN is shown as a red curve. (b) - The RC spectrum (green curve) and the first derivative RC spectrum (black curve). The part of the first derivative RC spectrum showing the X_B transition was multiplied by 10 for clarity.

An example of the RL spectrum at 5 K collected in monolayer $MoSe_2$ encapsulated in hBN is shown in Figure 3.3 (a) as a blue curve. The background spectrum (red curve) showing a broad Fabry-Perot oscillation was measured on hBN on the SiO_2/Si substrate. In Figure 3.3 (b), the RC spectrum calculated based on Eq. 3.1 and its first derivative are shown as a green and black curve, respectively. The absorption transitions of X_A (exciton A) and X_B (exciton B) can be clearly distinguished.

3.1.4 Spatial mapping

In the spatial mapping technique, the emitted or reflected signal was raster-scanned over a specified sample area. The mounting of the cryostat on the linear XY translation stage

enabled the change of the beam position on the sample. The microscrews attached to the stage were operated by stepper motors, and they moved the cryostat by a defined scanning step. The PL (RL) spectrum was measured at every step and through the appropriate data processing the PL (RL) spatial map was obtained. The excitation or detection setup in the PL and RL spatial mapping experiments was the same as in the PL and RL experiments, respectively. The scanning step was 1 µm and the scanning area was on the order of 50 µm x 50 µm. To reduce the error due to motor backlash, the scanning was conducted in one direction.

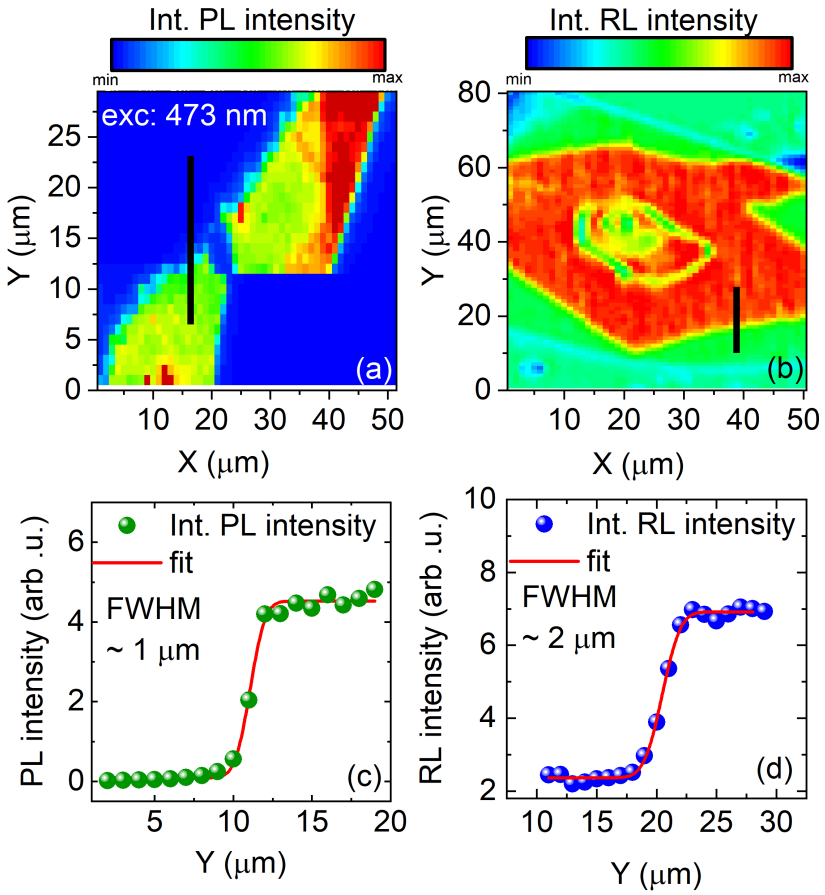

Figure 3.4: (a) - The PL intensity map of two PEPI flakes encapsulated in hBN. (b) - The RL intensity map of PEPI/MoS_2 stack encapsulated in hBN. The black lines indicate the areas on the samples from which the PL and RL spectra were extracted in order to estimate the beam size. (c) - Spatial intensity profile (green spheres) extracted from the PL intensity map in (a) along the black line. (d) - Spatial intensity profile (blue spheres) extracted from the RL map in (b) along the black line. The profiles were fitted with Eq. 3.2 (red curves). From the fits, the FWHM of the laser and white light beam was estimated to be around 1 and 2 µm, respectively.

An example of a low temperature ($\sim$ 5 K) PL intensity map of two PEPI flakes encapsulated in hBN is presented in Figure 3.4 (a). The map shows the integrated PL

intensity from 2.340 eV to 2.350 eV and enables the observation of the changes in the PL intensity throughout the perovskite flakes. In Figure 3.4 (b), I present an example of a room temperature RL intensity map of PEPI/MoS_2 stack encapsulated in hBN. The map shows the integrated RL intensity from 1.90 eV to 1.96 eV.

Apart from giving information about the optical response of the sample, the spatial mapping experiment can be used to estimate the size of the excitation laser or illumination white light spot on the sample. The spatial profile of the PL or RL signal is a convolution of a Gaussian profile G(x) of the beam and the Heaviside step function H(x) describing the substrate-flake interface:

$$I(y) = G(x) * H(x) = \ Ac\sqrt{(\pi/2)}(1 - \mathrm{erf}((x_0 - y)/(c\sqrt{2})), \tag{3.2}$$

where the spatial profile of the beam is given by

$$G(x) = \ A\mathrm{exp}(-x^2/(2c^2). \tag{3.3}$$

and

$$H(x) = \begin{cases} 0 & \text{for } x < x_0 \\ 1 & \text{for } x \geq x_0, \end{cases} \tag{3.4}$$

where the x_0 parameter represents the position of the flake edge. The A is the maximum intensity of the Gaussian profile and the c parameter is related to the full-width-at-half-maximum (FWHM) of the Gaussian profile by relation:

$$\mathrm{FWHM} = 2c\sqrt{\ln(2)} \tag{3.5}$$

To calculate the beam size, I analyze the spatial profiles of the PL or RL signal obtained from the maps shown in Figure 3.4. The regions of profile extraction are indicated by black lines in Figure 3.4 (a) and (b). The spatial profiles (green spheres in Figure 3.4 (c) and blue spheres in (d)) are fitted with Eq. 3.2 (red curves in (c) and (d)). The obtained parameters c are used to estimate the beam sizes in both experiments using Eq. 3.5. The estimated laser spot is $\sim$ 1 µm and the white light beam spot is $\sim$ 2 µm. Therefore, the white light spot is only 2 times larger than the laser spot.

3.1.5 PL excitation

In the PLE experiment, the PL spectra are collected while tuning the excitation photon energy. The experiment was conducted on the same setup as the PL experiment. The

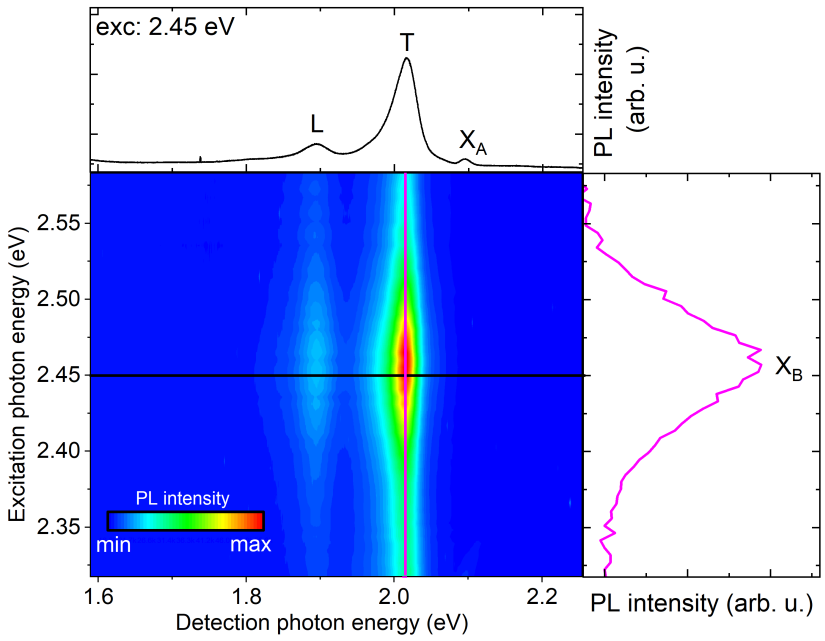

Figure 3.5: The false color map showing the PL spectra in monolayer WS_2 encapsulated in hBN as a function of the excitation photon energy. The color scale represents the emission intensity with red being the highest and blue - the lowest PL intensity. The PL spectrum excited at 2.45 eV is shown in the panel above the map. The PL intensity of the T peak (as a function of the excitation energy) is presented in the panel on the right side of the map. The black horizontal and pink vertical lines indicate at which excitation and detection energy, respectively, the spectra in the top and right panels were extracted.

excitation source was: (i) frequency-doubled output of Ti:sapphire, (ii) frequency-doubled output of OPO, or (iii) white light supercontinuum generated in the range from 450 nm to 2000 nm. The spectral resolution of the experimental setup determined by the spectral bandwidth of the source was: $\sim$ 1 nm for (i) and $\sim$ 2 nm for (ii). In case (iii), the white light beam passed through the 0.3 m-long monochromator. In this case, the spectral resolution was dictated by the monochromator output slit and was $\sim$ 1 nm.

In Figure 3.5, I present a false color map showing the PL spectra in the hBN-encapsulated monolayer WS_2 as a function of the excitation energy. In the panel above the map, the PL spectrum extracted from the map at the excitation energy of 2.45 eV is presented. The peaks of the neutral (X_A), charged (T) and localized (L) excitons can be clearly distinguished. The PLE spectrum of T is presented in the right-side panel. A peak with the maximum at $\sim$ 2.45 eV corresponds to the excitation via exciton B (X_B).

3.2 Time-resolved PL spectroscopy

In the time-resolved PL (TRPL) experiments, I used two different methods with different detection devices. In the experiment in nanosecond time scale (ns-TRPL) the detector was a single photon avalanche photodiode (SPAD). In the picosecond scale (ps-TRPL), a streak camera was used. In Figure 3.1, the excitation and detection part of the ns-TRPL setup is enclosed by yellow and black boxes, respectively. The excitation (detection) section in the ps-TRPL setup is shown in the pink (magenta) box.

3.2.1 Nanosecond time domain

In the ns-TRPL experiment, the excitation source was a pulsed laser diode emitting at $\lambda_{exc} = 400$ nm with a pulse width of 70 ps and tunable repetition frequency from 2 Hz to 100 MHz. In Figure 3.6, I present the laser pulse profile based on which the overall temporal resolution of the setup was estimated to be ~ 1 ns. To ensure that the emission signal from the sample fully decayed back to the background level before the next incoming laser pulse, I have chosen the repetition frequency of 200 kHz.

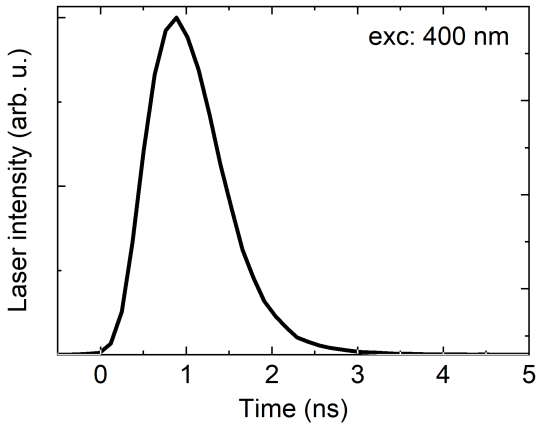

Figure 3.6: Temporal profile of a pulsed laser with $\lambda_{exc} = 400$ nm.

The silicon SPAD (shown in the black box in Figure 3.1) was used as a detector. The SPAD is a semiconducting photodetector device based on a pn junction with an applied reverse bias, i.e. negative potential is connected to the electron-deficient p-type semiconductor part. The schematic diagram of SPAD is presented in Figure 3.7. An active area (which is a charge depletion region) is located in the central part of the device, where incoming photons generate electron-hole pairs. The reverse bias in SPAD is usually larger than the breakdown voltage which creates a large electric field across the junction. The absorption of a single photon can, thus, start a self-sustaining avalanche of atomic ionization which quickly increases the current to the macroscopic levels. The swiftly reduced bias

voltage quenches the avalanche and prevents the destruction of the device. The return of the bias to the level before the photon absorption makes SPAD ready for the next incoming photon. In the ns-TRPL experiments, the active area diameter of SPAD was 180 µm with a dead time of 22 ns and the photon detection efficiency at 650 nm of 65 %.

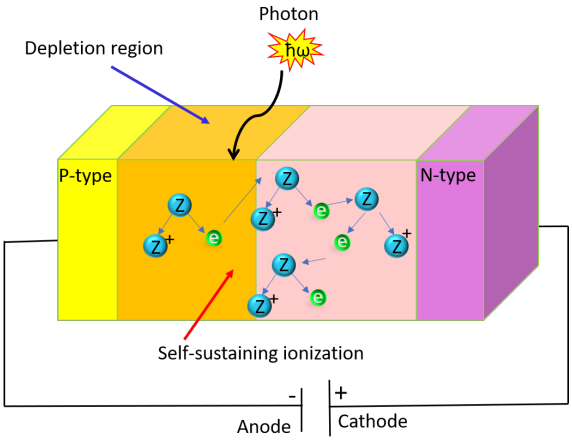

Figure 3.7: Schematic diagram of SPAD. The $\hbar\omega$ is the photon energy. The green spheres represent electrons. The blue spheres indicate neutral atoms and the + superscript indicates cations.

Time-Correlated Single Photon Counting (TCSPC) system was used to resolve the PL signal in the time domain. The dynamics was measured in the following way. First, an electrical excitation pulse from the laser driver entered one channel of TCSPC. The arrival of the pulse at time t_0 triggered the start of time measurement. Following the photon detection, an electrical pulse from SPAD entered the second channel of TCSPC unit at time t_1, stopping the measurement. This way, the TCSPC unit built a histogram of the number of photons in time intervals $t_1 - t_0$. The histogram represented the PL decay.

It is important to note that in the ns-TRPL experiment, the SPAD was placed behind the monochromator which allowed the selection of the detection wavelength. Before the measurements in the time domain, the PL spectrum was first collected by directing the signal to the CCD camera by the rotating mirror placed at the end of the monochromator (red box in Figure 3.1). The collected PL spectrum enabled the assessment of the sample optical response before the time-resolved experiment.

3.2.2 Picosecond time domain

In the ps-TRPL experiment, a streak camera was used as a detector. An important advantage of the streak camera over SPAD is not only the possibility to probe the signal on shorter time scales (on the order of ps) but also to simultaneously obtain a time- and spectrally-resolved PL intensity distribution.

For excitation, I used the frequency-doubled output of OPO. The repetition rate of Ti:sapphire used to pump OPO was 80 MHz. The temporal resolution of the setup determined by the excitation pulse jitter was $\sim$ 34 ps.

In the ps-TRPL, a Ti:sapphire pulse passed through a beamsplitter to a p-i-n photodiode (PD) and was reflected towards the entrance of OPO (pink box in Figure 3.1). The PD was connected with the delay unit that generated a trigger pulse for the sweep unit in the streak camera. The output of OPO was directed to the sample and the signal from the sample was dispersed by a monochromator and entered through the slit to the streak camera (magenta box in Figure 3.1).

The schematic diagram of the streak camera operation is shown in Figure 3.8. The adjustable slit was used to control the temporal resolution of the system. Behind the slit, a set of lenses focused the signal on the photocathode, where photons were converted to electrons. These photoelectrons were then accelerated by a constant electric field generated by an accelerating mesh. The electron stream was guided toward the sweep unit where a sinusoidal high voltage (triggered by the pulse from PD) was applied to the sweep electrodes. The generated alternating electric field deflected the electrons at an angle depending on their

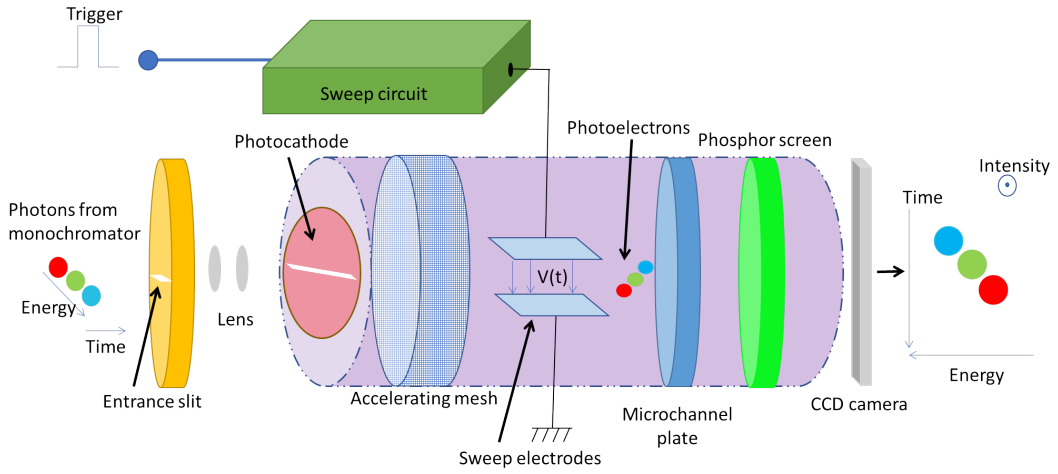

Figure 3.8: Operation principle of the streak camera.

time of arrival in the direction perpendicular to their original flight path. The electrons were then directed to a microchannel plate, where their number was multiplied. Finally, the electrons were converted back to photons on the phosphor screen. The CCD camera was used to image the generated photons. This experimental setup enabled the collection of the streak image representing the PL intensity as a function of wavelength and time.

In Figure 3.9, I present an example of the streak camera image in monolayer WSe_2 encapsulated in hBN. Time-integrated PL spectrum showing the neutral (X_A) and charged (T) exciton is presented above, and a spectrally integrated PL decay of X_A - on the right

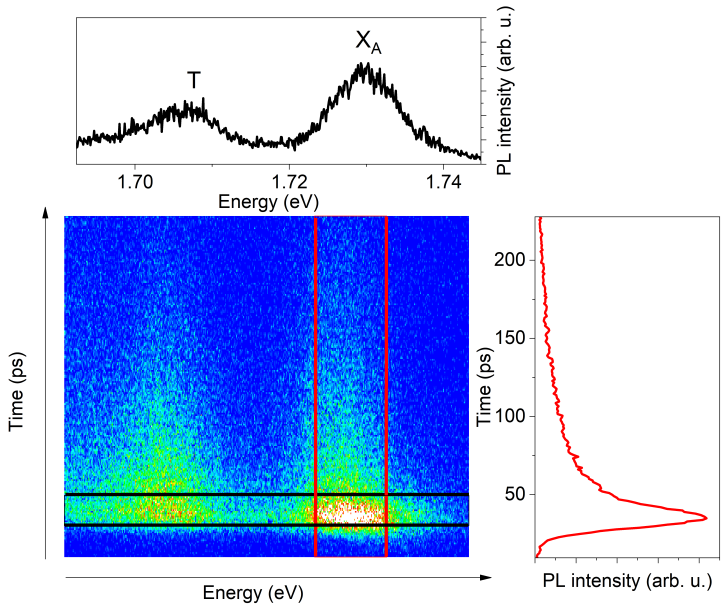

Figure 3.9: The streak image at 5 K in monolayer WSe_2 encapsulated in hBN. Time-integrated PL spectrum is shown above the image and a spectrally integrated signal (PL decay) is presented on the right side of the image. The black horizontal and red vertical lines indicate the integration range for the PL spectrum and the PL decay, respectively.

side of the image. Both plots were acquired from the same streak image by integrating a temporally resolved signal between the black horizontal lines (PL spectrum) and a spectrally resolved signal between red vertical lines (PL decay).

Sample characterization

In this Chapter, I will present the results of the characterization of the invesitgate heterostructures. The employed experimental techniques include optical microscopy, reflectance and photoluminescence spectroscopy.

4.1 Introduction

The aim of this Chapter is to discuss the RL and PL spectra of the constituent materials and identify the observed PL peaks. The optical characterization provides also information about the quality of the samples.

After synthesis and fabrication of PEPI/WS_2, PEPI/$MoSe_2$ and BAPI/$MoSe_2$ stacks, the quality of each sample was examined with an optical microscope. In particular, the presence of contaminants potentially introduced during the stacking procedure was investigated by this technique. The optical microscope studies were conducted by Minpeng Liang from the University of Groningen (PEPI/WS_2 stack) and by Jonas Ziegler from the University of Regensburg (PEPI/$MoSe_2$ and BAPI/$MoSe_2$ stacks).

The RL and PL techniques were used to identify the excitonic transitions in three characteristic regions in each stack, i.e. bare TMD - WS_2 and $MoSe_2$ (where monolayer TMD is in contact with hBN from the top and bottom side), bare 2D perovskite - PEPI and BAPI (where 2D perovskite is in contact with hBN from the top and bottom side), and the HS region (where TMD is in contact with 2D perovskite from one side and hBN from the other side). The experimental data presented in this Chapter will be analyzed in Chapters 5 and 6 from the point of view of the potential excitation transfer.

4.2 PEPI/WS_2

4.2.1 Optical microscopy

The microscope image of PEPI/WS_2 stack, provided by Minpeng Liang from the University of Groningen, is presented in Figure 4.1. The blue and green broken lines enclose the PEPI and WS_2 flakes. The HS region is pointed by the black arrow. The blue, green and black dots roughly indicate places of the RL and PL spectra collection on bare PEPI, bare WS_2 and the HS region, respectively.

The estimated dimensions of each part of the stack are as follows: PEPI flake with a roughly triangular shape - each side is $\sim$ 30 µm long, equilateral triangular monolayer WS_2 flake - each side is $\sim$ 25 µm long, the hBN flakes have dimensions of $\sim$ 80 µm x 50 µm and the HS region $\sim$ 15 µm x 3 µm. Uniform optical contrast indicates that the surface of the constituent flakes is mostly flat with no wrinkles or holes.

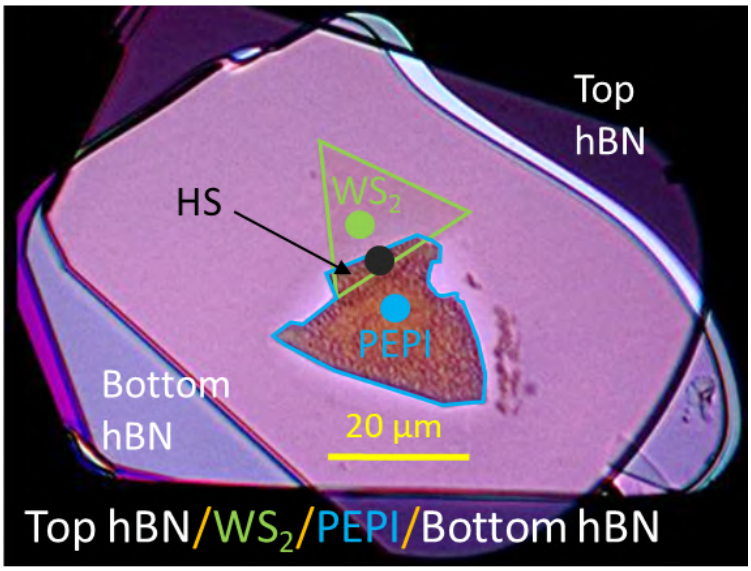

Figure 4.1: Optical microscope image of PEPI/WS_2 stack. The blue and green broken lines encircle the PEPI and WS_2 flakes, respectively. The yellow horizontal bar represents a distance of 20 µm. The blue, green and black dots indicate the places, where the PL and RL spectra were collected.

4.2.2 Reflectivity in WS_2

In stacks composed of thin films the light that is partially reflected at the boundaries between different materials undergoes either constructive or destructive interference [237]. The interference depends on the phase difference between the light waves reflected at the

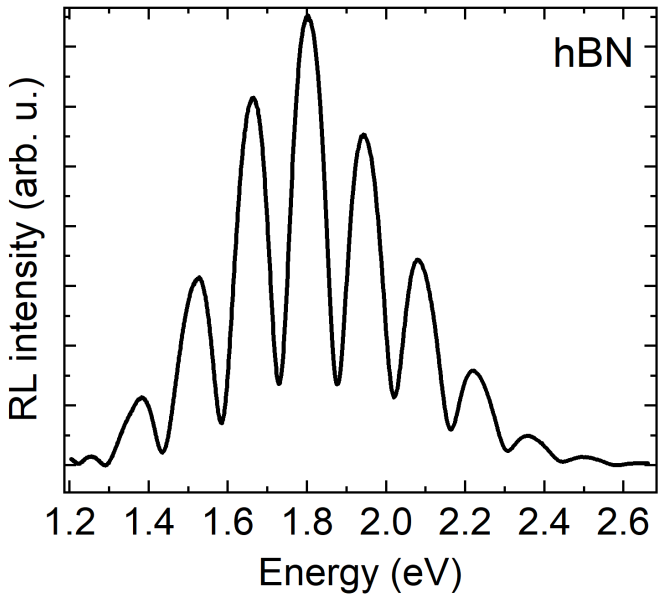

Figure 4.2: The RL spectrum collected on hBN in PEPI/WS_2 stack.

interfaces which is determined by the angle of light incidence, the thickness of the film and the refractive indices of the film and surrounding material. In PEPI/WS_2 stack, the interference of the reflected light resulted in the appearance of very strong oscillations, as presented in the RL spectrum in Figure 4.2. The spectrum was collected in the spot, where top and bottom hBN flakes are in contact. As the intensity and positions of the observed oscillations strongly depended on the position on the sample, I could not collect the appropriate background spectrum which is required to calculate the reflectance contrast (RC). To extract the absorption transition energies in PEPI/WS_2 stack, I subtract the background contribution from the as-measured RL spectra and calculate the first derivative. The transition energies are found in the inflection point of the first derivative RL spectrum.

The first derivative RL spectra on bare WS_2 and in the HS region in PEPI/WS_2 stack are presented in Figure 4.3 as the green and black curves, respectively. On bare WS_2, I observe the absorption transition at $\sim$ 2.07 eV. According to the literature, the absorption energy of the exciton A (X_A) in monolayer WS_2 placed on SiO_2/Si substrate is $\sim$ 2.1 eV [238]. As I discussed in Chapter 1, the dielectric environment influences the energy of excitonic transitions in atomically thin materials such as monolayer TMDs. When monolayer TMD is in contact with a material with a lower dielectric constant (ϵ), such as air, vacuum or SiO_2 film, the excitons generated in TMD are subjected to the weak dielectric screening in the out-of-plane direction. The reduced screening increases the strength of the electron-hole interaction resulting in the increased exciton binding energy (E_b) and bandgap (E_g^{mono}) in monolayer TMD [44]. As the exciton energy is given by a difference $E_g^{mono} - E_b$, the relative changes of these two values will determine either an increase or decrease of the exciton

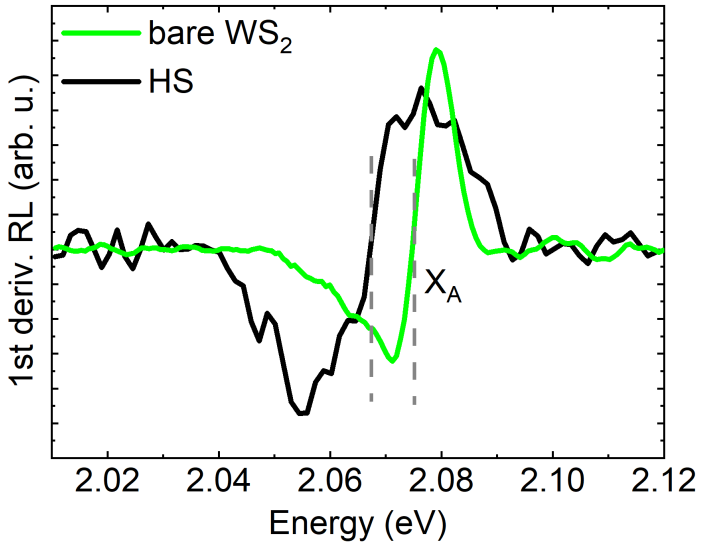

Figure 4.3: The first derivative RL spectra on bare WS_2 (green curve) and in the HS region (black curve). Grey dashed lines are guides for the eye.

energy [44, 115]. In PEPI/WS_2 stack, monolayer WS_2 is encapsulated by hBN flakes that have a larger dielectric constant ($\epsilon = 4.35$ [115]) than vacuum ($\epsilon = 1$) and SiO_2 ($\epsilon = 2.1$ [44]). Therefore, the change of the X_A transition energy in the hBN-encapsulated WS_2 with respect to WS_2 on SiO_2 (due to the change of dielectric environment) is expected.

I will now check if the absorption transition at 2.07 eV observed on bare WS_2 (in Figure 4.3) corresponds to the X_A transition. To this end, I calculate the X_A energy taking into account the contact of WS_2 with hBN from the top and the bottom. To estimate the E_b of X_A, I solve the 2D Schrödinger equation with Hamiltonian from Eq. 1.12 taking the Keldysh-Rytova potential introduced in Chapter 1 as [101, 111, 115]:

$$V(\mathbf{r_{2D}}) = \frac{-e^2}{8\epsilon_0 r_0}\Big[H_0\Big(\frac{\kappa \mathbf{r_{2D}}}{r_0}\Big) - Y_0\Big(\frac{\kappa \mathbf{r_{2D}}}{r_0}\Big)\Big], \tag{4.1}$$

where H_0 (Y_0) denotes the Struve (Bessel) function, and e and ϵ_0 are the electron charge and dielectric constant of vacuum, respectively. The parameter κ is the mean value of dielectric constants of the materials in contact with the top and bottom TMD surface, and r_0 is the screening length (see Chapter 1). The calculations of E_b are conducted with the following parameters: $\kappa = 4.35$ [115], $r_0 = 3.4$ nm [115], and the exciton effective mass in monolayer WS_2 is taken as $m_{eff} = 0.175 m_0$ [115] (where m_0 is the electron rest mass). The obtained E_b of X_A in the hBN-encapsulated WS_2 is $\sim$ 179 meV, in agreement with the value of 180 meV found in the literature [115]. This E_b is over 200 meV lower than the reported E_b in monolayer WS_2 placed directly on SiO_2 ($E_b \sim 410$ meV) [113]. To calculate the energy of the X_A transition in the hBN-encapsulated WS_2, I estimate also the bandgap of monolayer WS_2 (E_g^{mono}). The calculations are performed according to the method from Ref. [108] based on

Ref. [239], where the bandgap of bulk WS_2 is considered as a reference system. The bandgap of monolayer WS_2 is estimated as:

$$E_g^{mono} = E_g^{bulk} + \frac{e^2}{\epsilon_{mono} d} \left\{ \frac{(L_{12} + L_{13})}{\sqrt{L_{12} L_{13}}} 2\tanh^{-1}(\sqrt{L_{12} L_{13}}) - \ln(1 - L_{12} L_{13}) \right\}, \tag{4.2}$$

where E_g^{bulk} is a bandgap of bulk TMD at K point of the Brillouin zone, ϵ_{mono} (d) is a dielectric constant (thickness) of monolayer TMD and $L_{1n} = \frac{\epsilon_{mono} - \epsilon_n}{\epsilon_{mono} + \epsilon_n}$ (where n = 2, 3, and ϵ_2 (ϵ_3) is a dielectric constant of material at the top (bottom) of monolayer TMD). In calculations of E_g^{mono} of the hBN-encapsulated monolayer WS_2, I use the parameters: ϵ_{mono} = 14 [240], E_g^{bulk} = 2.1 eV [44] and d = 0.612 nm [240].

The obtained E_g^{mono} is 2.225 eV which gives the energy of X_A of 2.046 eV. This value agrees well with the reported experimental X_A absorption energies in the hBN-encapsulated monolayer WS_2 which are in the range from around 2.05 eV to 2.06 eV [108, 115]. The discrepancy between the observed here ($\sim$ 2.07 eV) and reported values of X_A energy may be a result of a weak adhesion of WS_2 to the top and/or bottom hBN flakes. In such a case, the dielectric screening induced by the presence of hBN would be weaker than in fully encapsulated WS_2 (there would be a gap between WS_2 and hBN flake) which would result in a smaller energy shift. Importantly, the observed here X_A energy in the hBN-encapsulated WS_2 is around 30 meV lower than in WS_2 on SiO_2 [44, 241]. This shows a very strong impact of the dielectric screening on the excitonic transitions in monolayer TMDs. Based on the analysis presented above, I conclude that the observed absorption transition at 2.07 eV corresponds to X_A.

Going back to the first derivative RL spectrum in Figure 4.3, on bare WS_2 I do not observe a low-energy absorption transition of the charged exciton. This implies that the doping level in WS_2 in PEPI/WS_2 stack is low [44, 82, 123].

Now, I will discuss the RL in the HS region of PEPI/WS_2 stack. In the first derivative RL spectrum in Figure 4.3, I observe that the absorption transition of X_A in the HS region is redshifted with respect to X_A on bare WS_2 by around 10 meV. To investigate if the observed energy shift of X_A in the HS region is caused by the change of dielectric screening due to the presence of PEPI perovskite, I estimate the X_A energy using Eq. 4.1 and 4.2. In the calculations, I use the dielectric constant of PEPI estimated as the average of dielectric constants of inorganic slab (ϵ_w = 6.1 [242]) and PEA^+ organic spacer layer (ϵ_b = 3.32 [243, 244]) according to the following formula [242]:

$$\epsilon_{pero} = \frac{L_w \epsilon_w + L_b \epsilon_b}{L_w + L_b}, \tag{4.3}$$

where L_w and L_b is the thickness of the inorganic slab (taken as 0.636 nm [242]) and organic spacer layer (taken as 0.982 nm [242]), respectively. The obtained ϵ_{pero} of PEPI is 4.41 and

it is almost the same as the ϵ of hBN [242]. Therefore, the dielectric screening "felt" by excitons in WS_2 in the HS region should be roughly the same as on bare WS_2, and the X_A transition energies should be also similar. Using Eq. 4.1 and 4.2, I calculate the E_b and E_g^{mono} for monolayer WS_2 in contact with hBN from the top and PEPI from the bottom. The obtained values are 177 meV and 2.225 eV, respectively. The calculated energy of X_A in the HS region is then equal to 2.048 eV which is larger by only 2 meV than on bare WS_2. Thus, the dielectric environment of PEPI (considering its average dielectric constant) cannot explain the observed redshift of the X_A energy of around 10 meV. The origin of this shift could be explained by the weak adhesion between perovskite and WS_2 flakes but more accurate calculations are needed to better understand the impact of the dielectric screening induced by 2D perovskites on the excitons in monolayer TMDs.

4.2.3 Emission in WS_2

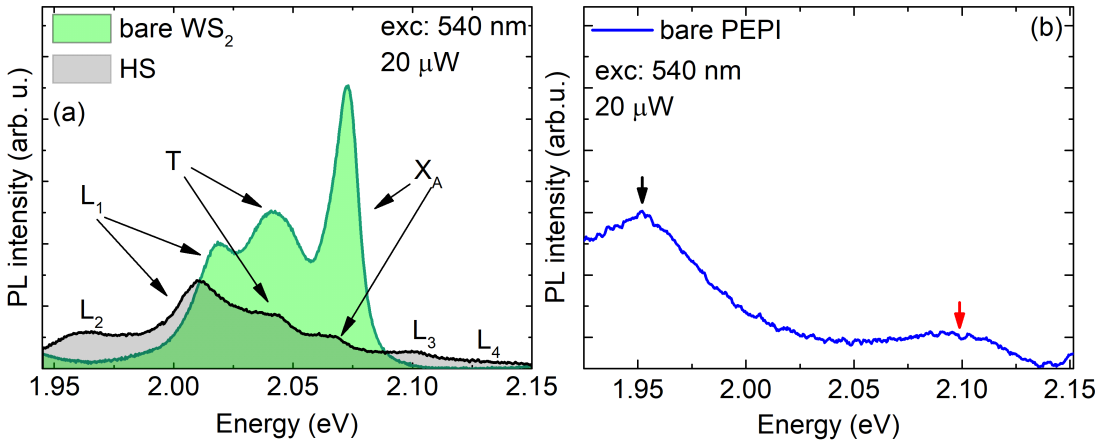

Figure 4.4: (a) - The PL spectra on bare WS_2 (green curve) and in the HS region (black curve). (b) - The PL spectrum on bare PEPI. Black and red arrows correspond to L_2 and L_3 peaks in the HS region.

The PL spectra on bare WS_2 and in the HS region are shown in Figure 4.4 (a). On bare WS_2, I observe three peaks - with the highest-energy peak having the largest emission intensity. To extract the positions and linewidths of the peaks, I fit the spectra with Gaussian functions. The peaks are located at: 2.015 eV, 2.043 eV and 2.073 eV. To gain an insight into the origin of these transitions, I compare the PL spectrum with the first derivative RL spectrum on bare WS_2 based on which I attribute the peak at 2.073 eV to X_A transition. In TMDs, the structural defects with low formation energy (such as sulfur vacancies in WS_2) naturally introduce an excess number of electrons to the material [116, 117, 245]. The excess carriers interact with excitons resulting in the charged excitonic (T) transitions. The emission peaks corresponding to T in monolayer TMDs are found $\sim$ 30 meV below the neutral exciton

energy [221, 246, 247]. Since the peak at 2.043 eV is redshifted with respect to X_A by 30 meV, I ascribe this peak to the charged exciton. Finally, the peak at 2.015 eV is observed below the X_A and T transitions and I tentatively attribute it to the defect-localized excitons L_1 [221, 246, 248].

The linewidths of the observed PL peaks are as follows: 19 meV (X_A), 28 meV (T) and 28 meV (L_1). These values are larger than in the hBN-encapsulated exfoliated monolayer TMDs by over 10 meV [221, 246, 249, 250]. The large FWHM can be explained by a level of disorder in the CVD-grown monolayer WS_2 which is usually higher than in the exfoliated monolayer TMD flakes [250]. The disorder (defects, strain, etc.) which is distributed randomly in the flake locally changes the bandgap of monolayer WS_2 leading to broader PL peaks [251, 252]. The other possible explanation for the large peak linewidths is the non-uniform adhesion of WS_2 and hBN flakes. This causes a non-uniform dielectric screening and subtle variations in the exciton binding energy and TMD bandgap. The much larger linewidth of T with respect to X_A peak (by 9 meV) can be explained by the fact that in monolayer WS_2 (and other TMDs with dark ground exciton state), the T peak has two contributions - from the intervalley spin singlet and intravalley spin triplet T transitions [221, 246, 249].

In the PL spectrum in the HS region in Figure 4.4 (a), six transitions can be distinguished. The peaks are observed at the following energies (obtained by fitting with Gaussian functions): 1.967 eV, 2.012 eV, 2.041 eV, 2.065 eV, 2.093 eV and 2.135 eV. To assign the peaks to their respective excitonic transitions, I compare the PL spectrum with the first derivative RL spectrum in the HS region, and with the PL spectrum on bare WS_2. The peak at 2.065 eV corresponds to the neutral exciton X_A. The peak at 2.041 eV is redshifted with respect to X_A by 24 meV and I attribute it to the charged exciton [221, 246, 247]. The emission at 2.012 eV is also observed on bare WS_2 and I can assign it to the defect-localized excitons in WS_2 (L_1). The low-energy peak located at 1.967 eV (I will refer to it as L_2) is also visible on bare PEPI (as shown by the black arrow in Figure 4.4 (b)). This suggests that the observed peak corresponds to the excitons localized at the defect states in PEPI. I will discuss further this hypothesis in Chapter 5. Finally, two high-energy peaks at 2.093 eV (L_3) and at 2.135 eV (L_4) are also observed in the PL spectrum on bare PEPI, as shown by the red arrow in Figure 4.4 (b). These transitions appear below the energy of neutral exciton in PEPI (which is $\sim$ 2.34 eV to 2.36 eV [166, 253–256]) and above the energy of T and X_A in WS_2. I will then tentatively ascribe the L_3 and L_4 peaks to the defect-localized excitons in PEPI. The FWHM of the identified in Figure 4.4 (a) peaks are comparable to the linewidths of their respective peaks on bare WS_2: 45 meV (L_2), 28 meV (L_1), 26 meV (T), 19 meV (X_A), 42 meV (L_3) and 28 meV (L_4).

4.2.4 Reflectivity and emission in PEPI

In Figure 4.5 (a), I present the first derivative RL spectra collected on bare PEPI and in the HS region. On bare perovskite, I observe the absorption transition at $\sim$ 2.34 eV. In the literature, the absorption transition at the energy range from 2.34 eV to 2.36 eV corresponds to the neutral exciton (I will refer to it as X_{PEPI}) [166, 253–256].

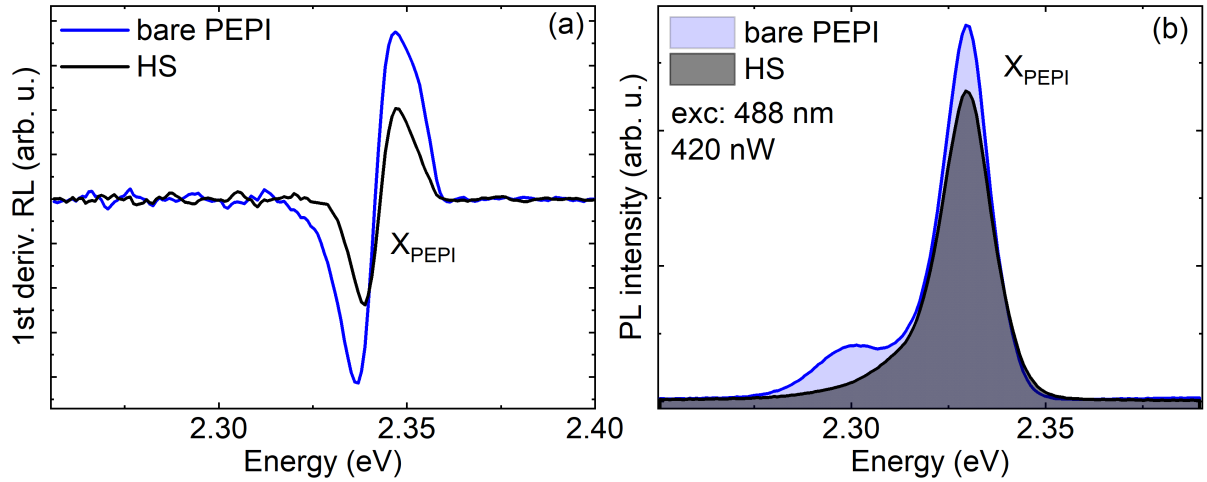

Figure 4.5: (a) - The first derivative RL spectra on bare PEPI (blue curve) and in the HS region (black curve). (b) - The PL spectra on bare PEPI (blue curve) and in the HS region (black curve).

The X_{PEPI} transition energy in the HS region is the same as on bare PEPI ($\sim$ 2.34 eV). It is important to note that in PEPI/WS_2 stack, the thickness of the PEPI flake is around 50 nm which corresponds to 29 perovskite layers [257]. As I discussed in Chapter 1, in 2D perovskites, the excitons (that are localized in the inorganic slabs) are subjected to the reduced dielectric screening induced by the spacer layers which strongly increases the E_b in these materials [140, 167, 168]. In thick 2D perovskites with thicknesses much larger than the single perovskite layer, most of the excitons are photoexcited far from the interface with the surrounding material. Therefore, the impact of the dielectric screening induced by the surrounding material on the optical transitions in 2D perovskites is negligible [140, 231, 258, 259]. The exceptions are ultrathin perovskite nanosheets with the thickness on the order of single perovskite layers [258–260]. For instance, the calculations of Zahra et al. [260] have shown that a thin sheet of $(C_6H_{13}NH_3)_2PbI_4$ perovskite on a silicon substrate exhibits around 100 meV larger exciton binding energy than its thick counterpart. Overall, no change of the absorption exciton energy on bare PEPI and in the HS region (observed in Figure 4.5 (a)) is a signature that PEPI is not sensitive to the dielectric screening induced by its surroundings.

The PL spectra collected on bare PEPI and in the HS region are shown in Figure 4.5 (b). On bare PEPI, I observe a strong high-energy peak with a weak peak on its low-energy side. To extract the positions of these peaks, I fit the spectra with the Lorentzian functions. The Lorentzian lineshape of the peaks implies a negligible inhomogeneous broadening and a low level of disorder in a material. On bare PEPI, the most intense peak is observed at 2.330 eV with a FWHM of 13 meV. I compare the PL and first derivative RL spectra based on which I ascribe the emission at 2.330 eV to the X_{PEPI} transition. The energy of X_{PEPI} peak agrees well with the previously reported studies [261–263], while its linewidth is around three times larger than was reported previously in the hBN-encapsulated PEPI at 5 K [231]. The second, much smaller PL peak is observed at $\sim$ 2.300 eV with a linewidth of 17 meV. The origin of this low-energy transition in PEPI is not yet fully understood. It was previously attributed to the phonon replica or defect-bound excitons [253, 264–266].

In the PL spectrum collected in the HS region, I observe a strong peak at 2.330 eV with a linewidth of 14 meV, and a long tail on its low-energy side. In an analogy to bare PEPI, I ascribe the main PL peak to the X_{PEPI} exciton transition [242, 254, 264, 265].

4.3 PEPI/$MoSe_2$

4.3.1 Optical microscopy

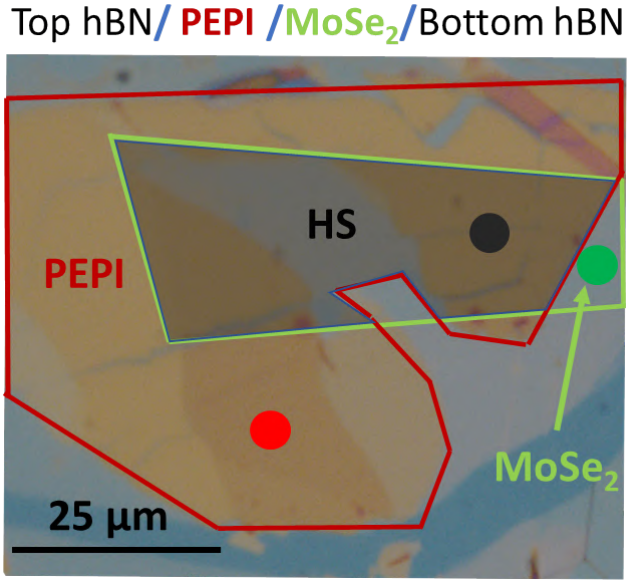

Figure 4.6: Optical microscope image of PEPI/$MoSe_2$ stack. The green and red broken lines surround the $MoSe_2$ and PEPI flakes, respectively. The HS region is indicated by the dark-shaded area. The black horizontal bar in the left bottom corner represents a distance of 25 µm. The red, green and black dots indicate the places on the sample, where the RL and PL spectra were collected.

In Figure 4.6, I present the optical microscope image of PEPI/$MoSe_2$ stack provided by Jonas Ziegler from the University of Regensburg. The perovskite and TMD flakes are enclosed by the red and green broken lines, respectively. The HS part of the sample is shown as the black-shaded area. The red, green and black dots roughly indicate the places of the RL and PL spectra collection on bare PEPI, bare $MoSe_2$ and the HS region, respectively.

The dimensions of each region of PEPI/$MoSe_2$ stack are as follows: $MoSe_2$ flake $\sim$ 50 µm x 20 µm, PEPI flake $\sim$ 70 µm x 40 µm and the HS region $\sim$ 50 µm x 20 µm. The whole stack is encapsulated by multilayer hBN flakes that can be partly distinguished by the blue color with lighter and darker areas (corresponding to thinner and thicker parts of the flake, respectively). The uniform optical contrast indicates that each constituent flake exhibits a mostly flat surface.

4.3.2 Reflectivity and emission in $MoSe_2$

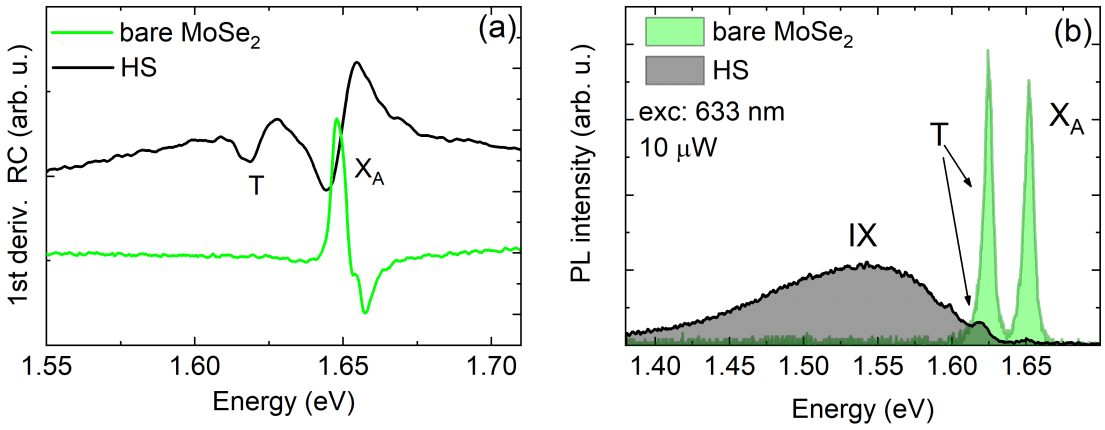

Figure 4.7: (a) - The first derivative RC spectra on bare $MoSe_2$ (green curve) and in the HS region (black curve). (b) - The PL spectra on bare $MoSe_2$ (green curve) and in the HS region (black curve).

To calculate the RC (according to Eq. 3.1) and first derivative of RC, I collect the RL spectra on the bare part of the $MoSe_2$ flake and in the HS region. The background RL spectrum is collected in the spot with top and bottom hBN. The transition energies are found in the inflection points of the first derivative RC spectra. In Figure 4.7 (a), I present the first derivative RC spectra on both parts of the sample. On bare $MoSe_2$, I observe the absorption transition at $\sim$ 1.65 eV. To check if the observed transition corresponds to X_A, I calculate the exciton binding energy and bandgap of monolayer $MoSe_2$ encapsulated in hBN. I solve the 2D Schrödinger equation with Keldysh-Rytova potential (from Eq. 4.1), taking $m_{eff} = 0.35m_0$ [115], $r_0 = 3.9$ nm [115] and $\kappa = 4.35$ [115]. To estimate the bandgap of monolayer

$MoSe_2$ according to Eq. 4.2, I use the following parameters: ϵ of monolayer $MoSe_2$ = 16.8 [240], monolayer thickness = 0.649 nm [240] and the bandgap of bulk $MoSe_2$ = 1.773 eV (calculated as the sum of the neutral exciton energy at K point at 5 K [125] and bulk exciton binding energy of 150 meV [267]. In the calculations, I obtain the E_b of 234 meV and E_g^{mono} of 1.890 eV which gives the energy of the X_A exciton transition in the hBN-encapsulated $MoSe_2$ of 1.656 eV. This value agrees well with the experimental observations and with the literature (where X_A is observed from around 1.64 eV to 1.66 eV) [115, 268–271]. Therefore, I attribute the observed at 1.65 eV absorption transition to the X_A.

In the HS region in Figure 4.7 (a), I observe two absorption transitions: at $\sim$ 1.62 eV and 1.65 eV. Based on the comparison of the first derivative RC spectra on bare $MoSe_2$ and in the HS region, I attribute the high-energy transition to X_A. The comparable X_A energy in both parts of the stack suggests that the dielectric screening induced by hBN and PEPI has a similar impact on the exciton binding energy and the bandgap of monolayer $MoSe_2$. To check the impact of the presence of PEPI and hBN on the X_A energy, I estimate the E_b and E_g^{mono} of $MoSe_2$ in the HS region according to Eq. 4.1 and 4.2, respectively. Taking the ϵ_{pero} of PEPI as 4.41 (see the subsection 4.2.2), I obtain the exciton binding energy of 233 meV and bandgap of 1.890 eV which are comparable to those in bare $MoSe_2$. Therefore, the energy of the X_A absorption transition almost does not change (1.656 eV on bare $MoSe_2$ vs. 1.657 eV in the HS region) which is observed in the experiment.

According to the literature, the low-energy transition at $\sim$ 1.62 eV corresponds to the charged exciton transition (T) [270, 272]. The reason for the appearance of this transition in the HS region will be discussed in Chapter 6.

In Figure 4.7 (b), I present the PL spectra collected on bare $MoSe_2$ and in the HS region. On bare $MoSe_2$, I observe two narrow peaks. To extract the transition energies and linewidths of the peaks, I fit the spectra with Lorentzian functions. Note that in the case of the CVD-grown WS_2 flake (subsection 4.2.3), the lineshape was Gaussian. The Lorentzian lineshape of the $MoSe_2$ peaks implies that the level of disorder in the exfoliated monolayer $MoSe_2$ flake is much lower than in the CVD-grown WS_2. The peaks are detected at: 1.619 eV and 1.646 eV. Based on the comparison of the PL and first derivative RC spectra, I attribute the high energy peak to the neutral exciton X_A transition. According to the literature, the emission energy of X_A in the hBN-encapsulated monolayer $MoSe_2$ is in the range from 1.64 eV to 1.66 eV which is comparable to the obtained experimental results [186, 270, 273–275]. Like monolayer WS_2, monolayer $MoSe_2$ is also an intrinsically n-doped material so I attribute the low-energy peak to the negatively charged exciton (T) [186, 270, 273, 274]. The binding energy of T can be defined as $E_b = E_{X_A} - E_T$ (where E_{X_A} and E_T is the energy of neutral and charged exciton, respectively) [120]. In Figure 4.7 (b)

on bare $MoSe_2$, the binding energy of T is 27 meV which is comparable to the previously reported values in the hBN-encapsulated $MoSe_2$ [273, 276, 277]. The linewidths of X_A and T peaks are 7 meV and 9 meV, respectively. This is several meV larger than reported linewidths of X_A and T peaks in the hBN-encapsulated $MoSe_2$ (which are on the order of 2 meV to 5 meV) [273, 277]. The absence of localized excitons below the energy of X_A and T peaks is an indication that in monolayer $MoSe_2$ the ground exciton state is optically bright [73]. The exciton recombination rate from the optically-allowed lowest state is much faster than the rate of carrier scattering to the defect states which explains the lack of low-energy defect-localized excitonic transition peaks in the PL spectrum.

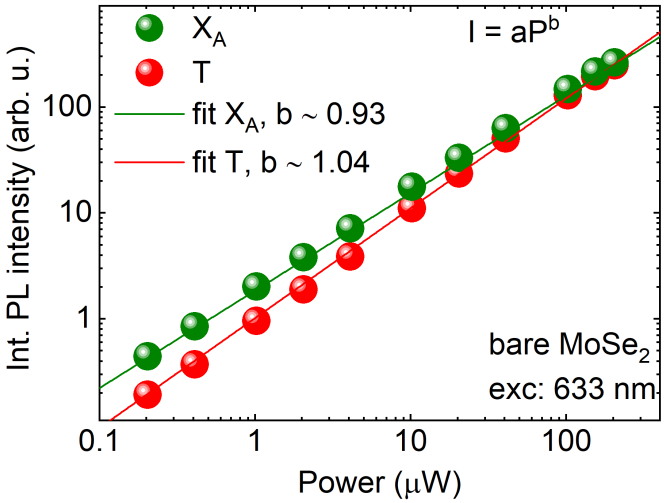

Figure 4.8: Power dependence of the integrated PL intensity of X_A (green spheres) and T (red spheres) on bare $MoSe_2$. The green (red) solid lines represent the fit of the PL intensity of the X_A (T) peak to the power law relation.

The additional piece of evidence confirming the assignment of the observed PL peaks on bare $MoSe_2$ to the excitonic transitions was obtained in the excitation power-dependent PL experiment. In Figure 4.8, I present the integrated PL intensity of X_A (green spheres) and T (red spheres) peaks on bare $MoSe_2$ as a function of the excitation power. The data were fitted to the power law function $I = aP^b$ (solid green and red lines), where I (P) stands for the PL intensity (excitation power), a is the coefficient and b is the parameter dependent on the type of electronic or excitonic transition [278]. The PL intensity of both X_A and T peaks exhibits an approximately linear dependence on the excitation power ($b = 0.93$ for X_A and 1.04 for T) which implies that X_A and T correspond to the excitonic transitions. The faster increase of the PL intensity of T with power compared to X_A (evidenced by a larger exponent b) can be ascribed to the photodoping effect [120, 279]. In this effect, the excitation photons photoionize carrier traps and increase the concentration of free carriers in a material. The ionization results in the increased density of charged excitons with respect to the neutral

excitons which is observed in the power-dependent PL experiment as a larger exponent b for T than for X_A.

In the PL spectrum in the HS region presented in Figure 4.7 (b), I observe three peaks. The PL intensity of two high-energy peaks, previously attributed to X_A and T transitions, is reduced by over 10 times. Interestingly, a new and very broad peak denoted as IX emerges on the low energy side of X_A and T. The position and linewidths of X_A and T peaks were obtained in the fitting procedure with Gaussian functions. The Gaussian spectral lineshape implies that the level of disorder is higher in the HS region than on bare $MoSe_2$ (where spectra were fitted with Lorentzian functions). This is usually observed in van der Waals stacks, where the non-homogeneous adhesion of the constituent flakes leads to the local variations of the dielectric screening [215]. The resulting local changes in the exciton energy are evidenced by the increase of the peak linewidths. In the HS region, the T and X_A peaks are observed at 1.620 eV with FWHM of 21 meV and 1.650 eV with FWHM of 26 meV, respectively. The assignment of the IX peak at $\sim$ 1.54 eV will be discussed in Chapter 6.

4.3.3 Reflectivity and emission in PEPI

The first derivative RC spectra on bare PEPI and in the HS region are shown in Figure 4.9 (a). In both parts of the sample, I observe the absorption transition at $\sim$ 2.35 eV which corresponds to the neutral exciton X_{PEPI} [166, 253–255]. As in the case of PEPI/WS_2 stack discussed in Section 4.2, the same exciton energy on bare PEPI and in the HS region suggests a similar impact of the dielectric screening induced by hBN and $MoSe_2$ on the E_b and bandgap of PEPI. The PL spectra on bare PEPI and in the HS region are presented

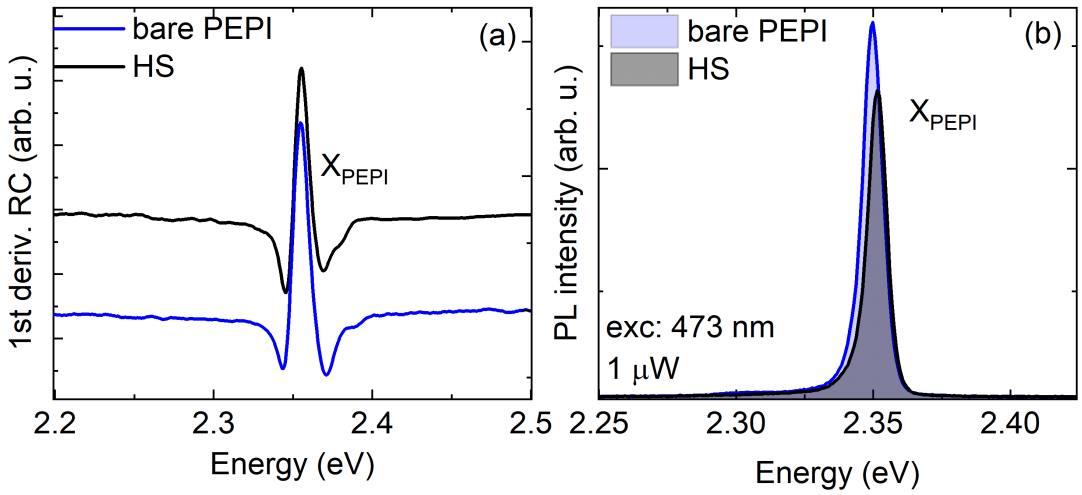

Figure 4.9: (a) - The first derivative RC spectra on bare PEPI (blue curve) and in the HS region (black curve). (b) - The PL spectra on bare PEPI (blue curve) and in the HS region (black curve).

in Figure 4.9 (b). On both parts of the stack, I observe a very intense peak with a weak sideband on its low-energy side. To obtain the positions of the peaks, I fit the spectra with Lorentzian functions. The main peak is observed at almost the same energy in both parts of the sample (2.350 eV on PEPI and 2.351 eV in the HS region). I attribute the high-energy peak in both parts of PEPI/$MoSe_2$ stack to X_{PEPI} transition [242, 265]. The X_{PEPI} peaks exhibit very similar linewidths - 9 meV on bare PEPI and 8 meV in the HS region which is comparable to the previously reported linewidths in the hBN-encapsulated PEPI [231]. On bare PEPI and in the HS region, a small, low-energy peak is observed at $\sim$ 2.300 eV. As was discussed in the previous Section, the origin of this transition in PEPI is not yet fully understood [265, 266, 280].

4.4 BAPI/$MoSe_2$

4.4.1 Optical microscopy

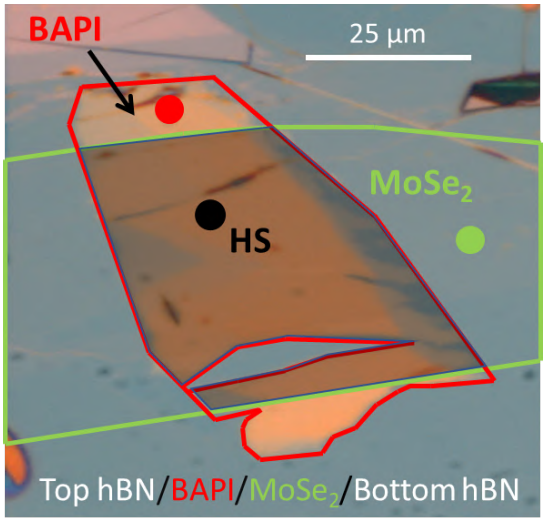

Figure 4.10: Optical microscope image of BAPI/$MoSe_2$ stack. The green and red broken lines encircle the $MoSe_2$ and BAPI flakes, respectively. The HS region is indicated as the dark-shaded area. The white horizontal bar in the top right corner of the image represents the distance of 25 µm. The red, green and black dots indicate the places on the sample, where the RL and PL spectra were collected.

The optical microscope image of BAPI/$MoSe_2$ was provided by Jonas Ziegler from the University of Regensburg. The image is presented in Figure 4.10. The BAPI flake is surrounded by red, and $MoSe_2$ - by green broken lines. The HS region of the sample is indicated by the black-shaded area. The whole structure is placed between the top and bottom multilayer hBN flakes, visible as a light blue background. The red, green and black

dots roughly indicate the places of the RL and PL spectra collection on bare BAPI, bare $MoSe_2$ and the HS region, respectively.

The estimated size of the $MoSe_2$ flake is $\sim$ 30 µm x 75 µm, BAPI flake is $\sim$ 25 µm x 60 µm, and the HS region is $\sim$ 25 µm x 50 µm. The BAPI and $MoSe_2$ flakes appear to be of good quality, exhibiting flat surfaces with little imperfections.

4.4.2 Reflectivity and emission in $MoSe_2$

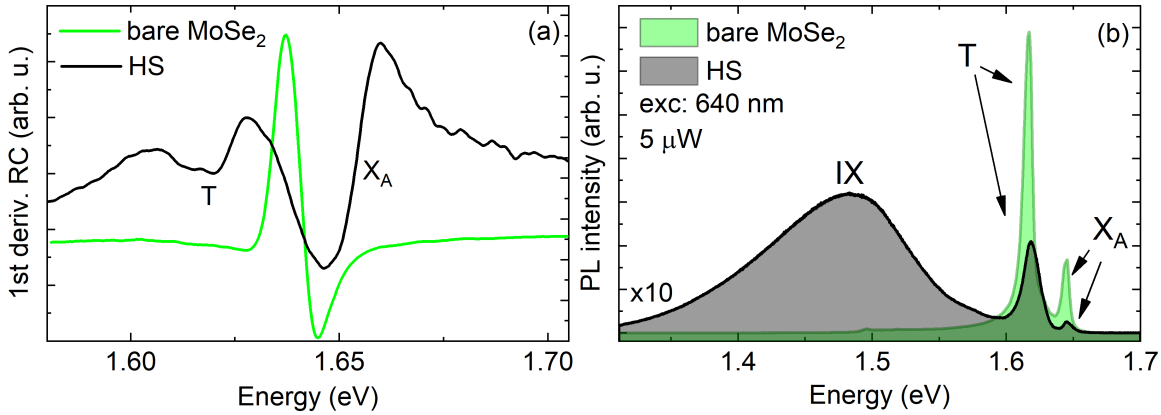

Figure 4.11: (a) - First derivative RC spectra on bare $MoSe_2$ (green curve) and in the HS region (black curve). (b) - The PL spectra on bare $MoSe_2$ (green curve) and in the HS region (black curve). The PL spectrum in the HS region was multiplied by 10 for clarity.

In Figure 4.11 (a), I present the first derivative RC spectra collected on bare $MoSe_2$ and in the HS region. On bare $MoSe_2$, I observe the absorption transition at $\sim$ 1.64 eV which corresponds to the exciton A (X_A) [115, 186, 269, 270].

In the HS region, two absorption transitions can be distinguished: at $\sim$ 1.62 eV and 1.65 eV [270, 272]. These transitions correspond to T and X_A, respectively. The reason for the appearance of the T transition in the HS region will be discussed in Chapter 6. To check if the observed difference of the X_A transition energy in both parts of BAPI/$MoSe_2$ stack (by around 10 meV) is caused by the dielectric screening induced by BAPI perovskite, I estimate the exciton binding energy and bandgap in $MoSe_2$ in contact with hBN and BAPI using Eq. 4.1 and 4.2. In the calculations, I use the average dielectric constant of the BAPI perovskite $\epsilon_{pero} = 4.92$, estimated according to Eq. 4.3 by taking the dielectric constant of the inorganic well ($\epsilon_w = 6.1$ [242]) and BA^+ organic spacer layer ($\epsilon_b = 4$ [243, 244]) [242]. The well L_w and barrier L_b thicknesses are taken as 0.56 nm [168]) and 0.71 nm [168]), respectively. The calculated E_b and E_g^{mono} in $MoSe_2$ adhering to hBN and BAPI are 221 meV and 1.884 eV, respectively, and the energy of X_A transition is 1.663 eV. Therefore, according to the calculations, the exciton energy in $MoSe_2$ in the HS region is blueshifted with respect

to the energy on bare $MoSe_2$ by 7 meV. This agrees well with the experimental results, where a shift of around 10 meV is observed.

The PL spectra on bare $MoSe_2$ and in the HS region are shown in Figure 4.11 (b). On bare $MoSe_2$, I observe two narrow peaks with the low-energy peak having approximately 4 times larger PL intensity than the high-energy one. To obtain the positions and FWHM of the observed peaks, I fit the spectra with Lorentzian functions. The peaks at 1.616 eV and 1.644 eV correspond to T and X_A transitions, respectively [186, 273, 274, 277]. The dissociation energy of T of 27 meV agrees well with the values found in the literature ($\sim$ 30 meV) [270, 274–277]. The X_A and T peaks exhibit linewidths of 6 meV and 8 meV, respectively which are comparable to the linewidths observed before in the hBN-encapsulated $MoSe_2$ [273, 277]. Interestingly, the T peak exhibits an asymmetric shape with a long tail at its low-energy side. This was previously attributed to the electron recoil effect [122, 123]. Due to the conservation of momentum, the recombination of T with a given center-of-mass momentum k, generates a photon and the momentum is then transferred to an electron. Consequently, the energy of the emitted photon ($\hbar\omega$) is lower than in the case of recombination of T with zero momentum ($\hbar\omega_0$): $\hbar\omega = \hbar\omega_0 - \frac{\hbar k^2}{2m_e^{*2}}\frac{M_{X_A}}{M_T}$, where m_e^* is the electron effective mass and M_{X_A} (M_T) is the effective mass of X_A (T). The resulting PL lineshape is a convolution of a symmetric lineshape and a low-energy exponential function which is observed in the experiment.

In Figure 4.11 (b) in the HS region, I observe three peaks: a very broad, low-energy peak denoted as IX and two weaker X_A and T peaks. Importantly, the PL intensity of X_A and T peaks is reduced by around 30 times compared to bare $MoSe_2$. To obtain the positions and linewidths of X_A and T peaks, I fit the spectra with Gaussian functions. The obtained T and X_A peak positions are 1.619 eV (with FWHM of 16 meV) and 1.646 eV (with FWHM of 16 meV), respectively. A discussion about the origin of the IX peak at $\sim$ 1.48 eV will be presented in Chapter 6.

4.4.3 Reflectivity and emission in BAPI

The first derivative RC spectra collected on bare BAPI and in the HS region are shown in Figure 4.12 (a). In both parts of the sample, I observe the absorption transition at $\sim$ 2.53 eV. According to the literature, the absorption at $\sim$ 2.53 eV corresponds to the neutral exciton transition (I will refer to it as X_{BAPI}) [168, 281]. Like in PEPI perovskite, the same absorption transition energy on bare BAPI and in the HS region suggests low sensitivity of the E_b and bandgap of BAPI to the dielectric screening induced by its environment.

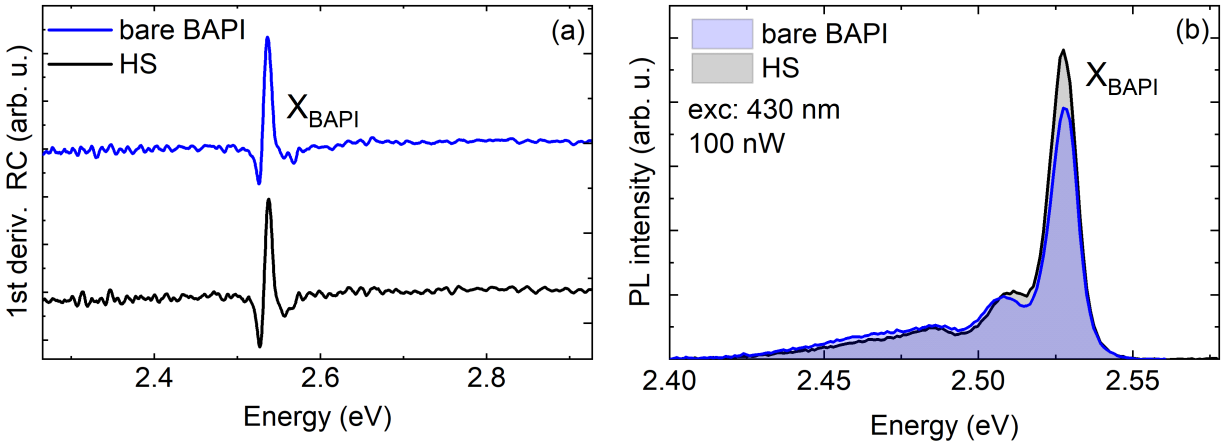

Figure 4.12: (a) - The first derivative RC spectra on bare BAPI (blue curve) and in the HS region (black curve). (b) - The PL spectra on bare BAPI (blue curve) and in the HS region (black curve).

The PL spectra on bare BAPI and in the HS region are presented in Figure 4.12 (b). In both parts of the sample, I observe three peaks - a strong high-energy peak and two weak, low-energy peaks. To obtain the peak positions, I fit the spectra with Lorentzian functions. On bare BAPI, the peaks are observed at: 2.528 eV with FWHM of 9 meV, 2.507 eV with FWHM of 15 meV, and 2.475 eV with FWHM of 41 meV. Based on the comparison of the PL and first derivative RC spectra, I attribute the highest energy emission to the neutral exciton X_{BAPI} [168, 281]. The linewidth of X_{BAPI} peak is comparable to the previously reported values at low temperature [168, 281]. The origin of two other peaks is still not fully understood and I will not focus on them further in this thesis.

In the HS region, the peaks are observed at the following energies: 2.527 eV (FWHM $\sim$ 9 meV), 2.509 eV (FWHM $\sim$ 13 meV), and 2.478 eV (FWHM $\sim$ 41 mev). As on bare BAPI, I attribute the highest energy peak to the exciton transition X_{BAPI}.

4.5 Conclusions

In this Chapter, I presented an analysis of the quality and optical properties of PEPI/WS_2, PEPI/$MoSe_2$ and BAPI/$MoSe_2$ van der Waals stacks. The characterization of each structure with an optical microscope has shown that the constituent flakes exhibit flat and homogeneous surfaces with a low level of contamination or macroscopic imperfections. The observed features in the RL and PL spectra were identified based on the literature. Understanding the origin of the excitonic transitions in the constituent materials will be the basis for an analysis of the mechanism of excitation transfer in the HS region in each stack.

Spectroscopic studies of excitation transfer in PEPI/WS_2 stack

In this Chapter, I will present a theoretical and experimental investigation of the optoelectronic properties of PEPI/WS_2 van der Waals stack. Based on this analysis, I will propose the mechanism of excitation transfer in 2D perovskite/TMD heterostructures.

5.1 Introduction

In Chapter 1, I pointed out that the research on 2D perovskite/TMD stacks is still in its infancy. In particular, the understanding of fundamental physics, crucial for device application, is far from complete. The limited number of studies that address the subject of excitation transfer in 2D perovskite/TMD stacks has given different results [32, 33, 282]. In 2020, Wang et al. [35] fabricated PEPI/monolayer WS_2 photodetector that exhibited better performance than the device based only on WS_2. The improvement of parameters, such as photocurrent and photoresponsivity, was attributed to the charge transfer (CT) from the photoexcited perovskite towards WS_2. On the other hand, based on the PL excitation (PLE) experiment, Zhang et al. [32] concluded that the nonradiative energy transfer (ET) takes place from perovskite to monolayer TMD in PEPI/WS_2 stack.

The understanding of the excitation transfer mechanism in 2D perovskite/TMD heterostructures is not yet conclusive and it is my motivation to shed more light on this important topic. Based on the spectroscopic experimental analysis of PEPI/WS_2 stack supported by theoretical calculations, I will show that 2D perovskite/TMD stacks exhibit a particular band structure that enables both charge and energy transfer to occur.

The contents of this Chapter were published in *Karpinska et al., ACS Appl. Mater. Interfaces 2021,* ***13****, 28, 33677-33684.*

5.2 Prediction of band alignment in PEPI/WS_2 stack

A theoretical investigation of the electronic structure in PEPI/WS_2 stack was conducted by the group from the Technical University of Dresden. The density functional theory (DFT) calculations of the band structure and the projected density of states (PDOS) were performed by Roman Kempt and Kati Finzel under the guidance of Agnieszka Kuc.

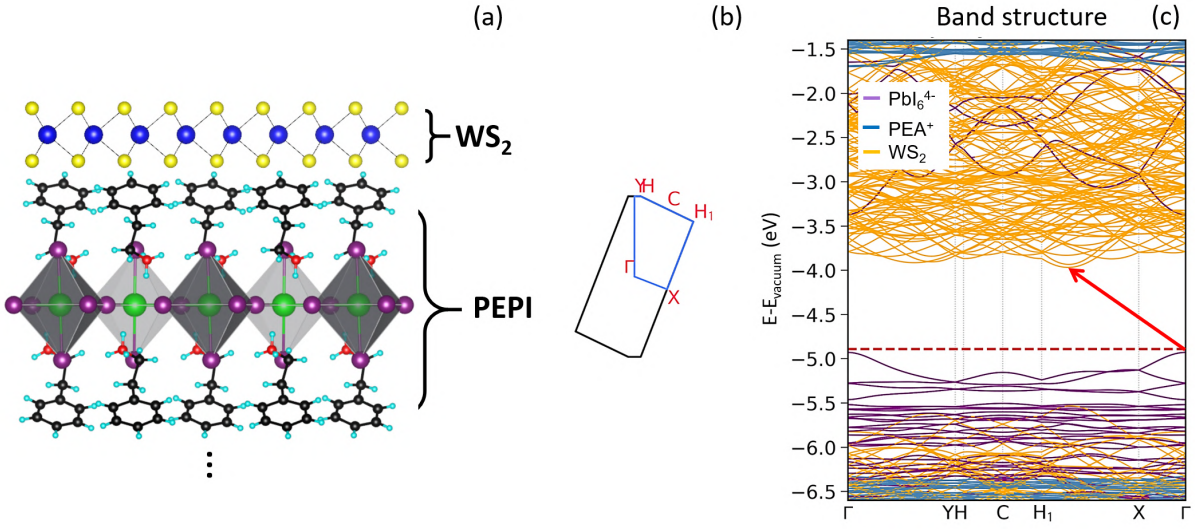

Figure 5.1: (a) - Schematic atomic structure of PEPI/WS_2 stack along the stacking axis. Blue, yellow, green, violet, red, black, and cyan spheres represent W, S, Pb, I, N, C, and H atoms, respectively. The inorganic PbI_6^{4-} slabs are marked by alternating dark and light grey octahedra. Black dots indicate multiple perovskite layers. Based on data from Ref. [154] and [283]. (b) - Brillouin zone in PEPI/WS_2 stack with high symmetry points shown in red. A broken blue line represents the k path. (c) - Electronic band structure in PEPI/WS_2 stack. The contributions of PbI_6^{4-}, PEA^+ and WS_2 orbitals are marked by a violet, blue and yellow color, respectively. The red dashed line indicates the Fermi level. The red arrow indicates the fundamental bandgap in the structure. The grey dotted lines are guides for the eye.

The atomic structure of PEPI/WS_2 stack along the stacking direction is schematically shown in Figure 5.1 (a). The structure was visualized in VESTA software [284] based on data from Ref.[154, 283]. Importantly, in the calculations, all three components - PbI_6^{4-} octahedra slabs, PEA^+ organic spacer layers and monolayer WS_2, were taken into account. The PEPI/WS_2 heterostructure consisted of 239 atoms.

The Brillouin zone in PEPI/WS_2 stack is presented in Figure 5.1 (b). The band structure and PDOS were calculated along the wavevector (k) path, shown as a blue broken line. The selected path included high symmetry points of the Brillouin zone and contained information about a whole energy landscape in the investigated structure.

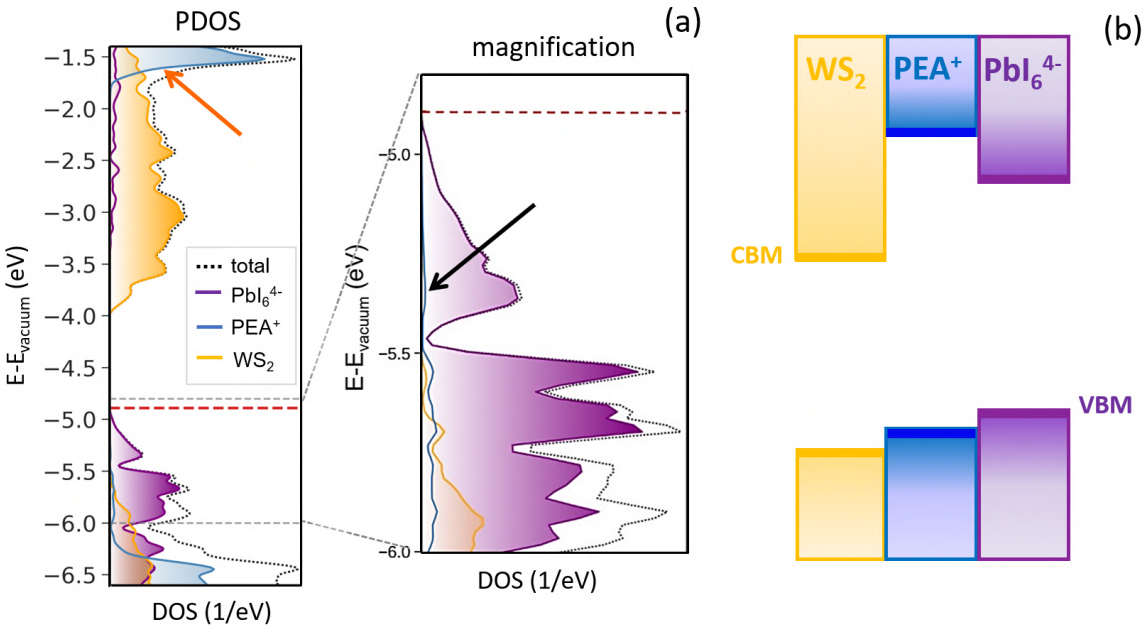

Figure 5.2: (a) - Left panel: The PDOS in PEPI/WS_2 stack. The dotted curve shows the total DOS. The contributions of PbI_6^{4-}, PEA^+ and WS_2 building blocks are shown in violet, blue and yellow colors, respectively. The grey dashed lines indicate the energy range of PDOS magnification. The red dashed line marks the Fermi level. The orange arrow indicates the PEA^+ states in the CB. Right panel: Magnification of a part of PDOS in the VB. The black arrow indicates the finite DOS introduced by PEA^+ orbitals between states of WS_2 and PbI_6^{4-}. (b) - Schematic diagram of the band alignment in PEPI/WS_2 stack. The color coding of the bands is the same as in (a).

The electronic band structure in PEPI/WS_2 stack is presented in Figure 5.1 (c). The violet, blue and yellow colors represent the bands with main contributions of PbI_6^{4-}, PEA^+ and WS_2 building blocks, respectively. The valence band maximum (VBM), located at Γ point, is mainly composed of perovskite PbI_6^{4-} orbitals. The conduction band minimum (CBM) which is in-between H_1 and X points - originates from WS_2 orbitals. Therefore, I can infer that PEPI/WS_2 stack exhibits type II band alignment with the momentum indirect bandgap (as shown by a red arrow).

The PbI_6^{4-}, PEA^+ and WS_2 band alignment can be deduced from the PDOS integrated over the entire k path. In Figure 5.2 (a), the PDOS and the magnification of its part in the VB are shown on the left and right panels, respectively. In the CB, the orbital contribution from WS_2 exhibits the lowest energy, followed by higher energy states of PbI_6^{4-} inorganic slab and even higher energy states of PEA^+ organic spacer (indicated by the orange arrow). Considering that PEA^+ is physically in-between PbI_6^{4-} and WS_2 layers, this implies that an energy barrier is introduced for electrons. In the VB, a finite density of PEA^+ states is located between the states of PbI_6^{4-} and WS_2, as shown by the black arrow in the right

panel in Figure 5.2 (a). Therefore, the orbital contributions of WS_2, PEA^+ and PbI_6^{4-} form a cascade of electronic states with PbI_6^{4-} states having the lowest, and WS_2 - the highest energy.

A simplified diagram of the band alignment concluded from the DFT calculations is presented in Figure 5.2 (b). The band colors correspond to the colors in PDOS. The horizontal lines represent the VBM and CBM states in each constituent layer. According to the DFT calculations, in the CB, the states of PEA^+ introduce a high energy barrier (of around 1 eV) for electrons. Since the distance from the center of WS_2 to the center of PbI_6^{4-} slab is large ($\sim$ 1.1 nm), I suspect that the electron transfer from PEPI to WS_2 is blocked [240, 257]. In the VB, the alignment of electronic states of WS_2, PEA^+ and PbI_6^{4-} layers forms a suitable environment for the transfer of holes from WS_2 to PEPI.

In the following Sections of this Chapter, I will show the experimental evidence of the CT and ET in PEPI/WS_2 stack.

5.3 The signatures of CT in PEPI/WS_2 stack

I will start with presenting the experimental evidence of the hole transfer from WS_2 to PEPI. To demonstrate that the CT occurs in PEPI/WS_2, I will compare the concentration of excess electrons in WS_2 on the bare part of the flake and the part that is in contact with PEPI. To this end, I will investigate the PL intensity of neutral and charged excitons in WS_2.

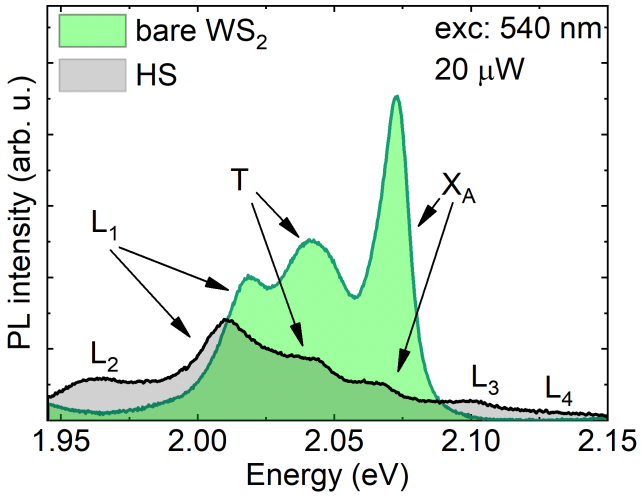

Figure 5.3: The PL spectra on bare WS_2 (green curve) and in the HS region (black curve).

In the PL experiment, PEPI/WS_2 stack was excited at λ_{exc} = 540 nm. The chosen excitation wavelength was below the energy of the PEPI bandgap in order to generate excitons only in WS_2 [166, 253–256]. The low probability of excitonic absorption in PEPI reduced

also the risk of perovskite degradation by laser-induced heating.

In Figure 5.3, I show two PL spectra collected on bare WS_2 and WS_2 in the HS region. On bare WS_2, I observe the emission of the localized (L_1), negatively charged (T) and neutral (X_A) excitons. On the HS, the peaks of the localized excitons in PEPI (L_2), L_1, T, X_A and another peaks of localized excitons in PEPI (L_3 and L_4), are resolved (see Chapter 4 for peak identification). Overall, the PL intensity of X_A and T in the HS region is lower than on bare WS_2. This is an initial indication of the excitation transfer from WS_2 to PEPI [28, 123, 185, 205]. Importantly, in the HS region, the integrated PL intensity of T is larger than that of X_A, whereas on bare WS_2, the PL intensities of T and X_A are similar. To estimate the PL intensity of X_A and T in both areas of PEPI/WS_2 stack, I fit the PL spectra with Gaussian functions. Then, I determine the change of the concentration of excess electrons in bare WS_2 and in the HS region by calculating the charged-to-neutral exciton PL intensity ratio T/X_A [7, 8, 120, 186]. For the spectra shown in Figure 5.3, on bare WS_2, the T/X_A ratio is $\sim$ 1.7, while on the HS the ratio is $\sim$ 3.4. Based on this observation, I conclude that the concentration of excess electrons in WS_2 is larger in the HS region than on bare WS_2.

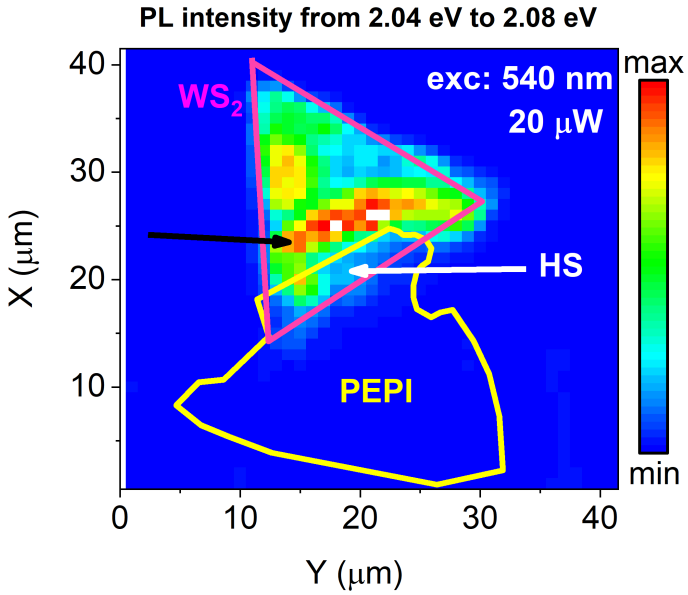

Figure 5.4: False color PL intensity map of PEPI/WS_2 stack in the energy range from 2.04 eV to 2.08 eV. The pink and yellow broken lines encircle WS_2 and PEPI flakes, respectively. The HS region is indicated by the white arrow. The black arrow indicates the region discussed at the end of this Section.

In order to draw more robust conclusions about the change of excess electron concentration in PEPI/WS_2 stack, I conduct the PL spatial mapping experiment. The excitation energy is the same as in the PL experiment described above. In Figure 5.4, I present the false color PL intensity map of PEPI/WS_2 stack, obtained by integration of the

PL spectra from 2.04 eV to 2.08 eV. This energy range mostly covered the neutral and charged exciton transitions in WS_2. In the map, I observe the overall reduction of PL intensity in the HS region compared to bare WS_2. This is consistent with the observation made in the analysis of two PL spectra presented above.

To investigate the change of the PL intensities of neutral and charged excitons in WS_2, the spectra on bare WS_2 and on the HS were extracted from the map. It is well known that the edge of a flake is usually a place of high concentration of structural defects [285–287]. Consequently, in the proximity of the flake edges the free-exciton emission may be largely obstructed by the defect-bound exciton peaks. To conduct the most reliable analysis, the PL spectra were selected at a distance of at least 1 µm from any edge. I have chosen 28 spectra on bare WS_2 and 10 spectra on the HS that fulfilled this criterion. The spectra were fitted with Gaussian functions in order to estimate the T/X_A PL intensity ratio in both parts of the sample.

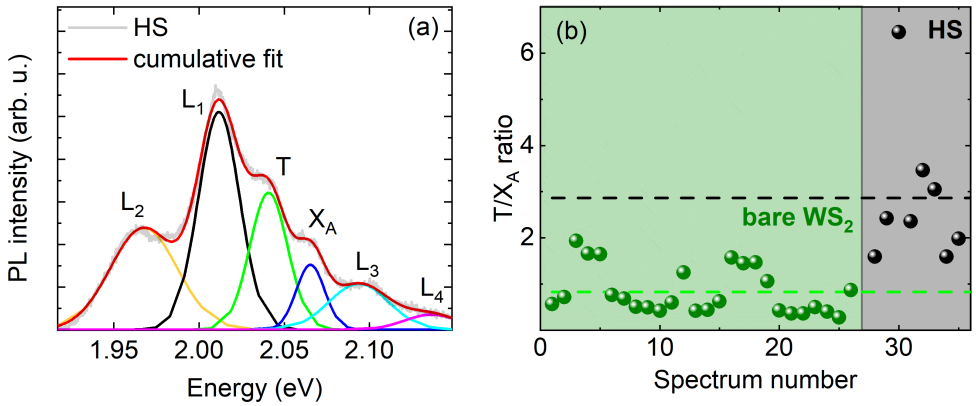

Figure 5.5: (a) - The PL spectrum collected in the HS region (grey curve) with fitted six Gaussian functions (yellow, black, green, blue, cyan and pink curves). The red curve represents the cumulative fit. (b) - The T/X_A emission intensity ratios (excluding the outliers) on bare WS_2 (green spheres) and on the HS (black spheres). The green and black dashed lines indicate the average T/X_A values on bare WS_2 and in the HS region, respectively.

An example of the fit is shown in Figure 5.5 (a), where the PL spectrum collected in the HS region (grey curve) was fitted with six Gaussian functions (yellow, black, green, blue, cyan and pink curves). The red curve indicates the cumulative fit, i.e. the sum of the constituent peaks.

The T/X_A values extracted from the analyzed spectra (after discarding the minimum and maximum values) are presented in Figure 5.5 (b). The average T/X_A ratios on bare WS_2 and in the HS region are indicated by the green and black dashed lines, respectively. On bare WS_2, the average ratio is 0.83 ± 0.50. In the HS region, the mean T/X_A is 2.9 ± 1.6. Therefore, the T/X_A ratio is larger in the HS region with respect to bare WS_2 by a factor

of 3. The large standard deviation of T/X_A values in the HS region is a signature of a high level of disorder which is often present at the contact area between the constituent layers in van der Waals stacks [215]. The above analysis is in agreement with the rough interpretation of two PL spectra shown in Figure 5.3. From the experimental results, I conclude that the concentration of excess electrons in WS_2 is increased in the HS region.

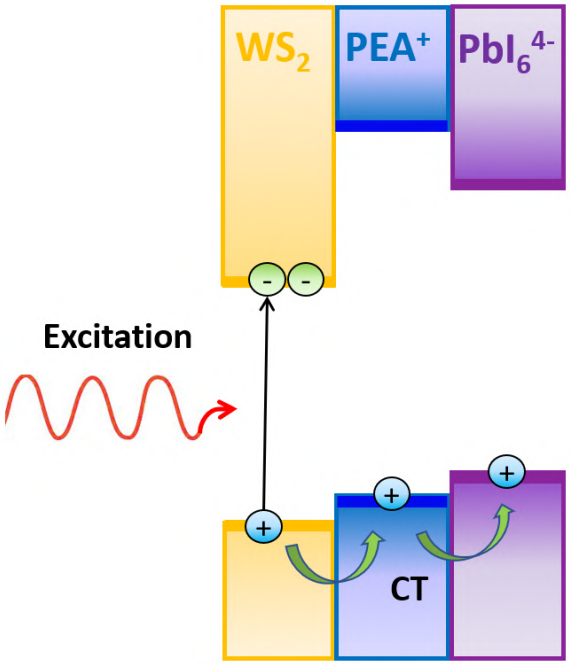

Figure 5.6: The proposed mechanism of CT in PEPI/WS_2 stack. The red wavy arrow denotes the excitation photon. The green curved arrows represent the transfer of holes (blue dots) from WS_2 to PEPI. The electrons are represented by green dots.

According to the band alignment presented in Figure 5.2 (b), the enhancement of excess electron concentration in WS_2 is a consequence of a transfer of photoexcited holes from WS_2 to PEPI. This process is schematically depicted by green curved arrows in Figure 5.6. The transfer of charge results in the dissociation of neutral and charged excitons which is evidenced by the reduced PL intensity of X_A and T peaks in the HS region. Additionally, the increased concentration of electrons leads to an increased T/X_A ratio in WS_2.

Let me now make a short comment about a particular region indicated by the black arrow in the PL intensity map in Figure 5.4. Namely, there is a PL intensity enhancement in the part of bare WS_2 that is close to the edge of the PEPI flake. In Figure 5.7 (a), I present the extracted from the map PL spectra that were collected at the center of bare WS_2 and WS_2 close to the PEPI edge. Importantly, the PL intensity of defect-localized exciton peak L_1 is over 2 times larger in WS_2 in the proximity of the PEPI edge than at the center of

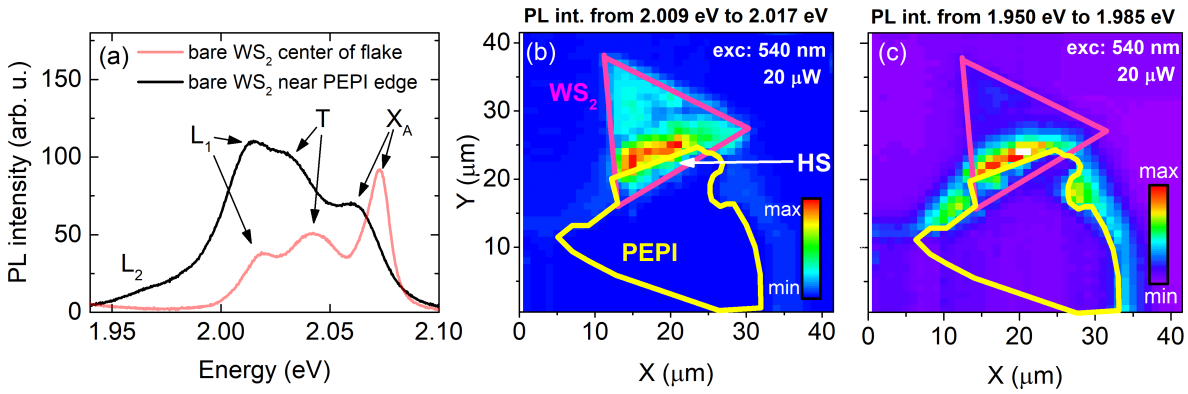

Figure 5.7: (a) - The PL spectra on bare WS_2 in the center of the flake (red curve) and close to the edge of PEPI (black curve). The PL intensity map obtained by integration of the PL spectra in the range (b) - from 2.009 eV to 2.017 eV and (c) - from 1.950 eV to 1.985 eV.

WS_2. In Figure 5.7 (b), I show the PL intensity map obtained by integration of L_1 peak from 2.009 eV to 2.017 eV. It is clear that the L_1 peak exhibits the largest PL intensity along the edge of PEPI and it is much weaker in other parts of WS_2. Additionally, in the PL spectrum, the T and X_A peaks exhibit an energy redshift (of $\sim$ 10 meV) with respect to peaks at the center of WS_2. The observed features (energy redshift of T and X_A, and the PL intensity enhancement of L_1 peak) could be related to the presence of tensile strain in WS_2 - I recall that in PEPI/WS_2 stack, the WS_2 flake is put on top of around 50-nm-thick PEPI flake. The strain could increase the concentration of structural defects at the interface PEPI-WS_2 which would result in an enhancement of the PL intensity of L_1 peak [248]. Another effect of the tensile strain in monolayer TMDs and their heterostructures is the redshift of energy bands [288–291]. The excitons photogenerated in a strained material drift towards lower energy states and recombine at lower energy which explains the observed redshift of T and X_A peaks. Wang et al. [292] reported that sufficiently large tensile strain (in monolayer WS_2 of $\sim$ 2.5 %) can modify the band structure and enable the formation of momentum-indirect excitons next to momentum-direct excitons. The authors have shown that under the strain of 2.5 %, the emission peak of momentum-indirect excitons is redshifted with respect to the X_A peak by around 40 meV. In the PL spectra, I observe a similar energy difference between the L_1 and X_A peaks ($\sim$ 45 meV) which implies the indirect exciton character of the L_1 peak. Note that L_1 peak is visible even far from the perovskite edge, where the strain should be minimal and the momentum-indirect excitons should not be formed. This suggests that more than one effect contributes to the PL intensity of L_1 peak, namely, the exciton localization at the structural defects and the additional recombination of momentum-indirect excitons.

Another feature observed in the PL spectrum of bare WS_2 close to the edge of PEPI is a low-energy tail denoted as L_2 in Figure 5.7 (a). Importantly, this tail is not present in

any other part of WS_2 flake but it is visible, albeit weakly, on bare PEPI flake (see Chapter 4). Since L_2 appears upon photoexcitation below the PEPI bandgap, I can assume that it originates from the localized states or defects in PEPI perovskite. In Figure 5.7 (c), I present the PL intensity map obtained by integration of L_2 in the energy range from 1.950 eV to 1.985 eV. I observe that the low-energy tail L_2 exhibits large PL intensity along the edge of PEPI and it is the largest when PEPI is in contact with the WS_2 flake. Zhang and collaborators [32] have suggested that in PEPI/WS_2 stack the states are formed at the interface PEA^+ organic spacer layer-WS_2 which was evidenced by the low-energy emission peak in the HS region. Therefore, the increased PL intensity of L_2 at the edge of PEPI in contact with WS_2 compared with bare PEPI and its edge may be explained by the increased number of localized states formed as a result of the coupling of PEA^+ with WS_2. Note that the presented above conclusions are just preliminary results. To gain a better insight into the origin of the observed emissions more studies are needed.

5.4 Energy transfer in PEPI/WS_2 stack

In this Section, based on the results of the PLE experiment, I will present the evidence for the ET in PEPI/WS_2 stack.

In Figure 5.8, I present the PLE spectra obtained on bare WS_2 and in the HS region. On bare WS_2, the PL intensity of neutral (X_A^{BARE}) and charged (T^{BARE}) excitons are shown as red full and empty squares, respectively. In the HS region, the PL intensity of neutral X_A^{HS} (charged T^{HS}) exciton is depicted as blue spheres (circles). The PL intensities were normalized at the low energy end of the excitation energy range at 2.32 eV. The normalization enabled a direct comparison of the PLE spectra on bare WS_2 and in the HS region.

First, I will focus on the analysis of the PLE spectra on bare WS_2. Starting from the low excitation energy and moving toward high energies, the PL intensities of X_A^{BARE} and T^{BARE} are initially reduced. This is a result of shifting of the excitation energy away from the absorbing excitonic states in WS_2 [204, 293]. When the excitation energy is increased from around 2.40 eV, I observe an enhancement of neutral and charged exciton PL intensity with the maximum at around 2.48 eV. According to the literature, the absorption energy at $\sim$ 2.46 eV in the hBN-encapsulated WS_2 corresponds to the exciton B (X_B) transition [294]. Hence, I can attribute the observed PLE peak to the excitation of X_A^{BARE} and T^{BARE} via the X_B state in WS_2. Note that the PL intensities of both X_A^{BARE} and T^{BARE} follow the same dependence implying that the excess electron concentration does not change with varying excitation energy.

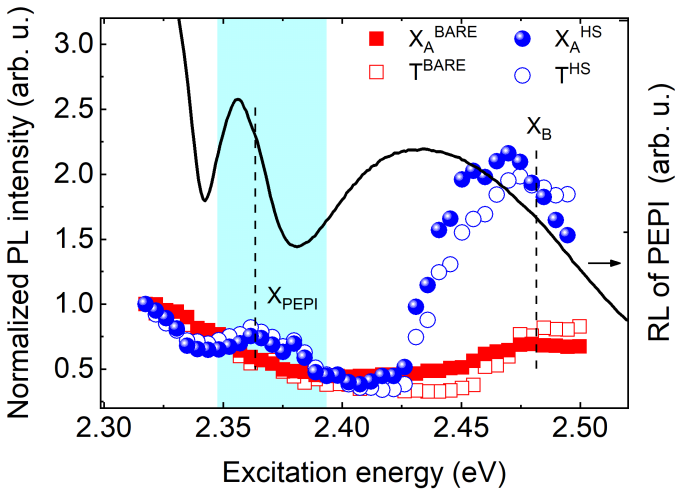

Figure 5.8: Normalized PLE spectra in PEPI/WS_2 stack. On bare WS_2, the integrated PL intensities of neutral (charged) excitons are shown as red full (empty) squares, and on the HS - as blue spheres (circles). The RL spectrum on bare PEPI is presented as a black curve. The cyan rectangle indicates the region, where the new PLE peak corresponding to X_{PEPI} is observed. The dashed vertical lines are guides for the eye.

Now, I will present the analysis of the PLE spectra obtained in the HS region. Overall, the shape of the PLE spectrum is similar to the spectrum of bare WS_2. The PL intensity of X_A^{HS} and T^{HS} initially decreases and above 2.42 eV starts increasing, reaching the resonance with X_B. Crucially, the important difference is the appearance of an additional, small peak at 2.36 eV (indicated by the cyan rectangle in Figure 5.8). This energy corresponds to the X_{PEPI} transition as evidenced by the RL spectrum shown as a black curve. I can interpret the observed PLE peak as a consequence of the excitation of X_A^{HS} and T^{HS} in WS_2 via PEPI. Importantly, the shapes of the PLE spectra of X_A^{HS} and T^{HS} are analogous which indicates a negligible change of excess electron concentration when WS_2 is excited via PEPI. Therefore, the peak at 2.36 eV can be interpreted as a fingerprint of ET from PEPI to WS_2. Note that an analogous argument was used by Kozawa et al. [204] as evidence for ET between $MoSe_2$ and WS_2. In the HS region, I observe also that the photoexcitation via X_B results in the PL enhancement of X_A^{HS} and T^{HS} by a factor of 3 compared to bare WS_2. This indicates another ET channel that couples the exciton B in WS_2 to a higher exciton state in PEPI.

In Figure 5.9, I present the schematic diagram of the pathways of ET in PEPI/WS_2 stack. In Chapter 4, I have shown that the absorption energy of X_A in the HS region is $\sim$ 2.07 eV. According to the calculations presented in Chapter 4, the binding energy of X_A in WS_2 in contact with hBN and PEPI is around 177 meV. Therefore, the bandgap in WS_2 in the HS region is $\sim$ 2.247 eV. In the PLE experiment, the enhancement of the PL intensity of charged and neutral exciton in the HS region corresponding to X_{PEPI}, is observed at

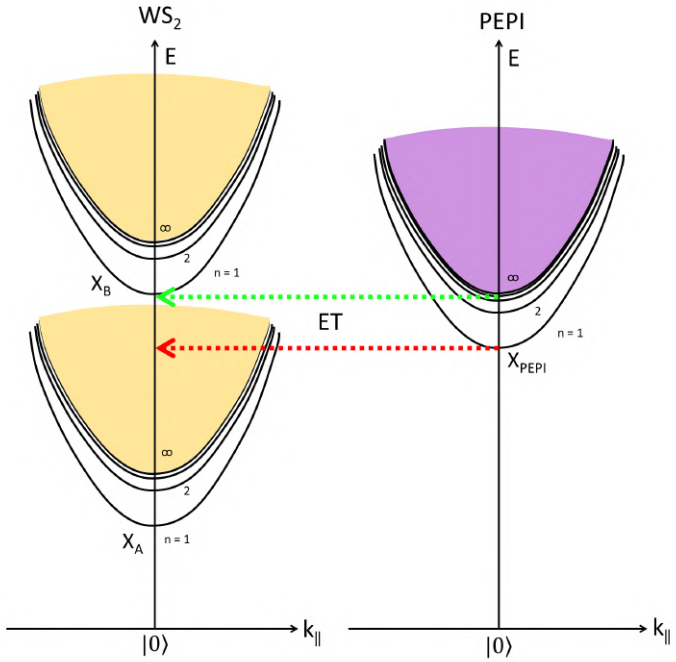

Figure 5.9: The suggested pathways of excitation transfer in PEPI/WS_2 stack. The dispersion relations of the ground ($n = 1$) and excited ($n = 2, 3...$) X_A, X_B and X_{PEPI} states, are schematically depicted as parabolas. The continuum (∞) of electronic states in PEPI and WS_2 is indicated by violet and yellow colors, respectively. The red and green dotted arrows represent the two possible pathways of ET from PEPI to WS_2. $|0\rangle$ is the ground state in WS_2 and PEPI. $k_{||}$ denotes the in-plane wavevector.

$\sim$ 2.36 eV. This implies that one of the pathways of ET in PEPI/WS_2 stack is from X_{PEPI} state to the continuum of states in WS_2, as shown by the red dotted arrow in Figure 5.9. The reported binding energy of X_{PEPI} is $\sim$ 274 meV and the bandgap of PEPI is $\sim$ 2.63 eV [295]. In the PLE experiment, the X_B state in WS_2 is observed at around 2.48 eV. Therefore, another pathway of ET in PEPI/WS_2 stack involves the transfer from one of the excited X_{PEPI} states to the X_B state in WS_2. This pathway is schematically depicted by the green dotted arrow in Figure 5.9.

I will now discuss the possible mechanism of ET in PEPI/WS_2 stack. As was discussed in Chapter 1, the ET can take place via a radiative or non-radiative pathway. The radiative ET involves the emission of a photon by an energy donor (D) and its absorption by an energy acceptor (A). The distance (d) between A and D on which this type of ET occurs has to be larger than the wavelength of the emitted by D (here PEPI) photon, i.e. $d > \frac{\lambda}{n}$, where n is the refractive index of D [206]. Taking n of PEPI as 2.1, this distance is $\sim$ 252 nm [242, 296]. In PEPI/WS_2 stack, the thickness of PEPI is $\sim$ 50 nm so the transfer of energy from PEPI to WS_2 via radiative mechanism is unlikely.

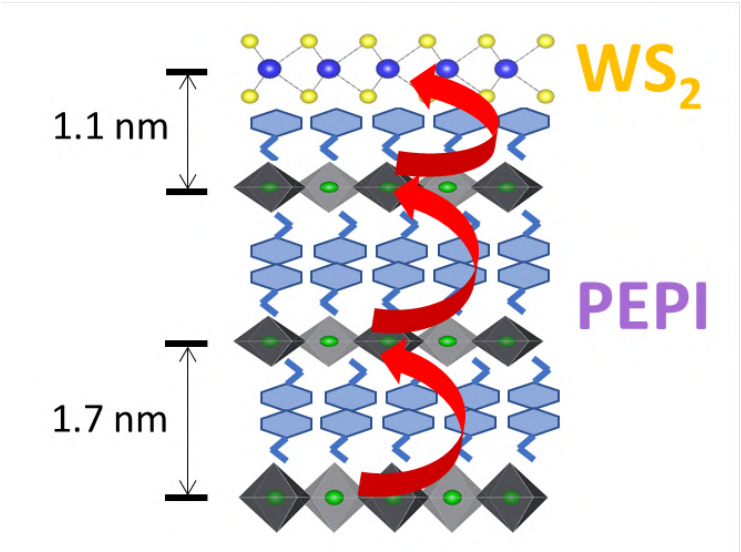

Figure 5.10: The schematic diagram showing the established mechanism of ET in PEPI/WS_2 stack. Red curved arrows represent the transfer between individual PbI_6^{4-} inorganic slabs, and between PbI_6^{4-} and WS_2. The given distances are calculated based on Ref. [257] and [240].

Apart from radiative ET, there are also two types of non-radiative ET mechanisms (see Chapter 1). In Dexter ET, the wavefunctions of D and A have to overlap to enable an exchange of carriers between the states in D and A [214]. Therefore, the spatial separation of D and A has to be lower than $\sim$ 1 nm [209]. In PEPI, the distance between the centers of the subsequent inorganic slabs separated by two layers of PEA^+ organic spacer is $\sim$ 1.7 nm, as shown in Figure 5.10. Considering that WS_2 adheres to one layer of PEA^+ organic spacer and that excitons are localized at the center of WS_2 flake and PbI_6^{4-} slab, the D-A separation is $\sim$ 1.1 nm. As the Dexter ET rate depends exponentially on the D-A distance (see Chapter 1), the efficiency of this process in PEPI/WS_2 stack should be low [29, 206]. Importantly, in Dexter ET both electron and hole are transferred from D to A which is facilitated by the type I band alignment [29, 206]. According to the DFT calculations discussed in Section 5.2, the band alignment in PEPI/WS_2 stack is of type II, where the transfer of holes from PEPI to WS_2 and transfer of electrons through the PEA^+ layer are energetically unfavorable. Based on this analysis, the ET via Dexter mechanism in PEPI/WS_2 stack is unlikely.

The non-radiative Förster resonant ET (FRET) takes place via dipole-dipole interactions, provided that the states in D and A are in resonance. In PEPI/WS_2, the requirement of energy resonance is fulfilled between the excitonic states in PEPI and free electron and hole states/exciton B state in WS_2. The typical distance on which the coupling between dipoles in D and A occurs is between $\sim$ 1 nm and $\sim$ 10 nm [209]. In PEPI/WS_2, this implies that the transfer to WS_2 is possible from up to the first six PbI_6^{4-} slabs. Importantly, in structures,

where the transition dipoles have 2D character (like in PEPI/WS_2) the rate of FRET is $\sim d^{-4}$ [211]. If I take into account the distance from the center of the first and second PbI_6^{4-} slab to the center of WS_2 as 1.1. nm and 2.8 nm, respectively, then the ET rate from the second slab would be reduced with respect to the rate from the first slab by a factor of ~ 42. This suggests that in PEPI/WS_2 stack the ET involves mostly the PbI_6^{4-} slab that is most adjacent to WS_2. Zhang et al. [32] have shown that in PEPI/WS_2 stack the ET first takes place between the individual perovskite layers before being transferred to WS_2. This process is schematically depicted by the red curved arrows in Figure 5.10. The contribution of multiple perovskite layers to the ET implies a larger PL intensity enhancement of WS_2 than if the transfer involved only a single inorganic slab.

To estimate the efficiency of the ET from PEPI to WS_2 observed in the PLE experiment, I consider the PL intensity of neutral exciton on bare WS_2 (I_{bare}) and in the HS region (I_{HS}) as [32]:

$$\begin{aligned} I_{bare} &= (1 - 10^{-A^{WS_2}}) I_0 QY^{bare} \\ I_{HS} &= (1 - 10^{-A^{WS_2}}) I_0 QY^{HS} + T^{WS_2}(1 - 10^{-A^{PEPI}})\beta_{in}\beta_{out} I_0 QY^{HS}, \end{aligned} \tag{5.1}$$

where A^{WS_2} (A^{PEPI}) and QY^{bare} (QY^{HS}) is the absorbance of WS_2 (PEPI) and the PL quantum yield of bare WS_2 (WS_2 in the HS region). The I_0 and T^{WS_2} denote the intensity of the incident light and the transmittance of WS_2, respectively. The β_{in} and β_{out} is the efficiency of ET between the individual perovskite layers in PEPI (assuming that the efficiency of each layer is the same) and the efficiency of ET from PEPI to WS_2, respectively. The effective PL enhancement of neutral exciton in WS_2 normalized by a quantum yield is then given by [32]:

$$\eta = \frac{I_{HS}/QY^{HS}}{I_{bare}/QY^{bare}} = \frac{(1 - 10^{-A^{WS_2}}) + T^{WS_2}(1 - 10^{-A^{PEPI}})\beta_{in}\beta_{out}}{(1 - 10^{-A^{WS_2}})} = 1 + \frac{T^{WS_2}(1 - 10^{-A^{PEPI}})\beta_{in}\beta_{out}}{(1 - 10^{-A^{WS_2}})}, \tag{5.2}$$

The factor η can be estimated from the normalized PLE spectra shown in Figure 5.8 by dividing the PLE intensity of X_A in the HS region by its intensity on bare WS_2 (at 2.36 eV $\eta \approx 1.35$). Assuming that β_{in} is 1, the lower limit of the efficiency of ET from PEPI to WS_2 can be calculated as:

$$\beta_{out} = \frac{\eta(1 - 10^{-A^{WS_2}}) - (1 - 10^{-A^{WS_2}})}{T^{WS_2}(1 - 10^{-A^{PEPI}})} = \frac{(1 - 10^{-A^{WS_2}})(\eta - 1)}{(1 - A^{WS_2} - R^{WS_2})(1 - 10^{-A^{PEPI}})}, \tag{5.3}$$

where R^{WS_2} is the reflectance of WS_2. I estimate the R^{WS_2} and A^{WS_2} taking the real and imaginary components of dielectric constant at $\lambda_{exc} = 488$ nm from Ref. [297]. The calculations of R^{WS_2} and A^{WS_2} are conducted based on Ref. [237], considering that WS_2 is in contact with semi-infinite hBN flake from one side and with semi-infinite PEPI flake from

the other side. The estimated reflectance and absorbance of WS_2 are $1.5*10^{-3}$ and 0.035, respectively. The absorbance of PEPI is taken as $A^{PEPI} = 0.12$ [137]. The obtained lower limit of the ET efficiency at 2.36 eV is ~ 12 % which is comparable to the efficiency estimated by Zhang et al. (~ 10 %) [32].

The presence of ET in PEPI/WS_2 could be also evidenced as the quenching of the PL intensity of X_{PEPI}. To check this possibility, I conduct the PL experiment. In Figure 5.11, I present the PL spectra collected on bare PEPI and in the HS region. Importantly, the PL intensity of X_{PEPI} is reduced by about 17 % on HS compared to bare PEPI.

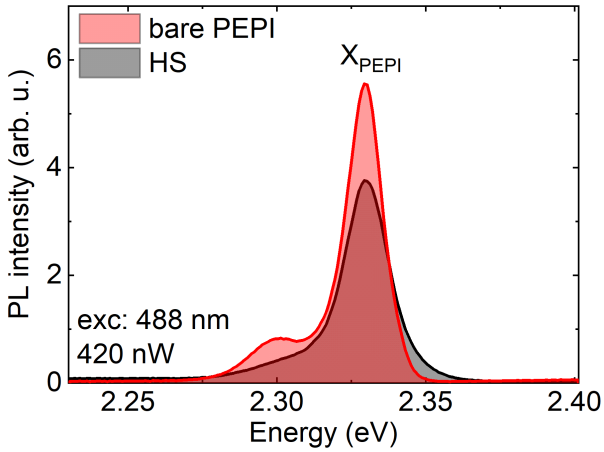

Figure 5.11: The PL spectra collected on bare PEPI (red curve) and in the HS region (black curve).

To draw more reliable conclusions about the changes in the PL intensity of X_{PEPI}, I conduct a PL spatial mapping experiment. In Figure 5.12 (a), I present a false color PL intensity map of PEPI/WS_2 stack. The map was obtained by integrating the X_{PEPI} peak from 2.325 eV to 2.340 eV. From the map, it is evident that the PL intensity in the HS region is lower than on bare PEPI. To assess the observed PL intensity difference, I analyze the distribution of the PL intensity of X_{PEPI}. In Figure 5.12 (b), I show the histogram of the PL intensity distribution on bare PEPI (orange bars) and in the HS region (green bars). The histogram intensities were normalized to the mean PL intensity on bare PEPI which allowed to enable a quick estimation of the HS/bare PEPI PL intensity ratio. On average, the PL intensity of X_{PEPI} is reduced on the HS by ~ 14 % compared to bare PEPI.

Since the PL intensity difference on bare PEPI and in the HS region is not large, it is important to first check if the absorption and reflection by WS_2 (which is on top of PEPI) are not the cause for the observed PL intensity reduction in the HS region. To this end,

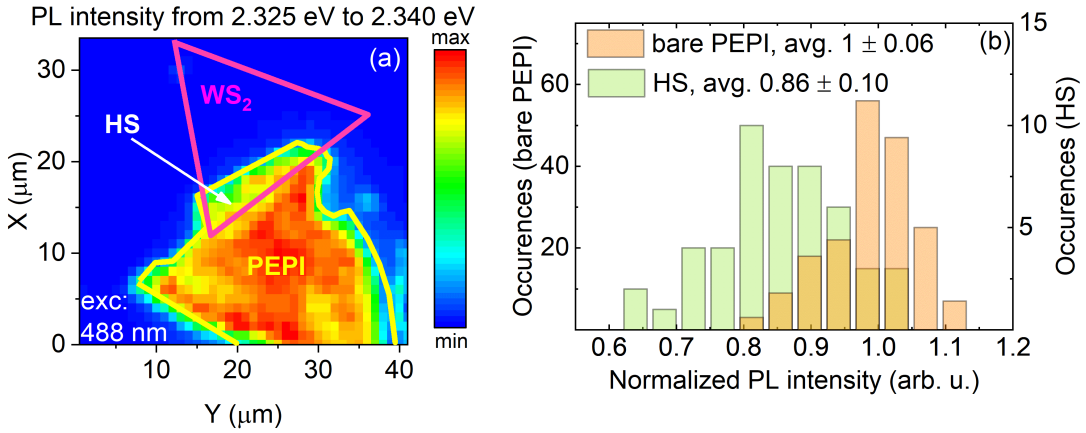

Figure 5.12: (a) - The false color PL intensity map of PEPI/WS_2 stack. The PL spectra were integrated from 2.325 eV to 2.340 eV. The perovskite flake is enclosed by the yellow and WS_2 flake - by the pink broken lines. The HS region is indicated by a white arrow. (b) - Histogram of X_{PEPI} emission intensity distribution on bare PEPI (orange bars) and in the HS region (green bars). The PL intensities were normalized to the average PL intensity on bare PEPI. The average PL intensity on bare PEPI and in the HS region is given in the form: mean value ± standard deviation.

I consider the PL intensity of X_{PEPI} on bare PEPI (I_{bare}) and in the HS region (I_{HS}) as:

$$\begin{aligned} I_{bare} &= (1 - 10^{-A^{PEPI}}) I_0 A^{PEPI} QY^{bare} \\ I_{HS} &= (1 - 10^{-A^{PEPI}}) I_0 (T^{WS_2} A^{PEPI} - A^{PEPI} \beta_{in} \beta_{out}) QY^{HS}, \end{aligned} \tag{5.4}$$

where QY^{bare} (QY^{HS}) is the PL quantum yield on bare PEPI (PEPI in the HS region). The HS/bare PEPI emission intensity ratio normalized by a quantum yield is given by:

$$\frac{I_{HS}/QY^{HS}}{I_{bare}/QY^{bare}} = T^{WS_2}(1 - \beta_{in}\beta_{out}) = (1 - A^{WS_2} - R^{WS_2})(1 - \beta_{in}\beta_{out}). \tag{5.5}$$

Neglecting the ET and taking the previously calculated parameters R^{WS_2} and A^{WS_2}, the PL intensity ratio is ~ 0.96. In the PL experiment, I observe the average ratio of ~ 0.86 as presented in the histogram in Figure 5.12 (b). Therefore, the decrease of the average PL intensity can be only partially attributed to the reduction of the effective excitation power that reaches PEPI due to the absorption and reflection in WS_2. The large impact of the ET on the PL intensity of X_{PEPI} is surprising since there is no actual excitonic state in WS_2 that is in resonance with the ground X_{PEPI} state. In this case, the absorption dipole moment for the acceptor (WS_2) is small which should lead to weak dipole-dipole interactions and weak ET. In consideration of the X_{PEPI} PL intensity, it is important to take into account that the HS region is highly disordered. This is evidenced by a larger standard deviation in the HS region (almost by a factor of 2) compared to bare PEPI, as shown in Figure 5.12 (b). Therefore, the effect of the ET on the PL intensity of X_{PEPI} in the HS region can be hidden in the broad distribution observed in the histogram.

Based on the ET efficiency obtained in the PLE experiment (β_{out}), I can also estimate the expected X_{PEPI} PL intensity decrease in the HS region. Considering that the efficiency of ET from PEPI to WS_2 is $\beta_{out} = 12$ % and taking β_{in} as 1, I obtain the intensity reduction of ~ 15 %. This is comparable to the average X_{PEPI} PL intensity reduction observed in the PL spatial mapping experiment.

5.5 Conclusions

In this Chapter, I presented the results of the studies of the excitation transfer between WS_2 and PEPI in PEPI/WS_2 van der Waals stack. The DFT calculations have predicted a band alignment that allows a transfer of holes from WS_2 to PEPI, whereas a transfer of electrons from PEPI to WS_2 is blocked.

In the PL experiment, I observed that the PL intensity ratio of the charged exciton to neutral exciton in WS_2 is increased in the HS region compared to bare WS_2. This observation implies that the concentration of excess electrons in WS_2 is increased which is in line with the theoretical predictions of the hole transfer from WS_2 to PEPI.

The analysis of the charged and neutral exciton PL intensity in WS_2 in the PLE experiment has indicated that there is also an excitonic ET from PEPI to WS_2. The ET process involves a transfer from the ground (excited) exciton state in PEPI to the continuum of free carrier states (X_B) state in WS_2.

Previous reports have shown that in TMD/TMD stacks the electronic coupling between the constituent materials enables the excitation transfer either through charge or energy transfer [8, 29, 195, 204]. In this Chapter, I have shown that a particular band alignment in 2D perovskite/TMD heterostructures enables the excitation transfer via both mechanisms. The important advantage of this type of structures is the possibility to easily manipulate the transfer mechanism. In the next Chapter, I will show that in 2D perovskite/TMD stacks the transfer mechanism can be engineered by the proper selection of the organic spacer compound.

Spectroscopic studies of excitation transfer in PEPI/$MoSe_2$ and BAPI/$MoSe_2$ stacks

In this Chapter, I present an investigation of the optical properties in PEPI/$MoSe_2$ and BAPI/$MoSe_2$ van der Waals stacks. The experimental results are confronted with theoretical predictions based on which I suggest the mechanism of excitation transfer and discuss the possibility of its manipulation in 2D perovskite/TMD heterostructures.

6.1 Introduction

An understanding of the physical properties of a single material or the heterostructure is crucial for future applications in devices. In Chapter 5, I discussed that the consensus about the dominating mechanism of excitation transfer in 2D perovskite/TMD stacks has not yet been reached. Another important aspect - the possibility to control this mechanism, is also mostly unexplored in this type of structures.

In this Chapter, I will investigate these issues in PEPI/$MoSe_2$ and BAPI/$MoSe_2$ stacks. Importantly, the employed 2D perovskites, PEPI and BAPI, consist of the same PbI_6^{4-} octahedra slabs and differ only by the organic spacer compound. Using various optical spectroscopic methods and comparing the experimental results with the theoretical predictions of band structure, I will show that in 2D perovskite/TMD stacks, the VB alignment facilitates the transfer of holes from perovskite to TMD leading to the formation of interlayer excitons (IXs). This CT can be accompanied by the excitonic ET, provided that the condition of resonance of the exciton states in 2D perovskite and TMD constituents is fulfilled. I will demonstrate that fabricating stacks composed of 2D perovskites with the same inorganic framework but different organic spacers enables turning on or off the excitation transfer process via the ET mechanism.

The results presented in this Chapter were published in *Karpinska et al., Nanoscale, 2022, **14**, 8085-8095.*

6.2 Band alignment in PEPI/$MoSe_2$ and BAPI/$MoSe_2$ stacks

Let me first introduce the results of the DFT calculations and propose the band alignment in PEPI/$MoSe_2$ and BAPI/$MoSe_2$ stacks. The presented band structure and PDOS were calculated by Roman Kempt under the guidance of Agnieszka Kuc at the Technical University of Dresden.

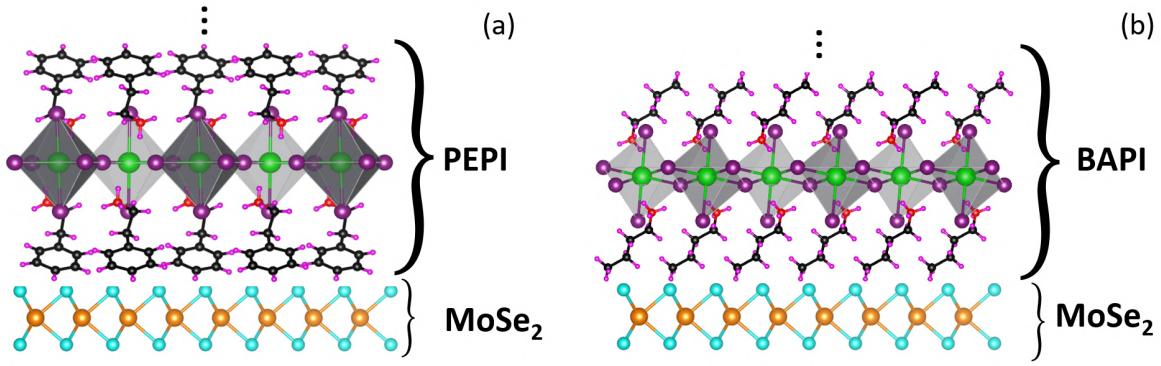

Figure 6.1: The schematic atomic structures of (a) - PEPI/$MoSe_2$ and (b) - BAPI/$MoSe_2$ stacks along the stacking axis. The colors represent the following atoms: Mo (orange), Se (cyan), Pb (green), I (violet), N (red), C (black) and H (pink). Black dots indicate multiple perovskite layers. Based on Ref. [154, 155, 298]

In Figure 6.1, I present the schematic atomic structures of (a) - PEPI/$MoSe_2$ and (b) - BAPI/$MoSe_2$ stacks visualized in VESTA software [284] based on Ref. [154, 155, 298]. In the calculations, the orbitals of all the layers, i.e. PEA^+ or BA^+, PbI_6^{4-} and $MoSe_2$, were taken into account. The PEPI/$MoSe_2$ and BAPI/$MoSe_2$ heterostructures consisted of 345 and 207 atoms, respectively.

The DFT calculations were conducted along the k path shown in Figure 6.2 (a). The band structures in PEPI/$MoSe_2$ and BAPI/$MoSe_2$ stacks are presented in Figure 6.2 (b) and (c), respectively. The colors of the bands indicate the largest orbital contribution of the following constituents: PEA^+ (red), BA^+ (orange), PbI_6^{4-} (green) and $MoSe_2$ (blue). In both structures, the VBM is located in the inorganic PbI_6^{4-} octahedra slab at high symmetry Γ point of the Brillouin zone. Interestingly, while the CBM in both stacks is in monolayer $MoSe_2$, it is located at different points of the Brillouin zone - in PEPI/$MoSe_2$ stack, the CBM

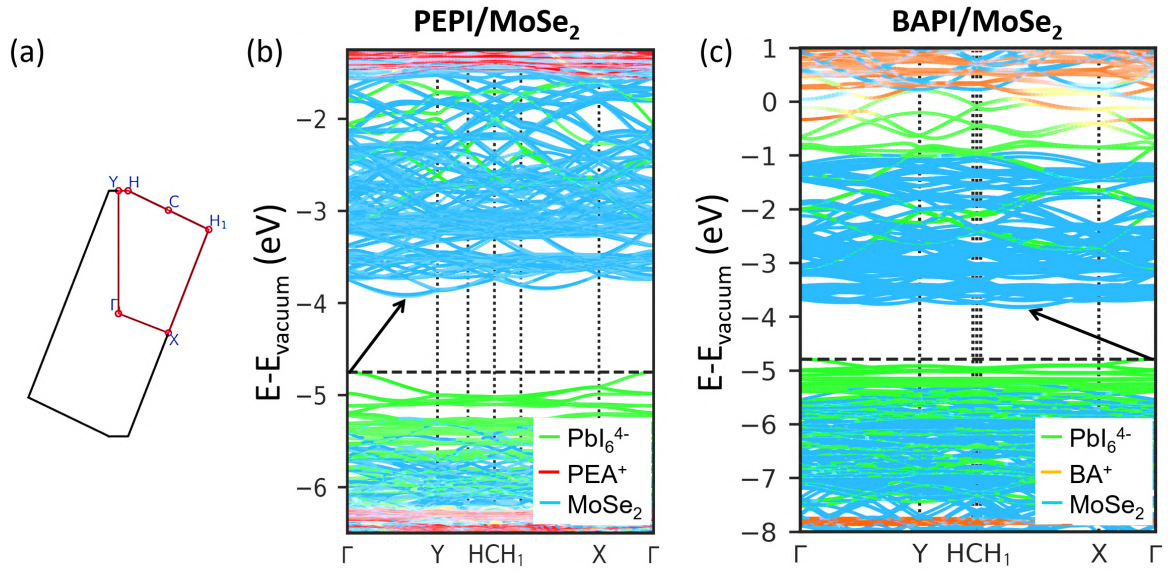

Figure 6.2: (a) - The Brillouin zone with high symmetry points in PEPI/$MoSe_2$ and BAPI/$MoSe_2$ stacks. The red broken line indicates the k path along which the calculations were performed. The band structure in (b) - PEPI/$MoSe_2$ and (c) - BAPI/$MoSe_2$ stack. Red, orange, green and blue curves indicate the contributions of the orbitals of PEA^+, BA^+, PbI_6^{4-} and $MoSe_2$ components, respectively. The black arrows indicate the fundamental bandgap in each structure.

is at a low symmetry point in-between Γ and Y points, and in BAPI/$MoSe_2$ stack, the CBM is at a low symmetry point between the H_1 and X points. In Chapter 1, I discussed that the size of the perovskite bandgap is strongly influenced by the organic spacer compound. Despite being composed of the same inorganic octahedra slabs, the bandgap of PEPI and BAPI differ by over 400 meV - in PEPI the bandgap is around 2.61 eV, while in BAPI around 3.02 eV [166, 168]. The analysis of the band structures presented above has revealed that the organic spacer compound not only impacts the electronic properties of the 2D perovskite but of the whole 2D perovskite/TMD stack. I will take advantage of this fact when studying the differences in the excitation transfer mechanism in PEPI/$MoSe_2$ and BAPI/$MoSe_2$ stacks in the subsequent parts of this Chapter.

To conclude the band structure analysis, both PEPI/$MoSe_2$ and BAPI/$MoSe_2$ stacks exhibit type II band alignment, where the fundamental bandgap is momentum indirect, as presented by the black arrows in Figure 6.2 (b) and (c).

The contribution of the constituent layers to the band structure is more clearly visible in the PDOS in Figure 6.3. The qualitative results observed for (a) - PEPI/$MoSe_2$ and (b) - BAPI/$MoSe_2$ stacks were similar. In the VB, the states of PbI_6^{4-} exhibit the lowest, and of $MoSe_2$ - the highest energy. Interestingly, a small density of PEA^+ or BA^+ states can be discerned in the VB between the states of $MoSe_2$ and PbI_6^{4-} layers,

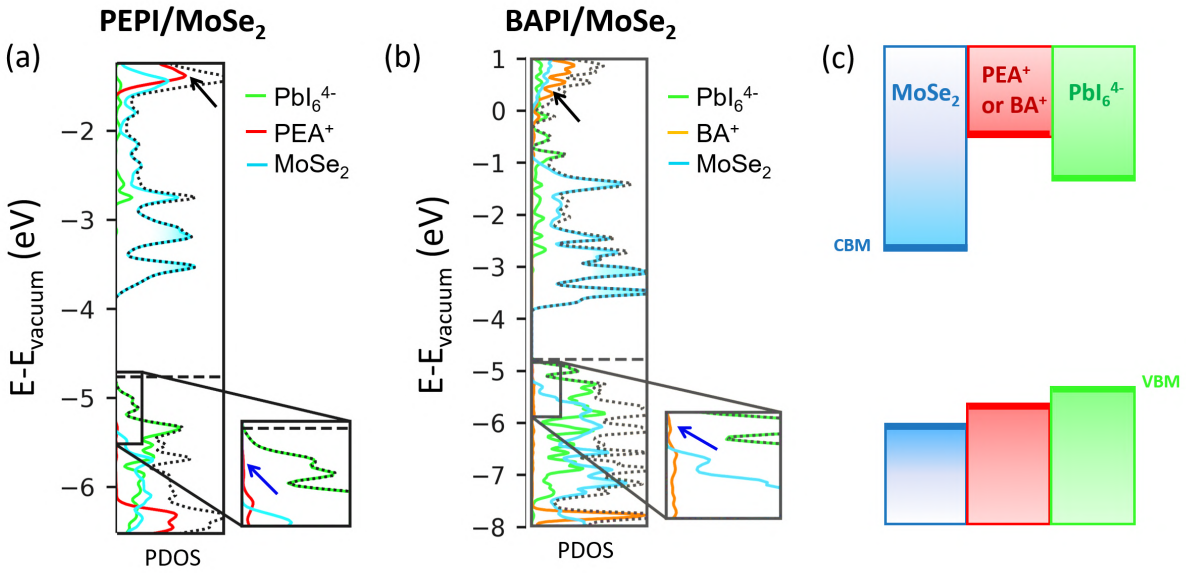

Figure 6.3: The PDOS with specified contributions of each of the building blocks in (a) - PEPI/$MoSe_2$ and (b) - BAPI/$MoSe_2$ stacks. The insets show the magnification of the part of PDOS in the VB. Red, orange, green and blue colors indicate the orbital contributions of PEA^+, BA^+, PbI_6^{4-} and $MoSe_2$, respectively. Dotted curves represent the total density of states. Blue arrows indicate the density of states of PEA^+ or BA^+ in-between states of $MoSe_2$ and PbI_6^{4-} in the VB. Black arrows indicate the PEA^+ or BA^+ states in the CB. (c) - Schematic diagram of the band alignment in PEPI/$MoSe_2$ and BAPI/$MoSe_2$ stacks. The color coding of the bands is the same as in (a).

as indicated by the blue arrows in the inset of Figure 6.3 (a) and (b). In the CB, the states introduced by $MoSe_2$ have the lowest energy, followed by states of PbI_6^{4-} and PEA^+ or BA^+ (indicated by black arrows). Based on these results, I can deduce the band alignment in PEPI/$MoSe_2$ and BAPI/$MoSe_2$ stacks which is shown schematically in Figure 6.3 (c). The band colors correspond to the colors in PDOS and the horizontal lines represent the VBM and CBM states in each constituent layer. In both structures in the VB, the electronic states introduced by each building block are aligned in a cascade-like manner with the lowest-energy states located in PbI_6^{4-}. Therefore, this band alignment should favor the transfer of holes from $MoSe_2$ to PEPI or BAPI perovskite layer. In the CB, the high energy states are introduced by organic spacer orbitals between the states of $MoSe_2$ and PbI_6^{4-}. As a result, the energy barrier for electrons of $\sim$ 1 eV and 3 eV is formed in PEPI/$MoSe_2$ and BAPI/$MoSe_2$ stack, respectively. This suggests that the transfer of electrons from PbI_6^{4-} slab to $MoSe_2$ layer is unlikely.

In the next part of this Chapter, I will show that in both PEPI/$MoSe_2$ and BAPI/$MoSe_2$ stacks the transfer of holes leads to the formation of IXs.

6.3 Signatures of CT and formation of IXs in PEPI/$MoSe_2$ and BAPI/$MoSe_2$ stacks

I will start with a discussion of the results of the steady-state optical spectroscopy experiments. In Figure 6.4, I present the first derivative RC spectra in (a) - PEPI/$MoSe_2$

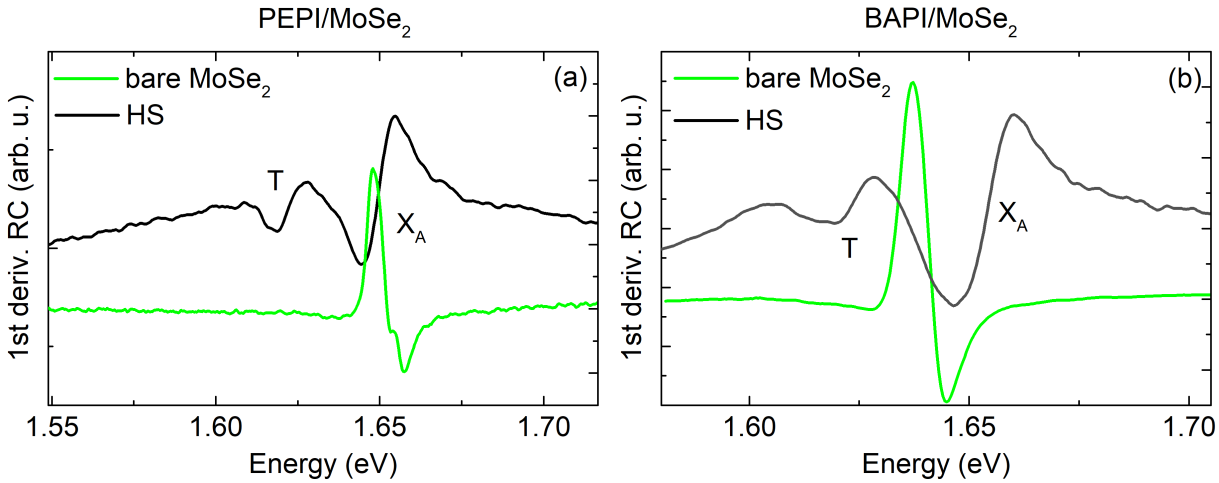

Figure 6.4: The first derivative RC spectra collected on bare $MoSe_2$ (green curve) and in the HS region (black curve) in (a) - PEPI/$MoSe_2$ and (b) - BAPI/$MoSe_2$ stacks.

and (b) - BAPI/$MoSe_2$ stacks. Qualitatively, the results are the same in both structures. On bare $MoSe_2$, I observe a single resonance of the neutral exciton X_A, whereas in the HS region, two absorption transitions - of neutral (X_A) and charged (T) excitons can be distinguished [115, 186, 268–270, 272]. The presence of T in the HS region implies that the concentration of excess carriers (and density of T absorptive states) in $MoSe_2$ is increased compared to bare $MoSe_2$ in both investigated stacks [270, 272]. The increased excess carrier density is the result of the transfer of charge between the TMD and perovskite flakes. According to the DFT calculations, in both stacks, the transfer of electrons from perovskite to $MoSe_2$ is energetically unfavorable. The other possible process that could increase the concentration of free carriers in $MoSe_2$ is the transfer of holes from $MoSe_2$ towards PEPI or BAPI perovskite. The hole transfer increases the concentration of free electrons in $MoSe_2$ and, as a result, the concentration of charged excitonic absorption states.

To check if the absorption of T is observed only in the HS region, I conduct the RL spatial mapping experiment. In Figure 6.5, I present the first derivative RC spectra extracted from the RL map on different spots on bare $MoSe_2$ (left panel) and in the HS region (right panel) in (a) - PEPI/$MoSe_2$ and (b) - BAPI/$MoSe_2$ stacks. It is clear that in both structures on bare $MoSe_2$ only the absorption transition of X_A is visible, whereas in the HS region, the absorption of T is observed next to X_A. The same qualitative results in PEPI/$MoSe_2$

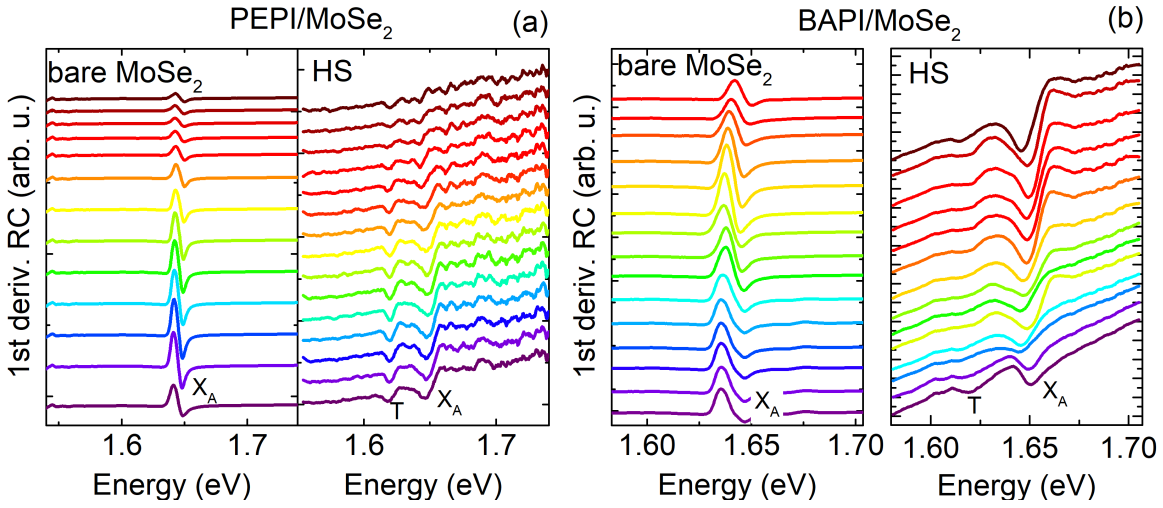

Figure 6.5: The first derivative RC spectra extracted from the RL spatial map on bare $MoSe_2$ and in the HS region in (a) - PEPI/$MoSe_2$ and (b) - BAPI/$MoSe_2$ stack.

and BAPI/$MoSe_2$ stacks are in agreement with the similar band alignment predicted by the theory.

Another signature of the CT in PEPI/$MoSe_2$ and BAPI/$MoSe_2$ stacks was observed in the PL experiment. In Figure 6.6 (a), I present the PL spectra collected on bare $MoSe_2$ (green curve) and in the HS region (black curve) in PEPI/$MoSe_2$ stack. On bare $MoSe_2$, I observe two peaks that correspond to the neutral and charged excitons [186, 270, 273–275]. In the HS region, both of these peaks have reduced PL intensities by around a factor of 10. This significant intensity reduction is accompanied by an increase of the T/X_A PL intensity ratio which is ~ 3 in the HS region compared to the ratio of ~ 1 on bare $MoSe_2$. The larger T/X_A

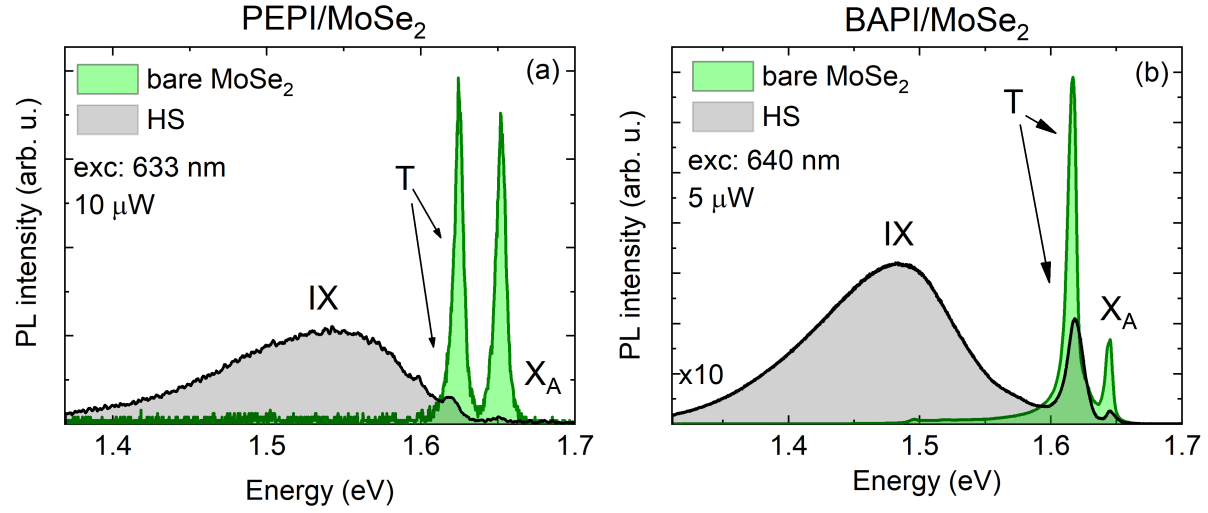

Figure 6.6: The PL spectra on bare $MoSe_2$ (green curve) and in the HS region (black curve) collected in (a) - PEPI/$MoSe_2$ and (b) - BAPI/$MoSe_2$ stacks. The PL spectrum in the HS region in BAPI/$MoSe_2$ stack was multiplied by 10 for clarity.

ratio on the HS than on bare $MoSe_2$ is in agreement with the RL studies presented above and suggests that the holes are transferred from $MoSe_2$ to PEPI resulting in an increased density of free electrons and the concentration of charged excitons with respect to neutral excitons.

In the PL spectrum in the HS region, I observe also a broad and strong peak at $\sim$ 1.54 eV that is not visible on bare $MoSe_2$. The observation of the signatures of CT leads me to assign this peak, redshifted with respect to the intralayer exciton peaks, to the interlayer excitons (IXs). The electrons that stay in the $MoSe_2$ layer and holes transferred to the PEPI layer bind across the heterostructure leading to the IX emission. The PL peaks of the IXs in the TMD/TMD stacks are redshifted with respect to the intralayer excitons due to the type II band alignment, where carriers relax to their respective band minima [8, 299–301]. Below, I will present multiple arguments in favor of the assignment of peak at 1.54 eV to IX.

Qualitatively, analogous effect is observed in the PL spectra for BAPI/$MoSe_2$ stack, shown in Figure 6.6 (b). On bare $MoSe_2$, I observe two peaks assigned previously to the X_A and T excitons (see Chapter 4) [270, 274–277]. In the HS region, the reduction of the PL intensities of X_A and T peaks is more prominent than in PEPI/$MoSe_2$ stack - by a factor of 30 (note that the PL spectrum in the HS region in Figure 6.6 (b) is multiplied by 10). This large decrease in intensity is accompanied by an increase of the T/X_A ratio ($\sim$ 5 on bare $MoSe_2$ vs. $\sim$ 18 in the HS region). I observe also a broad, low-energy peak at $\sim$ 1.48 eV which is absent on bare $MoSe_2$. In an analogy to PEPI/$MoSe_2$ stack, I attribute this peak to the IX transition.

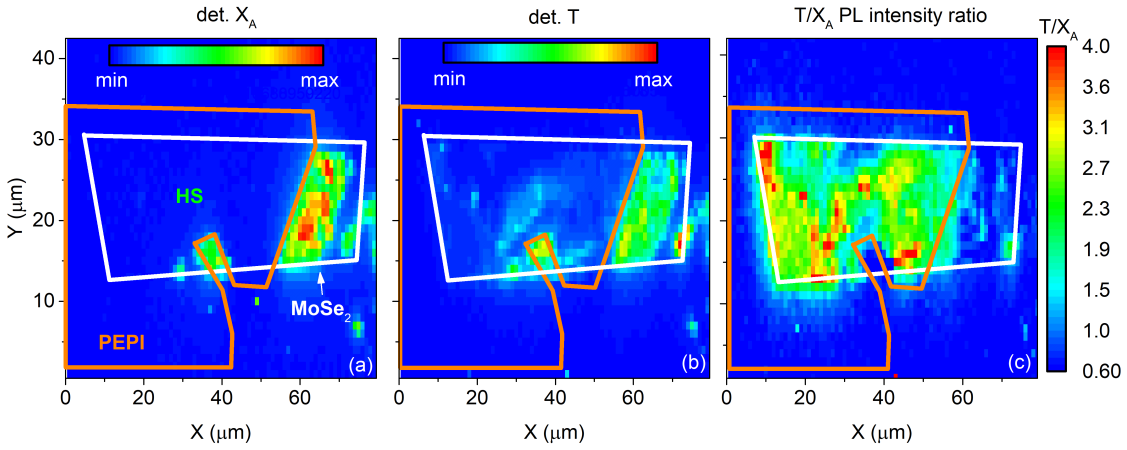

Figure 6.7: The false color PL intensity map of (a) - X_A and (b) - T in PEPI/$MoSe_2$ stack. The PEPI and $MoSe_2$ flakes are enclosed by orange and white broken lines, respectively. The blue and red colors represent the lowest and the highest emission intensity, respectively. (c) - The spatially resolved T/X_A PL intensity ratio in PEPI/$MoSe_2$ stack. λ_{exc} = 633 nm.

To check how robust are the observations presented above, I conduct the PL spatial mapping experiment. In Figure 6.7, I present the false color PL intensity maps of (a) - X_A and (b) - T in PEPI/$MoSe_2$ stack. The maps were acquired by integrating the PL intensity of neutral exciton (in the range from 1.640 eV to 1.660 eV) and charged exciton (from 1.614 eV to 1.631 eV). Both X_A and T peaks exhibit the PL intensity reduction in the HS region compared to bare $MoSe_2$ which is consistent with the analysis of the single PL spectrum presented above. To check how the excess carrier concentration in $MoSe_2$ is changed in PEPI/$MoSe_2$ stack, I calculate the spatially resolved T/X_A ratio, as shown in Figure 6.7 (c). It is clear that the ratio is increased in the HS region up to around 2.7 compared to the ratio on bare $MoSe_2$ which is around 1.2. This implies that the concentration of excess carriers in $MoSe_2$ is higher in the HS region than on bare $MoSe_2$ which can be explained by the transfer of holes from $MoSe_2$ to PEPI.

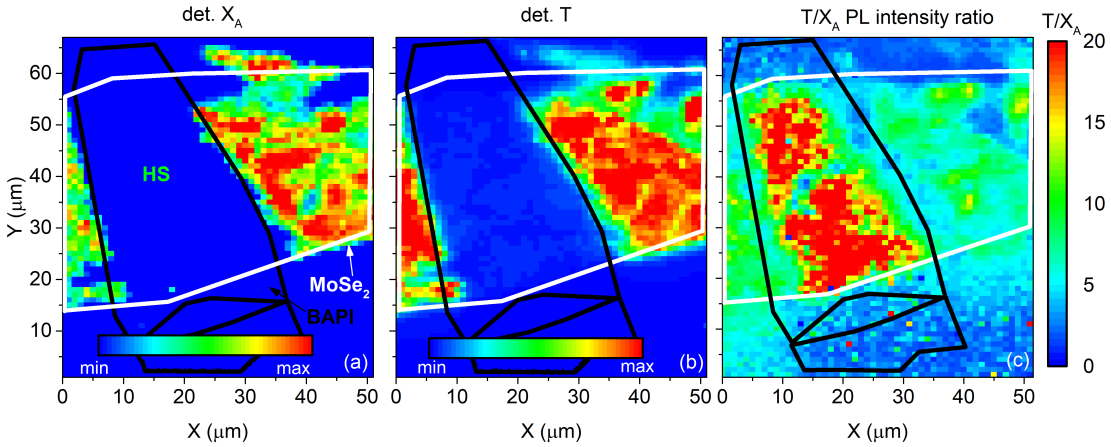

Figure 6.8: The false color PL intensity map of (a) - X_A and (b) - T in BAPI/$MoSe_2$ stack. The white and black broken lines enclose the $MoSe_2$ and BAPI flakes, respectively. The blue and red colors represent the lowest and the highest emission intensity, respectively. (c) - The spatially resolved T/X_A PL intensity ratio in BAPI/$MoSe_2$ stack. $\lambda_{exc} = 640$ nm.

Similar qualitative results were observed in BAPI/$MoSe_2$ stack. In Figure 6.8, I present the false color maps of the integrated PL intensity of (a) - X_A (from 1.636 eV to 1.650 eV) and (b) - T (from 1.600 eV to 1.630 eV) in BAPI/$MoSe_2$ stack. I observe that the PL intensity of both neutral and charged exciton is reduced in the HS region compared to bare $MoSe_2$. Simultaneously, the T/X_A PL intensity ratio is increased - from around 8 on bare $MoSe_2$ to around 18 in the HS region, as presented in Figure 6.8 (c). All these observations suggest the presence of CT from $MoSe_2$ to BAPI.

To gain a better insight into the origin of the IX peak, I study its PL intensity in the spatial mapping experiment. In Figure 6.9, I show the false color PL intensity maps of IX in (a) - PEPI/$MoSe_2$ and (b) - BAPI/$MoSe_2$ stacks. The maps were obtained by integrating

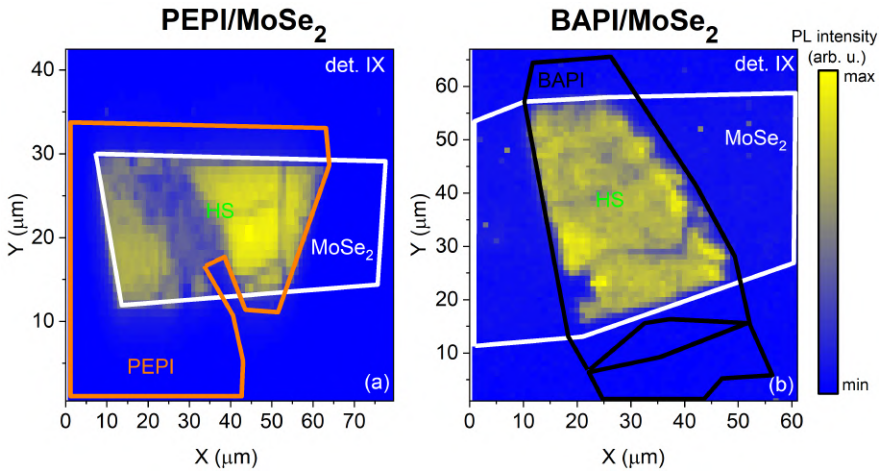

Figure 6.9: The false color PL intensity map of IX in (a) - PEPI/$MoSe_2$ and (b) - BAPI/$MoSe_2$ stacks. The maps were obtained by integration of the IX peak in the range (a) - from 1.40 eV to 1.57 eV, and (b) - from 1.35 eV to 1.55 eV.

the PL intensity of IX peak from 1.40 eV to 1.57 eV in PEPI/$MoSe_2$ and from 1.35 eV to 1.55 eV in BAPI/$MoSe_2$ stack. Importantly, in both structures, the IX peak is observed only in the HS region. This observation supports the early conclusion that the peak originates from the interlayer exciton transition.

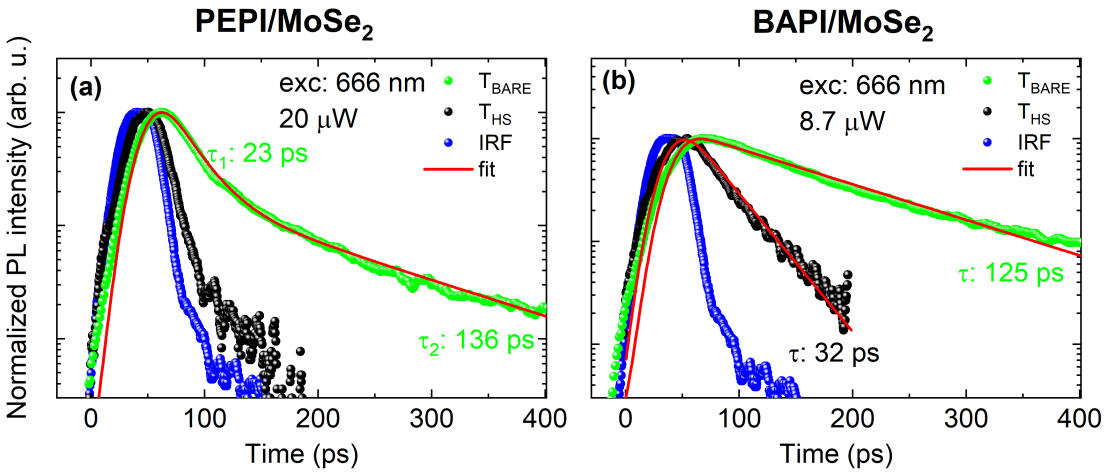

Figure 6.10: The PL decays of T on bare $MoSe_2$ (T_{BARE} - green spheres) and in the HS region (T_{HS} - black spheres) in (a) - PEPI/$MoSe_2$ and (b) - BAPI/$MoSe_2$ stack. The decays were extracted from the streak images. The IRF is shown as blue spheres. Fits with the exponential functions convoluted with IRF are shown as red solid curves.

Another signature of the CT in PEPI/$MoSe_2$ and BAPI/$MoSe_2$ stacks was observed in the time-resolved PL experiment. The PL decays (extracted from the streak camera images) were obtained by the resonant excitation in the X_B state of $MoSe_2$ ($\lambda_{exc} = 666$ nm). As the PL intensity of X_A in the HS region in both samples was too low, I could not obtain the

PL decays of the X_A transition. In Figure 6.10, I show the PL decays of T on bare $MoSe_2$ (T_{BARE} - green spheres) and in the HS region (T_{HS} - black spheres) in (a) - PEPI/$MoSe_2$ and (b) - BAPI/$MoSe_2$ stacks. To estimate the PL decay times of the charged excitonic transitions, I fit the PL decays with the convolution of the instrument function response (IRF - shown as blue spheres) with the exponential functions. For PEPI/$MoSe_2$ stack, I fit the biexponential $I(t) = A_1\exp(-t/\tau_1) + A_2\exp(-t/\tau_2) + I_0$, and for BAPI/$MoSe_2$ stack, I fit the monoexponential function $I(t) = A_1\exp(-t/\tau_1) + I_0$, where A (τ) is the amplitude (decay time), I_0 is the background level, and subscripts 1 and 2 denote the component 1 and 2. In PEPI/$MoSe_2$ stack, the charged exciton on bare $MoSe_2$ exhibits a biexponential decay with a short and long component of 23 ps and 136 ps, respectively. In the HS region, the PL decay of T is comparable to IRF and I cannot estimate the decay time of this transition. However, it is clear that the PL decay time of T in the HS region is several times shorter compared to T on bare $MoSe_2$. The reduced decay time of charged exciton PL indicates that an additional relaxation channel for T was formed in the HS region. According to the predictions of band alignment, the channel that reduces the population of charged excitons and increases its decay rate is the transfer of holes from $MoSe_2$ to PEPI.

The same qualitative results were observed in BAPI/$MoSe_2$ stack. The charged exciton on bare $MoSe_2$ and in the HS region exhibits a monoexponential decay with a PL decay time of around 125 ps and 32 ps, respectively. Therefore, the PL decay time of T in the HS region is reduced by a factor of 4 with respect to bare $MoSe_2$. This PL decay time shortening, like in PEPI/$MoSe_2$ stack, implies the influence of the CT from TMD to the perovskite layer.

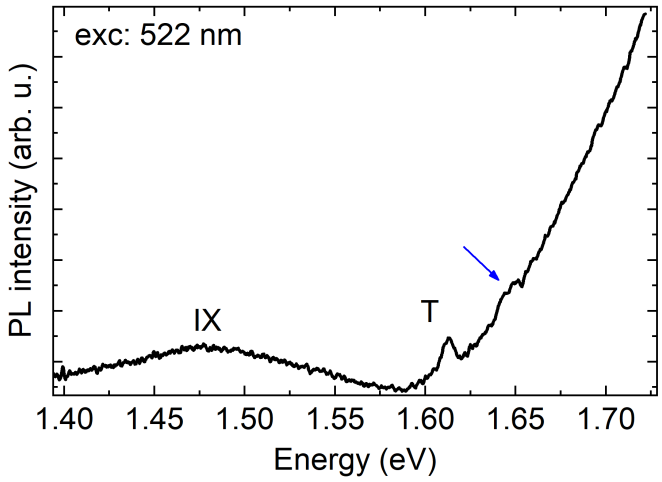

Figure 6.11: The PL spectrum in the HS region in PEPI/$MoSe_2$ stack at $\lambda_{exc} = 522$ nm. The blue arrow indicates a weakly visible X_A peak.

To better understand the origin of the IX peak, I also conduct the PLE experiment employing the excitation range covering the perovskite and TMD absorption, i.e. from

1.80 eV to 2.65 eV. Importantly, when exciting resonantly the X_{PEPI} or X_{BAPI} state, in the PL spectrum in the HS region, a strong low-energy emission of PEPI or BAPI at $\sim$ 1.80 eV covered mostly the weak peak of the X_A transition, as shown by a blue arrow in Figure 6.11. Therefore, the PLE spectrum of X_A in the HS region could not be obtained in both samples. Hence, in the PLE experiment, I monitor the PL intensities of X_A and T on bare $MoSe_2$, and T and IX in the HS region. The PL intensities were obtained by integrating the respective peaks, and normalized to the PL intensity of the corresponding peaks at 1.86 eV.

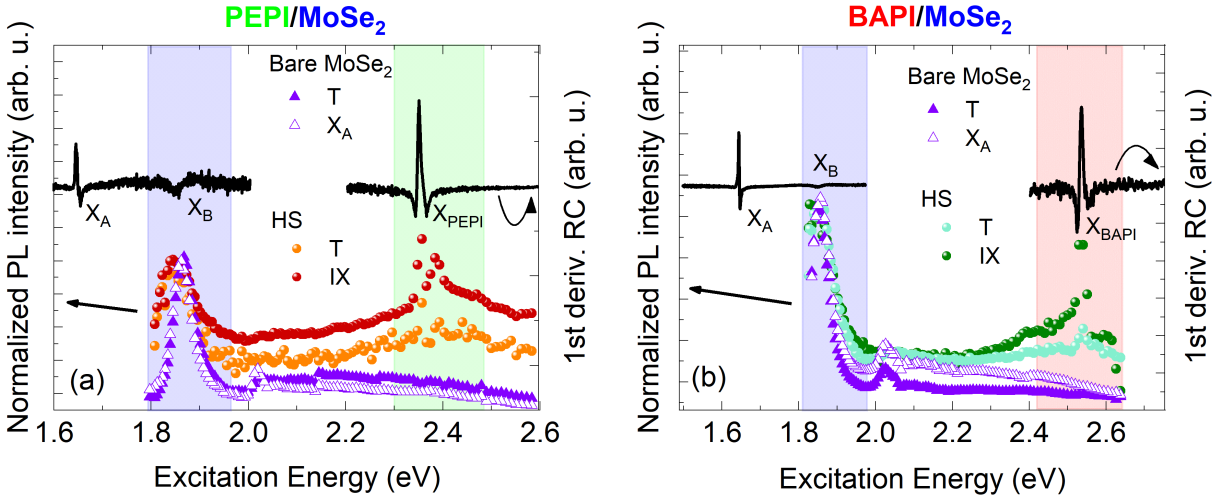

Figure 6.12: The PLE spectra in (a) - PEPI/$MoSe_2$ and (b) - BAPI/$MoSe_2$ stack. Violet empty and full triangles indicate the PL intensities of X_A and T peaks, respectively, on bare $MoSe_2$. In the HS region in PEPI/$MoSe_2$ stack, the orange and red spheres represent the PL intensities of T and IX, respectively. In the HS region in BAPI/$MoSe_2$ stacks, the cyan and green spheres represent the PL intensities of T and IX, respectively. Black curves are the first derivative RC spectra on bare $MoSe_2$, bare PEPI and bare BAPI. The blue, green and red rectangles roughly indicate the excitation energy range of X_B, X_{PEPI} and X_{BAPI}, respectively.

First, I will discuss the PLE spectra in PEPI/$MoSe_2$ stack presented in Figure 6.12 (a). For bare $MoSe_2$, starting from the low excitation energy and moving toward high energies, the PL intensities of X_A and T are initially enhanced with the maximum at around 1.86 eV. In the literature, the reported exciton B (X_B) absorption energy in the hBN-encapsulated $MoSe_2$ is $\sim$ 1.86 eV [269–272]. The X_B transition at $\sim$ 1.86 eV is also evidenced by a first derivative RC spectrum collected on bare $MoSe_2$ (shown as a black curve). Therefore, I attribute the observed PLE peak to the excitation of X_A and T via the X_B state. When the excitation energy is increased from 1.86 eV, the PL intensity of X_A and T decreases as a result of shifting away from the absorbing excitonic B state [204, 293]. Another small resonance of X_A and T is observed at $\sim$ 2.05 eV. This PL intensity enhancement may correspond to the excitation

of X_A and T via the excited state of X_B [73]. When the excitation energy is further increased, the PL intensities of neutral and charged excitons are roughly constant.

In the HS region in PEPI/$MoSe_2$ stack, the shape of the PLE spectrum of T is similar to the spectrum of bare $MoSe_2$. The PL intensity of T increases, as the resonance with X_B is approached, and above around 1.98 eV, the PLE spectrum of T is mostly flat. In the PLE spectrum of IX, two peaks can be distinguished - at 1.85 eV and 2.36 eV. The low-energy peak corresponds to X_B, whereas the high-energy peak is attributed to the X_{PEPI} transition as evidenced by comparison with the first derivative RC spectra on bare $MoSe_2$ and bare PEPI shown as the black curves. Therefore, I can interpret the observed PLE peaks of IX as a consequence of the excitation of IX via X_B in $MoSe_2$ and X_{PEPI} in the PEPI layer. The possibility of the IX excitation via both constituent materials in PEPI/$MoSe_2$ stack is another indication that IX peak corresponds to the recombination of interlayer excitons [7, 186].

Similar results were obtained in BAPI/$MoSe_2$ stack, as shown in the PLE spectra in Figure 6.12 (b). On bare $MoSe_2$, the neutral and charged excitons PL exhibits a resonance at 1.85 eV which corresponds to the excitation via X_B [269–271]. I observe also a resonance at $\sim$ 2.05 eV which may correspond to the excitation via an excited state of X_B [73].

In the HS region, the charged exciton peak exhibits a resonance at 1.85 eV which I attribute to the excitation via the X_B state. Strikingly, the PL intensity of the T peak exhibits another resonance with the perovskite X_{BAPI} state at $\sim$ 2.53 eV which is evidenced by the first derivative RC spectrum on bare BAPI. Note that for PEPI/$MoSe_2$ stack no excitation of the T peak via X_{PEPI} state in PEPI was observed (see Figure 6.12 (a)). I will discuss the potential origin of this PLE peak in Section 6.4. The PLE spectrum of IX exhibits three resonances: at $\sim$ 1.85 eV, $\sim$ 2.38 eV and $\sim$ 2.53 eV which correspond to the excitation via the X_B state in $MoSe_2$, via the exciton state in the high-temperature phase of BAPI (it is usually present even at 5 K [302]) and via the exciton state in the low-temperature phase of BAPI (X_{BAPI}), respectively. The excitation via excitonic states in both TMD and perovskite is another piece of evidence that the IX peak corresponds to the recombination of the interlayer excitons.

According to the DFT calculations of band structure and PDOS presented in Section 6.2, the type II band alignment in PEPI/$MoSe_3$ and BAPI/$MoSe_2$ stacks facilitates the transfer of the photoexcited holes from $MoSe_2$ to the PEPI or BAPI layer. The CT was evidenced by the RL, PL, spatial mapping, PLE and time-revolved PL experiments and it has two important consequences presented schematically in Figure 6.13. On one hand, the CT (indicated by green curved arrows) leads to the increased concentration of free electrons (green dots) in the $MoSe_2$ layer. These electrons interact with neutral excitons and form charged excitons,

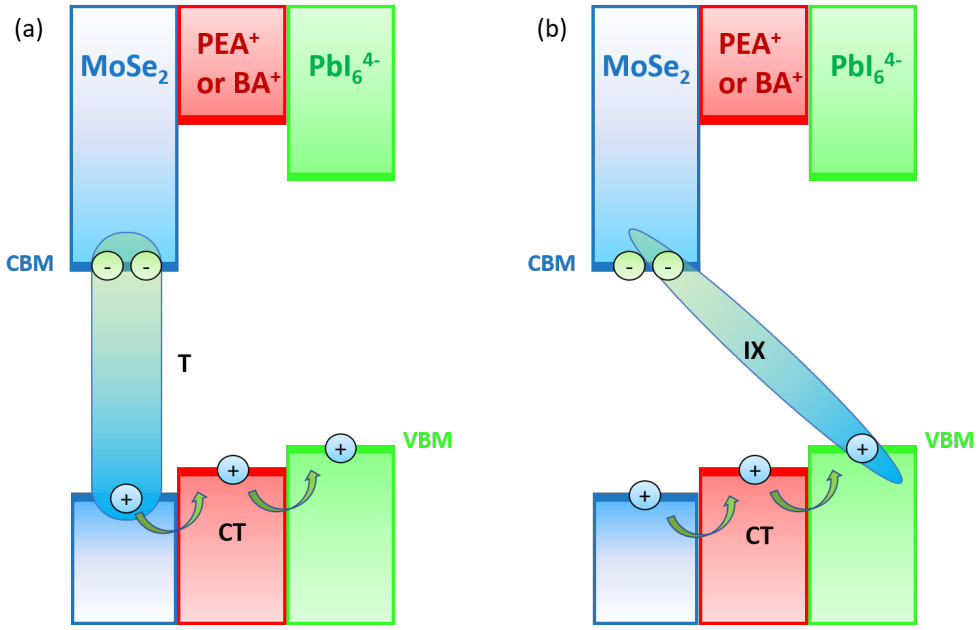

Figure 6.13: Proposed mechanism of (a) - T and (b) - IX formation in PEPI/$MoSe_2$ and BAPI/$MoSe_2$ stacks. The blue, red and green rectangles indicate the VB and CB in $MoSe_2$, PEA^+ or BA^+, and PbI_6^{4-} layers, respectively. The blue (green) dots represent the holes (electrons). The green curved arrows indicate the hole transfer from $MoSe_2$ to the PEPI or BAPI perovskite layer. The blue-green shape indicates the formation of (a) - T and (b) - IX.

as presented by the blue-green shape in Figure 6.13 (a). Additionally, the electrons located in the $MoSe_2$ layer bind with the holes (blue dots) transferred to the PEPI or BAPI layer and form IXs, as shown by the blue-green oval in Figure 6.13 (b).

6.4 Manipulation of the excitation transfer mechanism in PEPI/$MoSe_2$ and BAPI/$MoSe_2$

In this Section, I will discuss the possibility of controlling the mechanism of excitation transfer in 2D perovskite/TMD stacks by employing different organic spacer compounds in the 2D perovskite material.

In the PLE spectrum in Figure 6.12 (b), I observed that the PL intensity of T in the HS region in BAPI/$MoSe_2$ stack exhibits two resonances - at 1.85 eV (corresponding to the excitation via X_B) and 2.53 eV (corresponding to the excitation via X_{BAPI} state). According to the literature, I conclude that the energy of X_{BAPI} is close to the energy of the exciton C in the band nesting region of the Brillouin zone in monolayer $MoSe_2$ [73, 97, 98, 235]. As the transfer of electrons from BAPI to $MoSe_2$ is energetically unfavorable, the observed resonance in the PLE spectrum of T at 2.53 eV suggests the

presence of the ET. Therefore, in BAPI/$MoSe_2$ stack, next to the transfer of holes from $MoSe_2$ to BAPI, there is also ET from the ground exciton X_{BAPI} state to the exciton C state in $MoSe_2$. Importantly, no resonance of T via X_{PEPI} state was observed in the HS region in PEPI/$MoSe_2$ stack (see Figure 6.12 (a)). This is expected since the energy of X_{PEPI} is much lower than the energy of the exciton C and much higher than the energy of exciton B in $MoSe_2$ [97, 98]. These experimental results highlight the important role that the organic spacers play in determining the optical properties of 2D perovskite/TMD stacks. By simply employing 2D perovskites with different organic spacer cations, the excitation transfer (via the ET mechanism) can be enabled or disabled which strictly depends on the energy resonance of the excitonic states in 2D perovskite and TMD constituents.

6.5 Properties of IX in PEPI/$MoSe_2$ and BAPI/$MoSe_2$ stacks

In this Section, I will discuss further the properties of IX in both investigated stacks.

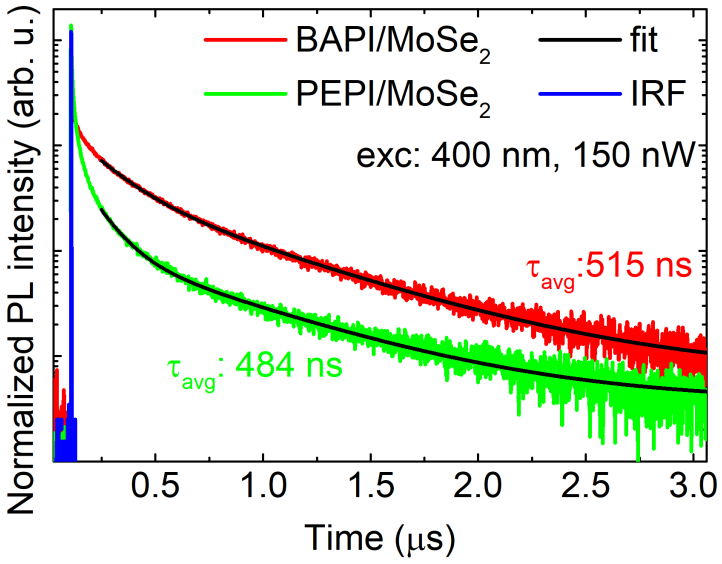

Figure 6.14: The PL decays of IX in PEPI/$MoSe_2$ (green curve) and BAPI/$MoSe_2$ (red curve). Fits with bi-exponential functions are shown as black solid curves. The IRF is shown as a blue curve.

To assess the PL decay time of IX, I conduct the time-resolved PL experiment in the ns time domain. In Figure 6.14, I present the PL decays of IX collected in PEPI/$MoSe_2$ (green curve) and BAPI/$MoSe_2$ (red curve). The PL decays were fitted with bi-exponential

functions (black curves). The average IX decay time was calculated according to the formula $\tau_{avg} = (A_1\tau_1^2 + A_2\tau_2^2)/(A_1\tau_1 + A_2\tau_2)$, where A_1 (A_2) and τ_1 (τ_2) is the fitted amplitude and decay time for component 1 (2) of the PL decay of IX. In PEPI/$MoSe_2$ stack, the short and long decay time components are 109 ns and 618 ns, respectively, giving an average decay time of 484 ns. In BAPI/$MoSe_2$ stack, the short and long components are 173 ns and 636 ns, respectively, with an average decay time of 515 ns. Therefore, the average decay time of IX in both stacks is more than 3 orders of magnitude longer than the decay time of T on bare $MoSe_2$, as was shown in Section 6.3. The long PL decay time of IX stems from the large spatial separation of electrons and holes that bind across the interface [7, 8, 299]. The large inter-carrier distance reduces the overlap of the carrier wavefunctions which in turn significantly reduces the IX oscillator strength leading to an increased recombination time. The several orders of magnitude longer decay times of IX with respect to the intralayer excitons were previously reported in other van der Waals stacks, such as MoS_2/$MoSe_2$/MoS_2 or $MoSe_2$/WSe_2 [7, 8]. The multi-exponential PL decay of IX observed in both PEPI/$MoSe_2$ and BAPI/$MoSe_2$ stacks might be an indication that the adhesion between the TMD and perovskite flakes is nonhomogenous and the 2D perovskite-TMD distances fluctuate across the excitation spot. The distance variations between the electrons and holes lead to differences in the PL decay time resulting in the multi-exponential IX decays.

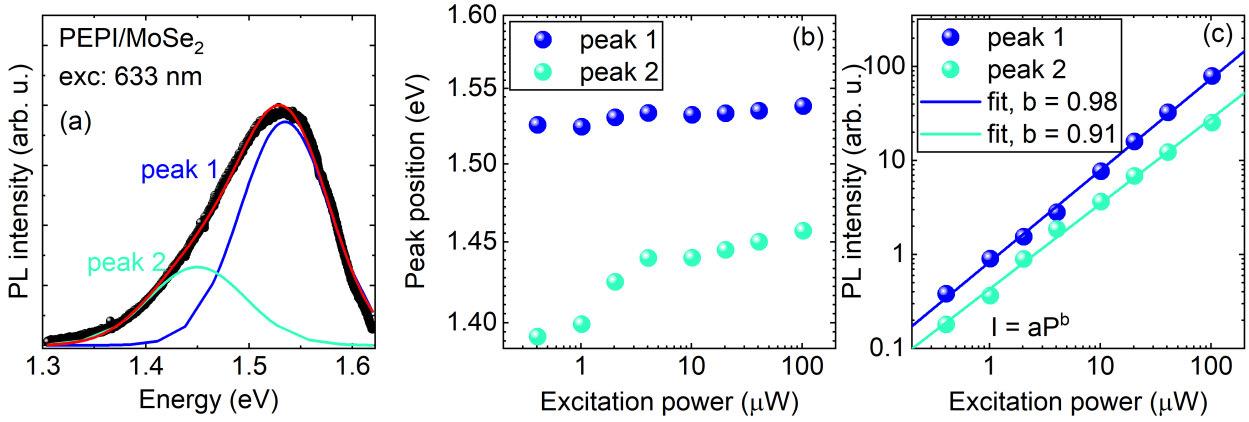

Figure 6.15: (a) - The PL spectrum in the HS region in PEPI/$MoSe_2$ stack. The IX peak (black spheres) is fitted with two Gaussian components (blue and cyan curves). The fit is shown as a red curve. (b) - The positions of the IX components 1 and 2 as a function of the excitation power in PEPI/$MoSe_2$ stack. (c) - The PL power dependence of the IX components in PEPI/$MoSe_2$ stack. The fits with the power law function are shown as blue and cyan solid lines.

In Figure 6.15, I present the results of the power-dependent PL experiment for IX transition in PEPI/$MoSe_2$ stack. To evaluate the dependence of the peak position and PL intensity on the excitation power, I fit the IX peak with two Gaussian functions, as shown in the PL spectrum in Figure 6.15 (a). As presented in Figure 6.15 (b), both the

high-energy component (I will refer to it as peak 1) and the low-energy component (peak 2) are gradually blueshifted when the excitation power is increased - peak 1 shifts by around 13 meV, while the shift of peak 2 is on the order of 65 meV. In Chapter 1, I discussed that the IXs are composed of electrons and holes that bind across the interface forming a permanent out-of-plane electric dipole [301, 303]. When the excitation power is increased, the density of photogenerated IXs also increases. The IX dipoles start interacting with each other and the repulsive interactions then lead to the shift of the IX energy states towards higher energies [8, 301]. The blueshift of the IX emission peak on the order of 10 meV to 50 meV was previously observed in other van der Waals stacks, such as $MoSe_2/WSe_2$ [7, 8, 301, 303].

In Figure 6.15 (c), I present the PL intensity of the IX components as a function of the excitation power. The fitting of the extracted PL intensities with a power law function gives the exponent b of $\sim$ 0.98 for peak 1 and 0.91 for peak 2. The obtained b is not typical for IXs in TMD/TMD stacks, where the power dependence is usually sublinear [7–9, 301]. The sublinear dependence occurs as a consequence of saturating the available IX states - an effect resulting from the fact that the CT rate is orders of magnitude faster than the IX recombination rate - the reported CT rates in TMD/TMD stacks are in the fs regime, whereas the IX decay times are in the ns regime [7, 8, 28, 187, 188, 204]. The almost linear power dependence observed in PEPI/$MoSe_2$ stack suggests that the excitation power was too low to saturate all the available IX optically active states.

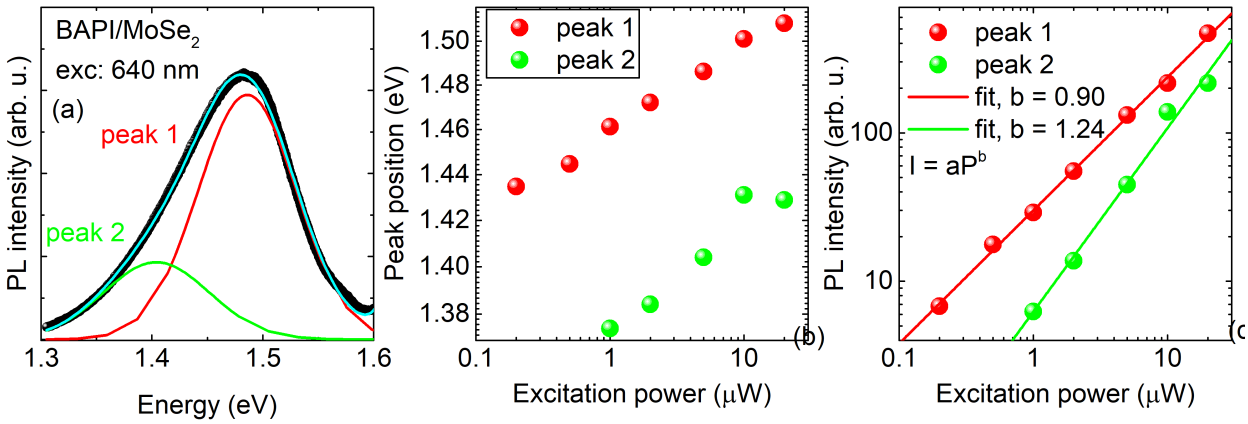

Figure 6.16: (a) - The PL spectrum in the HS region in BAPI/$MoSe_2$ stack. The IX peak (black spheres) is fitted with two Gaussian components (red and green curves). The fit is shown as a cyan curve. (b) - The positions of IX components as a function of the excitation power in BAPI/$MoSe_2$ stack. (c) - The PL power dependence of the IX components in BAPI/$MoSe_2$ stack. The fits with a power law function are shown as red and green solid lines.

In Figure 6.16, I present the PL power dependence studies in BAPI/$MoSe_2$ stack. Similarly to PEPI/$MoSe_2$ stack, the IX peak is fitted with two Gaussian functions, as shown in Figure 6.16 (a). It is important to note that the low-energy component (peak

2) emerges at a power of $\sim$ 1 µW, while the high-energy component (peak 1) is present in the whole excitation power range. Interestingly, the blueshift of peak 2 with increasing excitation power is much more pronounced in BAPI/$MoSe_2$ than in PEPI/$MoSe_2$ stack which suggests its different origin. The obtained positions of peak 1 and peak 2 show the maximum blueshift of 73 meV (for peak 1) and 55 meV (for peak 2), as shown in Figure 6.16 (b). In Figure 6.16 (c), I present the power dependence of the IX emission intensity. The fitting with the power law function has given the exponent of 0.90 for peak 1 and 1.24 for peak 2. The superlinear power dependence of peak 2 also implies that its origin is different than the origin of the low-energy component in PEPI/$MoSe_2$ stack. Further studies are needed to better understand the power dependence of IX in 2D perovskite/TMD stacks.

6.6 Conclusions

In this Chapter, I confronted the theoretically predicted band alignment with the steady-state and time-resolved spectroscopic studies of PEPI/$MoSe_2$ and BAPI/$MoSe_2$ van der Waals stacks. The DFT calculations have shown that both stacks exhibit a particular type II band alignment, where the transfer of electrons from the perovskite to $MoSe_2$ layer is blocked by a barrier introduced by the organic spacer.

According to the presented spectroscopic results, the main mechanism of excitation transfer in the investigated stacks is the CT. Following this process, the electron in $MoSe_2$ and the hole in perovskite bind across the interface giving rise to IX, observed as a broad, asymmetric PL peak below the energy of intralayer excitons of $MoSe_2$.

In this Chapter, I have also shown that the influence of the organic spacers on the band structure in 2D perovskites enables the manipulation of the excitation transfer mechanism in 2D perovskite/TMD stacks. In the PLE experiment, I have shown that by using different organic spacers, the energy of the exciton states in 2D perovskite material can be shifted to enable resonance with the exciton states in the TMD layer. As a result, in BAPI/$MoSe_2$ stack the ET is observed, while in PEPI/$MoSe_2$ stack it is not.

Conclusions and outlook

The subject of van der Waals stacks composed of 2D perovskites and monolayer TMDs is a fairly new topic of research, where the understanding of their fundamental electronic properties is still lacking. The results presented in this thesis obtained by means of optical spectroscopy at low temperature provide an important insight into the mechanism of excitation transfer and its manipulation in 2D perovskite/TMD heterostructures.

The studied heterostructures were composed of one of the most understood representative materials from both families, namely the PEPI and BAPI perovskites, and WS_2 and $MoSe_2$ monolayers.

The first principle calculations (obtained in cooperation with the University of Dresden) have shown that all investigated heterostructures exhibit type II band alignment, where the transfer of electrons from the perovskite to the TMD layer is blocked by a high-energy barrier introduced by the organic spacer.

In PEPI/WS_2 stack, the increased charged-to-neutral exciton PL intensity ratio in the HS region was a hallmark of an increased excess electron concentration. The ET was evidenced in the PLE experiment - the PL intensities of neutral and charged excitons of WS_2 were increased when the ground or excited PEPI exciton states were resonantly excited.

In both PEPI/$MoSe_2$ and BAPI/$MoSe_2$ heterostructures, the signature of the transfer of holes was the formation of IX. The IX was observed as a broad PL peak redshifted with respect to the energy of excitons of bare $MoSe_2$ and bare PEPI or BAPI.

Apart from CT, the ET was also evidenced in BAPI/$MoSe_2$ stack. The results from the PLE experiment have shown that the ET takes place from BAPI exciton state to the exciton C state in $MoSe_2$. The ET was not observed in PEPI/$MoSe_2$ stack, where the exciton states in PEPI and $MoSe_2$ are not in resonance.

In this thesis, I have shown that the main mechanism of excitation transfer in 2D perovskite/TMD stacks is via the CT but the transfer via ET can emerge when different organic spacer compounds are employed in 2D perovskite. The results obtained in this work pave the way for future research of the rich family of heterostructures that is

2D perovskite/TMD stacks. For instance, the mechanism of the ET could be further investigated by estimating the ET rate as a function of temperature. This would enable to distinguish FRET from Dexter ET mechanism, where the transfer of both carriers from one material to the other in heterostructures with type II band alignment would be a thermally activated process. More detailed insight into the dynamics of CT and ET could be provided by transient absorption spectroscopy. Furthermore, to investigate the possibility of the transfer of spin, the polarization-dependent PLE spectroscopy could be employed. In the future, the efficient CT in 2D perovskite/TMD stacks could find applications in ultrathin, wearable photovoltaic devices.

Bibliography

[1] W. Li, M.D. Brubaker, B. T. Spann, K. A. Bertness, and P. Fay. GaN nanowire MOSFET with near-ideal subthreshold slope. *IEEE Electron Device Letters*, 39(2):184–187, 2018.

[2] V. M. Ustinov and A. E. Zhukov. GaAs-based long-wavelength lasers. *Semiconductor Science and Technology*, 15(8):41–54, 2000.

[3] B. Jo. H. Stadler. Vapor processes. In *Materials Processing*, pages 513–588. Elsevier, 2016.

[4] K. S. Novoselov, A. K. Geim, S. V. Morozov, D. Jiang, Y. Zhang, S. V. Dubonos, I. V. Grigorieva, and A. A. Firsov. Electric field effect in atomically thin carbon films. *Science*, 306(5696):666–669, 2004.

[5] A. K. Geim and I. V. Grigorieva. Van der Waals heterostructures. *Nature*, 499(7459):419–425, 2013.

[6] F. Withers, O. Del Pozo-Zamudio, A. Mishchenko, A. P. Rooney, A. Gholinia, K. Watanabe, T. Taniguchi, S. J. Haigh, A. K. Geim, A. I. Tartakovskii, and K. S. Novoselov. Light-emitting diodes by band-structure engineering in van der Waals heterostructures. *Nature Materials*, 14(3):301–306, 2015.

[7] M. Baranowski, A. Surrente, L. Klopotowski, J. M. Urban, N. Zhang, D. K. Maude, K. Wiwatowski, S. Mackowski, Y. C. Kung, D. Dumcenco, A. Kis, and P. Plochocka. Probing the interlayer exciton physics in a $MoS_2/MoSe_2/MoS_2$ van der Waals heterostructure. *Nano Letters*, 17(10):6360–6365, 2017.

[8] P. Rivera, J. R. Schaibley, A. M. Jones, J. S. Ross, S. Wu, G. Aivazian, P. Klement, K. Seyler, G. Clark, N. J. Ghimire, J. Yan, D. G. Mandrus, W. Yao, and X. Xu. Observation of long-lived interlayer excitons in monolayer $MoSe_2/WSe_2$ heterostructures. *Nature Communications*, 6(1):1–6, 2015.

[9] P. Rivera, K. L. Seyler, H. Yu, J. R. Schaibley, J. Yan, D. G. Mandrus, W. Yao, and X. Xu. Valley-polarized exciton dynamics in a 2D semiconductor heterostructure. *Science*, 351(6274):688–691, 2016.

[10] Y. Cao, V. Fatemi, S. Fang, K. Watanabe, T. Taniguchi, E. Kaxiras, and P. Jarillo-Herrero. Unconventional superconductivity in magic-angle graphene superlattices. *Nature*, 556(7699):43–50, 2018.

[11] K. Tran, G. Moody, F. Wu, X. Lu, J. Choi, K. Kim, A. Rai, D. A. Sanchez, J. Quan, A. Singh, J. Embley, A. Zepeda, M. Campbell, T. Autry, T. Taniguchi, K. Watanabe, N.u Lu, S. K. Banerjee, K. L. Silverman, S. Kim, E. Tutuc, L. Yang, A. H. MacDonald, and X. Li. Evidence for moiré excitons in van der Waals heterostructures. *Nature*, 567(7746):71–75, 2019.

[12] N. Flöry, P. Ma, Y. Salamin, A. Emboras, T. Taniguchi, K. Watanabe, J. Leuthold, and L. Novotny. Waveguide-integrated van der waals heterostructure photodetector at telecom wavelengths with high speed and high responsivity. *Nature Nanotechnology*, 15(2):118–124, 2020.

[13] R. Singh, A. Giri, M. Pal, K. Thiyagarajan, J. Kwak, J.-J. Lee, U. Jeong, and K. Cho. Perovskite solar cells with an MoS_2 electron transport layer. *Journal of Materials Chemistry A*, 7(12):7151–7158, 2019.

[14] G. Iannaccone, F. Bonaccorso, L. Colombo, and G. Fiori. Quantum engineering of transistors based on 2D materials heterostructures. *Nature Nanotechnology*, 13(3):183–191, 2018.

[15] Y. Kim, S. Lee, J.-G. Song, K. Y. Ko, W. J. Woo, S. W. Lee, M. Park, H. Lee, Z. Lee, H. Choi, W.-H. Kim, J. Park, and H. Kim. 2d transition metal dichalcogenide heterostructures for p- and n-type photovoltaic self-powered gas sensor. *Advanced Functional Materials*, 30(43):1–11, 2020.

[16] Y. Liu, S. Xie, H. Li, and X. Wang. A highly efficient sunlight driven ZnO nanosheet photocatalyst: Synergetic effect of p-doping and MoS_2 atomic layer loading. *ChemCatChem*, 6(9):2522–2526, 2014.

[17] M. Baranowski, A. Surrente, and P. Plochocka. Two dimensional perovskites/transition metal dichalcogenides heterostructures: Puzzles and challenges. *Israel Journal of Chemistry*, e202100120:1–14, 2021.

[18] J. Ghosh, L. P. L. Mawlong, M. G. B., A. J. Pattison, W. Theis, S. Chakraborty, and P. K. Giri. Solid-state synthesis of stable and color-tunable cesium lead halide perovskite nanocrystals and the mechanism of high-performance photodetection in a monolayer MoS_2/$CsPbBr_3$ vertical heterojunction. *Journal of Materials Chemistry C*, 8(26):8917–8934, 2020.

[19] T. Yang, X. Wang, B. Zheng, Z. Qi, C. Ma, Y. Fu, Y. Fu, M. P. Hautzinger, Y. Jiang, Z. Li, P. Fan, F. Li, W. Zheng, Z. Luo, J. Liu, B. Yang, S. Chen, D. Li, L. Zhang, S. Jin, and A. Pan. Ultrahigh-performance optoelectronics demonstrated in ultrathin perovskite-based vertical semiconductor heterostructures. *ACS Nano*, 13(7):7996–8003, 2019.

[20] B. Peng, G. Yu, Y. Zhao, Q. Xu, G. Xing, X. Liu, D. Fu, B. Liu, J. Rong, S. Tan, W. Tang, H. Lu, J. Xie, L. Deng, T. C. Sum, and K. P. Loh. Achieving ultrafast hole transfer at the monolayer MoS_2 and $CH_3NH_3PbI_3$ perovskite interface by defect engineering. *ACS Nano*, 10(6):6383–6391, 2016.

[21] A. Elbanna, K. Chaykun, Y. Lekina, Y. Liu, B. Febriansyah, S. Li, J. Pan, Z. X. Shen, and J. Teng. Perovskite-transition metal dichalcogenides heterostructures: recent advances and future perspectives. *Opto-Electronic Science*, 1(8):1–40, 2022.

[22] C. Ma, Y. Shi, W. Hu, M.-H. Chiu, Z. Liu, A. Bera, F. Li, H. Wang, L.-J. Li, and T. Wu. Heterostructured WS_2/$CH_3NH_3PbI_3$ photoconductors with suppressed dark current and enhanced photodetectivity. *Advanced Materials*, 28(19):3683–3689, 2016.

[23] G. Kakavelakis, I. Paradisanos, B. Paci, A. Generosi, M. Papachatzakis, T. Maksudov, L. Najafi, A. E. Del Rio Castillo, G. Kioseoglou, E. Stratakis, F. Bonaccorso, and E. Kymakis. Extending the continuous operating lifetime of perovskite solar cells with a molybdenum disulfide hole extraction interlayer. *Advanced Energy Materials*, 8(12):1–15, 2018.

[24] P. Huang, Z. Wang, Y. Liu, K. Zhang, L. Yuan, Y. Zhou, B. Song, and Y. Li. Water-soluble 2D transition metal dichalcogenides as the hole-transport layer for highly efficient and stable p-i-n perovskite solar cells. *ACS Applied Materials & Interfaces*, 9(30):25323–25331, 2017.

[25] Z. Liu, K. Liu, F. Zhang, S. M. Jain, T. He, Y. Jiang, P. Liu, J. Yang, H. Liu, and M. Yuan. $CH_3NH_3PbI_3$:MoS_2 heterostructure for stable and efficient inverted perovskite solar cell. *Solar Energy*, 195:436–445, 2020.

[26] K. Mahmood, A. Khalid, S. Waqas Ahmad, H. G. Qutab, M. Hameed, and R. Sharif. Electrospray deposited MoS_2 nanosheets as an electron transporting material for high efficiency and stable perovskite solar cells. *Solar Energy*, 203:32–36, 2020.

[27] C. Zhang, G. Lu, Y. Zhang, Z. Fang, H. He, and H. Zhu. Long-range transport and ultrafast interfacial charge transfer in perovskite/monolayer semiconductor heterostructure for enhanced light absorption and photocarrier lifetime. *The Journal of Chemical Physics*, 156(24):1–10, 2022.

[28] X. Hong, J. Kim, S.-F. Shi, Y. Zhang, C. Jin, Y. Sun, S. Tongay, J. Wu, Y. Zhang, and F. Wang. Ultrafast charge transfer in atomically thin MoS_2/WS_2 heterostructures. *Nature Nanotechnology*, 9(9):682–686, 2014.

[29] L. Wu, Y. Chen, H. Zhou, and H. Zhu. Ultrafast energy transfer of both bright and dark excitons in 2D van der waals heterostructures beyond dipolar coupling. *ACS Nano*, 13:2341–2348, 2019.

[30] Q. Wang and A. T. S. Wee. Upconversion photovoltaic effect of WS_2/2D perovskite heterostructures by two-photon absorption. *ACS Nano*, 15(6):10437–10443, 2021.

[31] Y. Chen, J. Ma, Z. Liu, J. Li, X. Duan, and D. Li. Manipulation of valley pseudospin by selective spin injection in chiral two-dimensional perovskite/monolayer transition metal dichalcogenide heterostructures. *ACS Nano*, 14(11):15154–15160, 2020.

[32] Q. Zhang, E. Linardy, X. Wang, and G. Eda. Excitonic energy transfer in heterostructures of quasi-2d perovskite and monolayer WS_2. *ACS Nano*, 14(9):11482–11489, 2020.

[33] Y. Chen, Z. Liu, J. Li, X. Cheng, J. Ma, H. Wang, and D. Li. Robust interlayer coupling in two-dimensional perovskite/monolayer transition metal dichalcogenide heterostructures. *ACS Nano*, 14(8):10258–10264, 2020.

[34] Q. Wei, X. Wen, J. Hu, Y. Chen, Z. Liu, T. Lin, and D. Li. Site-controlled interlayer coupling in WSe_2/2D perovskite heterostructure. *Science China Materials*, 65(5):1337–1344, 2022.

[35] Q. Wang, Q. Zhang, X. Luo, J. Wang, R. Zhu, Q. Liang, L. Zhang, J. Z. Yong, C. P. Y. Wong, G. Eda, J. H. Smet, and A. T. S. Wee. Optoelectronic properties of a van der waals WS2 monolayer/2D perovskite vertical heterostructure. *ACS Applied Materials & Interfaces*, 12(40):45235–45242, 2020.

[36] J. Frenkel. On the transformation of light into Heat in Solids. i. *Physical Review*, 37(1):17–44, 1931.

[37] M. Hayashi and K. Katsuki. Absorption spectrum of cuprous oxide. *Journal of the Physical Society of Japan*, 5(5):380B–381, 1950.

[38] O. Kühn. Frenkel exciton dynamics: A theoretical perspective. In *Handbook of Organic Materials for Electronic and Photonic Devices*, pages 259–279. Elsevier, 2019.

[39] K. Mizuno and A. Matsui. Frenkel exciton dynamics in anthracene under high pressure and quasi-free exciton state. *Journal of the Physical Society of Japan*, 55(7):2427–2435, 1986.

[40] H. Haug and S. W Koch. Quantum confinement effects in semiconductors. In *Applied Nanophotonics*, pages 52–91. Cambridge University Press, 2009.

[41] P. Y. Yu and M. Cardona. Optical properties i. In *Fundamentals of Semiconductors*, pages 243–344. Springer Berlin Heidelberg, 2010.

[42] F. Han. Optical properties of solids. In *A Modern Course in the Quantum Theory of Solids*, pages 499–579. WORLD SCIENTIFIC, 2012.

[43] A. Podhorodecki J. Misiewicz, G. Sk. *Optyczna spektroskopia nanostruktur*. OFICYNA WYDAWNICZA POLITECHNIKI WROCAWSKIEJ.

[44] A. Chernikov, T. C. Berkelbach, H. M. Hill, A. Rigosi, Y. Li, O. Burak A., D. R. Reichman, M. S. Hybertsen, and T. F. Heinz. Exciton binding energy and nonhydrogenic rydberg series in monolayer WS_2. *Physical Review Letters*, 113(7):1–5, 2014.

[45] F. Schöne, S.-O. Krüger, P. Grünwald, H. Stolz, S. Scheel, M. Aßmann, J. Heckötter, J. Thewes, D. Fröhlich, and M. Bayer. Deviations of the exciton level spectrum in Cu_2O from the hydrogen series. *Physical Review B*, 93(7):1–5, 2016.

[46] B. K. Ridley. The electron-phonon interaction in quasi-two-dimensional semiconductor quantum-well structures. *Journal of Physics C: Solid State Physics*, 15(28):5899–5917, 1982.

[47] M. Z. Maialle, E. A. de Andrada e Silva, and L. J. Sham. Exciton spin dynamics in quantum wells. *Physical Review B*, 47(23):15776–15788, 1993.

[48] R. G. Dickinson and L. Pauling. THE CRYSTAL STRUCTURE OF MOLYBDENITE. *Journal of the American Chemical Society*, 45(6):1466–1471, 1923.

[49] K. F. Mak, C. Lee, J. Hone, J. Shan, and T. F. Heinz. Atomically thin MoS_2: A new direct-gap semiconductor. *Physical Review Letters*, 105(13):1–4, 2010.

[50] A. Splendiani, L. Sun, Y. Zhang, T. Li, J. Kim, C.-Y. Chim, G. Galli, and F. Wang. Emerging photoluminescence in monolayer MoS_2. *Nano Letters*, 10(4):1271–1275, 2010.

[51] B. Radisavljevic, A. Radenovic, J. Brivio, V. Giacometti, and A. Kis. Single-layer MoS2 transistors. *Nature Nanotechnology*, 6(3):147–150, 2011.

[52] Y. Hu, Y. Huang, C. Tan, X. Zhang, Q. Lu, M. Sindoro, X. Huang, W. Huang, L. Wang, and H. Zhang. Two-dimensional transition metal dichalcogenide nanomaterials for biosensing applications. *Mater. Chem. Front.*, 1(1):24–36, 2017.

[53] Y.-P. Gao, X. Wu, K.-J. Huang, L.-L. Xing, Y.-Y. Zhang, and L. Liu. Two-dimensional transition metal diseleniums for energy storage application: a review of recent developments. *CrystEngComm*, 19(3):404–418, 2017.

[54] K. Thakar and S. Lodha. Optoelectronic and photonic devices based on transition metal dichalcogenides. *Materials Research Express*, 7(1):1–25, 2020.

[55] N. Huo and G. Konstantatos. Ultrasensitive all-2D MoS_2 phototransistors enabled by an out-of-plane MoS_2 PN homojunction. *Nature Communications*, 8(1):1–6, 2017.

[56] E. Lee, Y. S. Yoon, and D.-J. Kim. Two-dimensional transition metal dichalcogenides and metal oxide hybrids for gas sensing. *ACS Sensors*, 3(10):2045–2060, 2018.

[57] D. Voiry, J. Yang, and M. Chhowalla. Recent strategies for improving the catalytic activity of 2D TMD nanosheets toward the hydrogen evolution reaction. *Advanced Materials*, 28(29):6197–6206, 2016.

[58] N., M. Gibertini, P. Schwaller, D. Campi, A. Merkys, A. Marrazzo, T. Sohier, I. E. Castelli, A. Cepellotti, G. Pizzi, and N. Marzari. Two-dimensional materials from high-throughput computational exfoliation of experimentally known compounds. *Nature Nanotechnology*, 13(3):246–252, 2018.

[59] K. E. Dungey, M. D. Curtis, and J. E. Penner-Hahn. Structural characterization and thermal stability of MoS_2 intercalation compounds. *Chemistry of Materials*, 10(8):2152–2161, 1998.

[60] Y. Ding, Y. Wang, J. Ni, L. Shi, S. Shi, and W. Tang. First principles study of structural, vibrational and electronic properties of graphene-like MX_2 (M=Mo, Nb, W, Ta, X=S, Se, Te) monolayers. *Physica B: Condensed Matter*, 406(11):2254–2260, 2011.

[61] C. Ataca, H. Şahin, and S. Ciraci. Stable, single-layer MX_2 transition-metal oxides and dichalcogenides in a honeycomb-like structure. *The Journal of Physical Chemistry C*, 116(16):8983–8999, 2012.

[62] D. Voiry, A. Mohite, and M. Chhowalla. Phase engineering of transition metal dichalcogenides. *Chemical Society Reviews*, 44(9):2702–2712, 2015.

[63] Z. Lei, J. Zhan, L. Tang, Y. Zhang, and Y. Wang. Recent development of metallic (1T) phase of molybdenum disulfide for energy conversion and storage. *Advanced Energy Materials*, 8(19):1–29, 2018.

[64] A. Kuc and T. Heine. The electronic structure calculations of two-dimensional transition-metal dichalcogenides in the presence of external electric and magnetic fields. *Chemical Society Reviews*, 44(9):2603–2614, 2015.

[65] A. Kuc, N. Zibouche, and T. Heine. Influence of quantum confinement on the electronic structure of the transition metal sulfide TS_2. *Physical Review B*, 83(24):1–4, 2011.

[66] A. Kormányos, G. Burkard, M. Gmitra, J. Fabian, V. Zólyomi, N. D. Drummond, and V. Fal'ko. kůp theory for two-dimensional transition metal dichalcogenidesemiconductors. *2D Materials*, 2(2):1–31, 2015.

[67] D. Pasquier and O. V. Yazyev. Crystal field, ligand field, and interorbital effects in two-dimensional transition metal dichalcogenides across the periodic table. *2D Materials*, 6(2):1–16, 2019.

[68] H. He, P. Lu, L. Wu, C. Zhang, Y. Song, P. Guan, and S. Wang. Structural properties and phase transition of na adsorption on monolayer MoS_2. *Nanoscale Research Letters*, 11(1):1–8, 2016.

[69] H. Zeng and X. Cui. An optical spectroscopic study on two-dimensional group-VI transition metal dichalcogenides. *Chemical Society Reviews*, 44(9):2629–2642, 2015.

[70] Z. Y. Zhu, Y. C. Cheng, and U. Schwingenschlögl. Giant spin-orbit-induced spin splitting in two-dimensional transition-metal dichalcogenide semiconductors. *Physical Review B*, 84(15):1–5, 2011.

[71] C. Zhang, C. Gong, Y. Nie, K.-A. Min, C. Liang, Y. J. Oh, H. Zhang, W. Wang, S. Hong, L. Colombo, R. M. Wallace, and K. Cho. Systematic study of electronic structure and band alignment of monolayer transition metal dichalcogenides in van der Waals heterostructures. *2D Materials*, 4(1):1–10, 2016.

[72] S. K. Mahatha, K. D. Patel, and K. S. R. Menon. Electronic structure investigation of MoS_2 and $MoSe_2$ using angle-resolved photoemission spectroscopy and ab initio band structure studies. *Journal of Physics: Condensed Matter*, 24(47):1–5, 2012.

[73] A. Arora, K. Nogajewski, M. Molas, M. Koperski, and M. Potemski. Exciton band structure in layered $MoSe_2$: from a monolayer to the bulk limit. *Nanoscale*, 7(48):20769–20775, 2015.

[74] W. Zhao, Z. Ghorannevis, L. Chu, M. Toh, C. Kloc, P.-H. Tan, and Go. Eda. Evolution of electronic structure in atomically thin sheets of WS_2 and WSe_2. *ACS Nano*, 7(1):791–797, 2012.

[75] E. Cappelluti, R. Roldán, J. A. Silva-Guillén, P. Ordejón, and F. Guinea. Tight-binding model and direct-gap/indirect-gap transition in single-layer and multilayer MoS_2. *Physical Review B*, 88(7):1–18, 2013.

[76] J. Silva-Guillén, P. San-Jose, and R. Roldán. Electronic band structure of transition metal dichalcogenides from ab initio and slater–koster tight-binding model. *Applied Sciences*, 6(10):1–14, 2016.

[77] K. Kośmider and J. Fernández-Rossier. Electronic properties of the MoS_2/WS_2 heterojunction. *Physical Review B*, 87(7):1–4, 2013.

[78] K. Kośmider, J. W. González, and J. Fernández-Rossier. Large spin splitting in the conduction band of transition metal dichalcogenide monolayers. *Physical Review B*, 88(24):1–7, 2013.

[79] D. Xiao, G.-B. Liu, W. Feng, X. Xu, and W. Yao. Coupled spin and valley physics in monolayers of $MoS_2$and other group-VI dichalcogenides. *Physical Review Letters*, 108(19):1–5, 2012.

[80] A. Kormányos, V. Zólyomi, N. D. Drummond, P. Rakyta, G. Burkard, and V. I. Fal'ko. Monolayer MoS_2: Trigonal warping, the γ valley, and spin-orbit coupling effects. *Phys. Rev. B*, 88:1–8, 2013.

[81] M. A. U. Absor, H. Kotaka, F. Ishii, and M. Saito. Strain-controlled spin splitting in the conduction band of monolayer WS_2. *Physical Review B*, 94(11):1–6, 2016.

[82] M. Koperski, M. R. Molas, A. Arora, K. Nogajewski, A. O. Slobodeniuk, C. Faugeras, and M. Potemski. Optical properties of atomically thin transition metal dichalcogenides: observations and puzzles. *Nanophotonics*, 6(6):1289–1308, 2017.

[83] X. Xu, W. Yao, D. Xiao, and T. F. Heinz. Spin and pseudospins in layered transition metal dichalcogenides. *Nature Physics*, 10(5):343–350, 2014.

[84] T. Cao, G. Wang, W. Han, H. Ye, C. Zhu, J. Shi, Q. Niu, P. Tan, E. Wang, B. Liu, and J. Feng. Valley-selective circular dichroism of monolayer molybdenum disulphide. *Nature Communications*, 3(1):1–5, 2012.

[85] J. R. Schaibley, H. Yu, Ge. Clark, P. Rivera, J. S. Ross, K. L. Seyler, W. Yao, and X. Xu. Valleytronics in 2D materials. *Nature Reviews Materials*, 1(11):1–15, 2016.

[86] A. M. Jones, H. Yu, N. J. Ghimire, S. Wu, G. Aivazian, J. S. Ross, B. Zhao, J. Yan, D. G. Mandrus, D. Xiao, W. Yao, and J. Xu. Optical generation of excitonic valley coherence in monolayer WSe_2. *Nature Nanotechnology*, 8(9):634–638, 2013.

[87] R. Naaman and D. H. Waldeck. Spintronics and chirality: Spin selectivity in electron transport through chiral molecules. *Annual Review of Physical Chemistry*, 66(1):263–281, 2015.

[88] S. Wu, C. Huang, G. Aivazian, J. S. Ross, D. H. Cobden, and X. Xu. Vapor-solid growth of high optical quality MoS_2 monolayers with near-unity valley polarization. *ACS Nano*, 7(3):2768–2772, 2013.

[89] Yi. Jiang, S. Chen, W. Zheng, B. Zheng, and A. Pan. Interlayer exciton formation, relaxation, and transport in TMD van der waals heterostructures. *Light: Science & Applications*, 10(1), 2021.

[90] A. Surrente, Ł. Kłopotowski, N. Zhang, M. Baranowski, A. A. Mitioglu, M. V. Ballottin, P. C.M. Christianen, D. Dumcenco, Y.-C. Kung, D. K. Maude, A. Kis, and P. Plochocka. Intervalley scattering of interlayer excitons in a $MoS_2/MoSe_2/MoS_2$ heterostructure in high magnetic field. *Nano Letters*, 18(6):3994–4000, 2018.

[91] M. Manca, M. M. Glazov, C. Robert, F. Cadiz, T. Taniguchi, K. Watanabe, E. Courtade, T. Amand, P. Renucci, X. Marie, G. Wang, and B. Urbaszek. Enabling

valley selective exciton scattering in monolayer WSe_2 through upconversion. *Nature Communications*, 8(1):1–7, 2017.

[92] D. Lagarde, L. Bouet, X. Marie, C. R. Zhu, B. L. Liu, T. Amand, P. H. Tan, and B. Urbaszek. Carrier and polarization dynamics in monolayer MoS_2. *Physical Review Letters*, 112(4):1–5, 2014.

[93] A. T. Hanbicki, K. M. McCreary, G. Kioseoglou, M. Currie, C. S. Hellberg, A. L. Friedman, and B. T. Jonker. High room temperature optical polarization due to spin-valley coupling in monolayer WS_2. *AIP Advances*, 6(5):1–7, 2016.

[94] G. Sallen, L. Bouet, X. Marie, G. Wang, C. R. Zhu, W. P. Han, Y. Lu, P. H. Tan, T. Amand, B. L. Liu, and B. Urbaszek. Robust optical emission polarization in MoS_2 monolayers through selective valley excitation. *PRB*, 86(8):1–4, 2012.

[95] S. Morozov, T. Yezekyan, C. Wolff, S. I. Bozhevolnyi, and N. A. Mortensen. Inducing room-temperature valley polarization of excitonic emission in transition metal dichalcogenide monolayers, 2023.

[96] A. Carvalho, R. M. Ribeiro, and A. H. Castro Neto. Band nesting and the optical response of two-dimensional semiconducting transition metal dichalcogenides. *Physical Review B*, 88(11):1–6, 2013.

[97] D. Kozawa, R. Kumar, A. Carvalho, K. K. Amara, We. Zhao, S. Wang, M. Toh, R. M. Ribeiro, A. H. Castro Neto, K. Matsuda, and G. Eda. Photocarrier relaxation pathway in two-dimensional semiconducting transition metal dichalcogenides. *Nature Communications*, 5(1):1–7, 2014.

[98] W. Zhao, R. M. Ribeiro, and G. Eda. Electronic structure and optical signatures of semiconducting transition metal dichalcogenide nanosheets. *Accounts of Chemical Research*, 48(1):91–99, 2014.

[99] B. Peng, P. Kailian Ang, and K. Ping Loh. Two-dimensional dichalcogenides for light-harvesting applications. *Nano Today*, 10(2):128–137, apr 2015.

[100] J. Even, L. Pedesseau, J.-M. Jancu, and C. Katan. Importance of spin-orbit coupling in hybrid organic/inorganic perovskites for photovoltaic applications. *The Journal of Physical Chemistry Letters*, 4(17):2999–3005, 2013.

[101] L. V. Keldysh. Coulomb interaction in thin semiconductor and semimetal films. *SovietJournal of Experimental and Theoretical Physics Letters*, 29:658–660, 1979.

[102] E. Hanamura, N. Nagaosa, M. Kumagai, and T. Takagahara. Quantum wells with enhanced exciton effects and optical non-linearity. *Materials Science and Engineering: B*, 1(3-4):255–258, 1988.

[103] S. Tarucha, H. Okamoto, Y. Iwasa, and N. Miura. Exciton binding energy in GaAs quantum wells deduced from magneto-optical absorption measurement. *Solid State Communications*, 52(9):815–819, 1984.

[104] R. Cingolani, L. Calcagnile, G. Colí, R. Rinaldi, M. Lomoscolo, M. DiDio, A. Franciosi, L. Vanzetti, G. C. LaRocca, and D. Campi. Radiative recombination processes in wide-band-gap II/VI quantum wells: the interplay between excitons and free carriers. *Journal of the Optical Society of America B*, 13(6):1–10, 1996.

[105] H. M. Hill, A. F. Rigosi, C. Roquelet, A. Chernikov, T. C. Berkelbach, D. R. Reichman, M. S. Hybertsen, L. E. Brus, and T. F. Heinz. Observation of excitonic Rydberg states in monolayer MoS_2 and WS_2 by photoluminescence excitation spectroscopy. *Nano Letters*, 15(5):2992–2997, 2015.

[106] G. Gupta, S. Kallatt, and K. Majumdar. Direct observation of giant binding energy modulation of exciton complexes in monolayer MoS_2. *Physical Review B*, 96(8):1–5, 2017.

[107] K. He, N. Kumar, L. Zhao, Z. Wang, K. F. Mak, H. Zhao, and J. Shan. Tightly bound excitons in monolayer WSe_2. *Physical Review Letters*, 113(2):1–5, 2014.

[108] A. Raja, L. Waldecker, J. Zipfel, Y. Cho, S. Brem, J. D. Ziegler, M. Kulig, T. Taniguchi, K. Watanabe, E. Malic, T. F. Heinz, T. C. Berkelbach, and A. Chernikov. Dielectric disorder in two-dimensional materials. *Nature Nanotechnology*, 14(9):832–837, 2019.

[109] S. Latini, T. Olsen, and K. S. Thygesen. Excitons in van der Waals heterostructures: The important role of dielectric screening. *Physical Review B*, 92(24):1–13, 2015.

[110] P. Cudazzo, I. V. Tokatly, and A. Rubio. Dielectric screening in two-dimensional insulators: Implications for excitonic and impurity states in graphane. *Physical Review B*, 84(8):1–7, 2011.

[111] N. S. Rytova. Screened potential of a point charge in a thin film. 1967.

[112] T. C. Berkelbach, M. S. Hybertsen, and D. R. Reichman. Theory of neutral and charged excitons in monolayer transition metal dichalcogenides. *Physical Review B*, 88(4):1–6, 2013.

[113] A. V. Stier, K. M. McCreary, B. T. Jonker, J. Kono, and S. A. Crooker. Exciton diamagnetic shifts and valley zeeman effects in monolayer WS_2 and MoS_2 to 65 Tesla. *Nature Communications*, 7(1):1–8, 2016.

[114] Y. Lin, X. Ling, L. Yu, S. Huang, A. L. Hsu, Y.-H. Lee, J. Kong, M. S. Dresselhaus, and T. Palacios. Dielectric screening of excitons and trions in single-layer MoS_2. *Nano Letters*, 14(10):5569–5576, 2014.

[115] M. Goryca, J. Li, A. V. Stier, T. Taniguchi, K. Watanabe, E. Courtade, S. Shree, C. Robert, B. Urbaszek, X. Marie, and S. A. Crooker. Revealing exciton masses and dielectric properties of monolayer semiconductors with high magnetic fields. *Nature Communications*, 10(1):1–12, 2019.

[116] J. Hong, Z. Hu, M. Probert, K. Li, Danhui, X. Yang, L. Gu, N. Mao, Q. Feng, L. Xie, J. Zhang, D. Wu, Z. Zhang, C. Jin, W. Ji, X. Zhang, J. Yuan, and Z. Zhang. Exploring atomic defects in molybdenum disulphide monolayers. *Nature Communications*, 6(1):1–8, 2015.

[117] D. Han, W. Ming, H. Xu, S. Chen, D. Sun, and M.-H. Du. Chemical trend of transition-metal doping in WSe_2. *Physical Review Applied*, 12(3):1–9, 2019.

[118] K. F. Mak, K. He, C. Lee, G. H. Lee, J. Hone, T. F. Heinz, and J. Shan. Tightly bound trions in monolayer MoS_2. *Nature Materials*, 12(3):207–211, 2012.

[119] H. Qiu, T. Xu, Z. Wang, W. Ren, H. Nan, Z. Ni, Q. Chen, S. Yuan, F. Miao, F. Song, G. Long, Y. Shi, L. Sun, J. Wang, and X. Wang. Hopping transport through defect-induced localized states in molybdenum disulphide. *Nature Communications*, 4(1), 2013.

[120] A. A. Mitioglu, P. Plochocka, J. N. Jadczak, W. Escoffier, G. L. J. A. Rikken, L. Kulyuk, and D. K. Maude. Optical manipulation of the exciton charge state in single-layer tungsten disulfide. *Physical Review B*, 88(24):1–5, 2013.

[121] K. Kheng, R. T. Cox, Merle Y. d' Aubigné, Franck Bassani, K. Saminadayar, and S. Tatarenko. Observation of negatively charged excitons X^- in semiconductor quantum wells. *Physical Review Letters*, 71(11):1752–1755, 1993.

[122] A. Esser, E. Runge, R. Zimmermann, and W. Langbein. Photoluminescence and radiative lifetime of trions in GaAs quantum wells. *Physical Review B*, 62(12):8232–8239, 2000.

[123] J. S. Ross, S. Wu, H. Yu, N. J. Ghimire, A. M. Jones, G. Aivazian, J. Yan, D. G. Mandrus, D. Xiao, W. Yao, and X. Xu. Electrical control of neutral and charged excitons in a monolayer semiconductor. *Nature Communications*, 4(1):1–6, 2013.

[124] C. Zeng, J. Zhong, Y.-P. Wang, J. Yu, L. Cao, Z. Zhao, J. Ding, C. Cong, X. Yue, Z. Liu, and Y. Liu. Observation of split defect-bound excitons in twisted WSe2/WSe2 homostructure. *Applied Physics Letters*, 117(15), 2020.

[125] J. Kopaczek, S. Zelewski, K. Yumigeta, R. Sailus, S. Tongay, and R. Kudrawiec. Temperature dependence of the indirect gap and the direct optical transitions at the high-symmetry point of the brillouin zone and band nesting in MoS_2, $MoSe_2$, $MoTe_2$, WS_2, and WSe_2 crystals. *The Journal of Physical Chemistry C*, 126(12):5665–5674, 2022.

[126] C. Kastl, R. J. Koch, C. T. Chen, J. Eichhorn, S. Ulstrup, A. Bostwick, C. Jozwiak, T. R. Kuykendall, N. J. Borys, F. M. Toma, S. Aloni, A. Weber-Bargioni, E. Rotenberg, and A. M. Schwartzberg. Effects of defects on band structure and excitons in WS_2 revealed by nanoscale photoemission spectroscopy. *ACS Nano*, 2019.

[127] T. Verhagen, V. L. P. Guerra, G. Haider, M. Kalbac, and J. Vejpravova. Towards the evaluation of defects in MoS_2 using cryogenic photoluminescence spectroscopy. *Nanoscale*, 12(5):3019–3028, 2020.

[128] J. Long, L. Yang, and X. Wei. Lattice, elastic properties and debye temperatures of ATiO3 (A=Ba, Ca, Pb, Sr) from first-principles. *Journal of Alloys and Compounds*, 549:336–340, 2013.

[129] H. F. Kay and P. C. Bailey. Structure and properties of $CaTiO_3$. *Acta Crystallographica*, 10(3):219–226, 1957.

[130] B. Jaffe, R.S. Roth, and S. Marzullo. Properties of piezoelectric ceramics in the solid-solution series lead titanate-lead zirconate-lead oxide: Tin oxide and lead titanate-lead hafnate. *Journal of Research of the National Bureau of Standards*, 55(5):239–254, 1955.

[131] S. Zhang, C. A. Randall, and T. R. Shrout. High curie temperature piezocrystals in the $BiScO_3$-$PbTiO_3$ perovskite system. *Applied Physics Letters*, 83(15):3150–3152, 2003.

[132] Y. Yuan, Z. Xiao, B. Yang, and J. Huang. Arising applications of ferroelectric materials in photovoltaic devices. *J. Mater. Chem. A*, 2(17):6027–6041, 2014.

[133] D. Weber. $CH_3NH_3PbX_3$, ein Pb(II)-system mit kubischer perowskitstruktur / $CH_3NH_3PbX_3$, a Pb(II)-system with cubic perovskite structure. *Zeitschrift für Naturforschung B*, 33(12):1443–1445, 1978.

[134] A. Kojima, K. Teshima, Y. Shirai, and T. Miyasaka. Organometal halide perovskites as visible-light sensitizers for photovoltaic cells. *Journal of the American Chemical Society*, 131(17):6050–6051, 2009.

[135] M. A. Green, E. D. Dunlop, J. Hohl-Ebinger, M. Yoshita, N. Kopidakis, and A. W. Y. Ho-Baillie. Solar cell efficiency tables. *Progress in Photovoltaics: Research and Applications*, 28(1):3–15, 2019.

[136] A. K. Jena, A. Kulkarni, and T. Miyasaka. Halide perovskite photovoltaics: Background, status, and future prospects. *Chemical Reviews*, 119(5):3036–3103, 2019.

[137] Q. Zhang, Q. Shang, R. Su, T. T. H. Do, and Q. Xiong. Halide perovskite semiconductor lasers: Materials, cavity design, and low threshold. *Nano Letters*, 21(5):1903–1914, 2021.

[138] Y. Li, P. Zhang, D. Wan, C. Xue, J. Zhao, and G. Shao. Direct evidence of 2d/1d heterojunction enhancement on photocatalytic activity through assembling MoS_2 nanosheets onto super-long TiO_2 nanofibers. *Applied Surface Science*, 504:1–10, 2020.

[139] G. Grinblat, I. Abdelwahab, Mi. P. Nielsen, P. Dichtl, K. Leng, R. F. Oulton, K. P. Loh, and S. A. Maier. Ultrafast all-optical modulation in 2D hybrid perovskites. *ACS Nano*, 13(8):9504–9510, 2019.

[140] C. C. Stoumpos, D. H. Cao, D. J. Clark, J. Young, J. M. Rondinelli, J. I. Jang, J. T. Hupp, and M. G. Kanatzidis. Ruddlesden-Popper hybrid lead iodide perovskite 2D homologous semiconductors. *Chemistry of Materials*, 28(8):2852–2867, 2016.

[141] Y. I. Dolzhenko, T. Inabe, and Y. Maruyama. In situ x-ray observation on the intercalation of weak interaction molecules into perovskite-type layered crystals $(C_9H_{19}NH_3)_2PbI_4$ and $(C_{10}H_{21}NH_3)_2CdCl_4$. *Bulletin of the Chemical Society of Japan*, 59(2):563–567, 1986.

[142] X. Gao, X. Zhang, W. Yin, H. Wang, Y. Hu, Q. Zhang, Z. Shi, V. L. Colvin, W. W. Yu, and Y. Zhang. Ruddlesden-Popper perovskites: Synthesis and optical properties for optoelectronic applications. *Advanced Science*, 6(22):3–22, 2019.

[143] E. Jokar, P.-Y. Cheng, C.-Y. Lin, S. Narra, S. Shahbazi, and E. W.-G. Diau. Enhanced performance and stability of 3D/2D tin perovskite solar cells fabricated with a sequential solution deposition. *ACS Energy Letters*, 6(2):485–492, 2021.

[144] Y. Liu, S. Akin, L. Pan, R. Uchida, N. Arora, J. V. Milić, A. Hinderhofer, F. Schreiber, A. R. Uhl, S. M. Zakeeruddin, A. Hagfeldt, M. I. Dar, and M. Grätzel. Ultrahydrophobic 3D/2D fluoroarene bilayer-based water-resistant perovskite solar cells with efficiencies exceeding 22%. *Science Advances*, 5(6):1–8, 2019.

[145] Y.-H. Kim, S. Kim, A. Kakekhani, J. Park, J. Park, Y.-H. Lee, H. Xu, S. Nagane, R. B. Wexler, D.-H. Kim, S. H. Jo, L. Martínez-Sarti, P. Tan, A. Sadhanala, G.-S. Park, Y.-W. Kim, B. Hu, H. J. Bolink, S. Yoo, R. H. Friend, A. M. Rappe, and T.-W. Lee. Comprehensive defect suppression in perovskite nanocrystals for high-efficiency light-emitting diodes. *Nature Photonics*, 15(2):148–155, 2021.

[146] A. Kostopoulou, K. Brintakis, N. K. Nasikas, and E. Stratakis. Perovskite nanocrystals for energy conversion and storage. *Nanophotonics*, 8(10):1607–1640, 2019.

[147] W. Sun, Y. Liu, G. Qu, Y. Fan, W. Dai, Y. Wang, Q. Song, J. Han, and S. Xiao. Lead halide perovskite vortex microlasers. *Nature Communications*, 11(1):1–7, 2020.

[148] C. Li, H. Wang, F. Wang, Te. Li, M. Xu, H. Wang, Z. Wang, X. Zhan, W. Hu, and L. Shen. Ultrafast and broadband photodetectors based on a perovskite/organic bulk heterojunction for large-dynamic-range imaging. *Light: Science & Applications*, 9(1):1–8, 2020.

[149] W. Travis, E. N. K. Glover, H. Bronstein, D. O. Scanlon, and R. G. Palgrave. On the application of the tolerance factor to inorganic and hybrid halide perovskites: a revised system. *Chemical Science*, 7(7):4548–4556, 2016.

[150] B. Saparov and D. B. Mitzi. Organic/inorganic perovskites: Structural versatility for functional materials design. *Chemical Reviews*, 116(7):4558–4596, 2016.

[151] X. Li, W. Ke, Bo. Traoré, P. Guo, I. Hadar, M. Kepenekian, J. Even, C. Katan, C. C. Stoumpos, R. D. Schaller, and M. G. Kanatzidis. Two-dimensional dion-jacobson hybrid lead iodide perovskites with aromatic diammonium cations. *Journal of the American Chemical Society*, 141(32):12880–12890, 2019.

[152] D. B. Mitzi. Templating and structural engineering in organic-inorganic perovskites. *Journal of the Chemical Society, Dalton Transactions*, (1):1–12, 2001.

[153] C. Quarti, C. Katan, and J. Even. Physical properties of bulk, defective, 2D and 0D metal halide perovskite semiconductors from a symmetry perspective. *Journal of Physics: Materials*, 3(4):1–15, 2020.

[154] K.-Z. Du, Q. Tu, X. Zhang, Q. Han, J. Liu, S. Zauscher, and D. B. Mitzi. Two-dimensional lead(II) halide-based hybrid perovskites templated by acene alkylamines: Crystal structures, optical properties, and piezoelectricity. *Inorganic Chemistry*, 56(15):9291–9302, 2017.

[155] M. Menahem, Z. Dai, S. Aharon, R. Sharma, M. Asher, Y. Diskin-Posner, R. Korobko, A. M. Rappe, and O. Yaffe. Strongly anharmonic octahedral tilting in two-dimensional hybrid halide perovskites. *ACS Nano*, 15(6):10153–10162, 2021.

[156] D. B. Mitzi, K. Chondroudis, and C. R. Kagan. Design, structure, and optical properties of organic-inorganic perovskites containing an oligothiophene chromophore. *Inorganic Chemistry*, 38(26):6246–6256, 1999.

[157] K. Tanaka, T. Takahashi, T. Kondo, K. Umeda, K. Ema, T. Umebayashi, K. Asai, K. Uchida, and N. Miura. Electronic and excitonic structures of inorganic-organic perovskite-type quantum-well crystal $(C_4H_9NH_3)_2PbBr_4$. *Japanese Journal of Applied Physics*, 44(8):5923–5932, 2005.

[158] E. Mahal, S. C. Mandal, and B. Pathak. Understanding the role of spacer cation in 2D layered halide perovskites to achieve stable perovskite solar cells. *Materials Advances*, 3(5):2464–2474, 2022.

[159] L. Ma, J. Dai, and X. C. Zeng. Two-dimensional single-layer organic-inorganic hybrid perovskite semiconductors. *Advanced Energy Materials*, 7(7):1–5, 2016.

[160] W. Peng, J. Yin, K.-T. Ho, O. Ouellette, M. De Bastiani, B. Murali, O. El Tall, C. Shen, X. Miao, J. Pan, E. Alarousu, J.-H. He, B. S. Ooi, O. F. Mohammed, E. Sargent, and O. M. Bakr. Ultralow self-doping in two-dimensional hybrid perovskite single crystals. *Nano Letters*, 17(8):4759–4767, 2017.

[161] L. Zhang and W. Liang. How the structures and properties of two-dimensional layered perovskites $MAPbI_3$ and $CsPbI_3$ vary with the number of layers. *The Journal of Physical Chemistry Letters*, 8(7):1517–1523, 2017.

[162] R. A. DeCrescent, N. R. Venkatesan, C. J. Dahlman, R. M. Kennard, X. Zhang, W. Li, X. Du, M. L. Chabinyc, R. Zia, and J. A. Schuller. Bright magnetic dipole radiation from two-dimensional lead-halide perovskites. *Science Advances*, 6(6):1–11, 2020.

[163] T. Umebayashi, K. Asai, T. Kondo, and A. Nakao. Electronic structures of lead iodide-based low-dimensional crystals. *Physical Review B*, 67(15):1–6, 2003.

[164] J. Even, L. Pedesseau, M.-A. Dupertuis, J.-M. Jancu, and C. Katan. Electronic model for self-assembled hybrid organic/perovskite semiconductors: Reverse band edge electronic states ordering and spin-orbit coupling. *Physical Review B*, 86(20):1–4, 2012.

[165] L. Zhang, X. Zhang, and G. Lu. Intramolecular band alignment and spin-orbit coupling in two-dimensional halide perovskites. *The Journal of Physical Chemistry Letters*, 11(17):6982–6989, 2020.

[166] M. Dyksik, H. Duim, X. Zhu, Z. Yang, M. Gen, Y. Kohama, S. Adjokatse, D. K. Maude, M. A. Loi, D. A. Egger, M. Baranowski, and P. Plochocka. Broad tunability of carrier effective masses in two-dimensional halide perovskites. *ACS Energy Letters*, 5(11):3609–3616, 2020.

[167] T. Ishihara, J. Takahashi, and T. Goto. Optical properties due to electronic transitions in two-dimensional semiconductors $(C_nH_{2n+1}NH_3)_2PbI_4$. *Physical Review B*, 42(17):11099–11107, 1990.

[168] J.-C. Blancon, A. V. Stier, H. Tsai, W. Nie, C. C. Stoumpos, B. Traoré, L. Pedesseau, M. Kepenekian, F. Katsutani, G. T. Noe, J. Kono, S. Tretiak, S. A. Crooker, C. Katan, M. G. Kanatzidis, J. J. Crochet, J. Even, and A. D. Mohite. Scaling law for excitons in 2D perovskite quantum wells. *Nature Communications*, 9(1):1–10, 2018.

[169] Limeng Ni, Uyen Huynh, Alexandre Cheminal, Tudor H. Thomas, Ravichandran Shivanna, Ture F. Hinrichsen, Shahab Ahmad, Aditya Sadhanala, and Akshay Rao. Real-time observation of exciton phonon coupling dynamics in self-assembled hybrid perovskite quantum wells. *ACS Nano*, 11(11):10834–10843, 2017.

[170] M. Pandey, K. W. Jacobsen, and K. S. Thygesen. Band gap tuning and defect tolerance of atomically thin two-dimensional organic-inorganic halide perovskites. *The Journal of Physical Chemistry Letters*, 7(21):4346–4352, 2016.

[171] N. Kitazawa. Compositional modulation of two-dimensional layered perovskite $(RNH_3)_2Pb(Cl,Br,I)_4$ and its optical properties. *Japanese Journal of Applied Physics*, 35(Part 1, No. 12A):6202–6207, 1996.

[172] J. Di, H. Li, L. Chen, S. Zhang, Y. Hu, K. Sun, B. Peng, J. Su, X. Zhao, Y. Fan, Z. Lin, Y. Hao, P. Gao, K. Zhao, and J. Chang. Low trap density para-f substituted

2d PEA_2PbX_4 (X= Cl, Br, I) single crystals with tunable optoelectrical properties and high sensitive x-ray detector performance. *Research*, 2022:1–11, 2022.

[173] M. D. Smith, B. A. Connor, and H. I. Karunadasa. Tuning the luminescence of layered halide perovskites. *Chemical Reviews*, 119(5):3104–3139, 2019.

[174] D. B. Mitzi, C. D. Dimitrakopoulos, and L. L. Kosbar. Structurally tailored organic-inorganic perovskites: Optical properties and solution-processed channel materials for thin-film transistors. *Chemistry of Materials*, 13(10):3728–3740, 2001.

[175] Z. Xu, D. B. Mitzi, C. D. Dimitrakopoulos, and K. R. Maxcy. Semiconducting perovskites $(2\text{-}XC_6H_4C_2H_4NH_3)_2SnI_4$ (X = F, Cl, Br): Steric interaction between the organic and inorganic layers. *Inorganic Chemistry*, 42(6):2031–2039, 2003.

[176] J. L. Knutson, J. D. Martin, and D. B. Mitzi. Tuning the band gap in hybrid tin iodide perovskite semiconductors using structural templating. *Inorganic Chemistry*, 44(13):4699–4705, 2005.

[177] L. Pedesseau, D. Sapori, B. Traore, R. Robles, H.-H. Fang, M. A. Loi, H. Tsai, W. Nie, J.-C. Blancon, A. Neukirch, S. Tretiak, A. D. Mohite, C. Katan, J. Even, and M. Kepenekian. Advances and promises of layered halide hybrid perovskite semiconductors. *ACS Nano*, 10(11):9776–9786, 2016.

[178] D. G. Billing and A. Lemmerer. Synthesis, characterization and phase transitions in the inorganic-organic layered perovskite-type hybrids $[(C_nH_{2n+1}NH_3)_2PbI_4]$, n = 4, 5 and 6. *Acta Crystallographica Section B Structural Science*, 63(5):735–747, 2007.

[179] W. Paritmongkol, N. S. Dahod, A. Stollmann, N. Mao, C. Settens, S.-L. Zheng, and W. A. Tisdale. Synthetic variation and structural trends in layered two-dimensional alkylammonium lead halide perovskites. *Chemistry of Materials*, 31(15):5592–5607, 2019.

[180] J. Kang, S. Tongay, J. Zhou, J. Li, and J. Wu. Band offsets and heterostructures of two-dimensional semiconductors. *Applied Physics Letters*, 102(1):1–4, 2013.

[181] Y. Guo and J. Robertson. Band engineering in transition metal dichalcogenides: Stacked versus lateral heterostructures. *Applied Physics Letters*, 108(23):1–5, 2016.

[182] V. O. Özçelik, J. G. Azadani, C. Yang, S. J. Koester, and T. Low. Band alignment of two-dimensional semiconductors for designing heterostructures with momentum space matching. *Physical Review B*, 94(3):1–9, 2016.

[183] H.-P. Komsa and A. V. Krasheninnikov. Electronic structures and optical properties of realistic transition metal dichalcogenide heterostructures from first principles. *Physical Review B*, 88(8):1–7, 2013.

[184] M.-H. Chiu, C. Zhang, H.-W. Shiu, C.-P. Chuu, C.-H. Chen, C.-Y. S. Chang, C.-H. Chen, M.-Y. Chou, C.-K. Shih, and L.-J. Li. Determination of band alignment in the single-layer MoS_2/WSe_2 heterojunction. *Nature Communications*, 6(1):1–6, 2015.

[185] F. Ceballos, M.-G. Ju, S. D. Lane, X. C. Zeng, and H. Zhao. Highly efficient and anomalous charge transfer in van der Waals trilayer semiconductors. *Nano Letters*, 17(3):1623–1628, 2017.

[186] N. Zhang, A. Surrente, M. Baranowski, D. K. Maude, P. Gant, A. Castellanos-Gomez, and P. Plochocka. Moiré intralayer excitons in a $MoSe_2/MoS_2$ heterostructure. *Nano Letters*, 18(12):7651–7657, 2018.

[187] F. Ceballos, M. Z. Bellus, H.-Y. Chiu, and H. Zhao. Ultrafast charge separation and indirect exciton formation in a $MoS_2/MoSe_2$ van der Waals heterostructure. *ACS Nano*, 8(12):12717–12724, 2014.

[188] C. Robert, D. Lagarde, F. Cadiz, G. Wang, B. Lassagne, T. Amand, A. Balocchi, P. Renucci, S. Tongay, B. Urbaszek, and X. Marie. Exciton radiative lifetime in transition metal dichalcogenide monolayers. *Physical Review B*, 93(20):1–10, 2016.

[189] R. Long and O. V. Prezhdo. Quantum coherence facilitates efficient charge separation at a $MoS_2/MoSe_2$ van der Waals junction. *Nano Letters*, 16(3):1996–2003, feb 2016.

[190] H. Zhu, J. Wang, Z. Gong, Y. D. Kim, J. Hone, and X.-Y. Zhu. Interfacial charge transfer circumventing momentum mismatch at two-dimensional van der Waals heterojunctions. *Nano Letters*, 17(6):3591–3598, 2017.

[191] A. Marchioro, J. Teuscher, D. Friedrich, M. Kunst, R. van de Krol, T. Moehl, Mi. Grätzel, and J.-E. Moser. Unravelling the mechanism of photoinduced charge transfer processes in lead iodide perovskite solar cells. *Nature Photonics*, 8(3):250–255, 2014.

[192] P. Schulz, A.-M. Dowgiallo, Me. Yang, K. Zhu, J. L. Blackburn, and J. J. Berry. Charge transfer dynamics between carbon nanotubes and hybrid organic metal halide perovskite films. *The Journal of Physical Chemistry Letters*, 7(3):418–425, 2016.

[193] J. Zhang, X. Zhu, M. Wang, and B. Hu. Establishing charge-transfer excitons in 2D perovskite heterostructures. *Nature Communications*, 11(1):1–8, 2020.

[194] S. Mouri, W. Zhang, D. Kozawa, Y. Miyauchi, G. Eda, and K. Matsuda. Thermal dissociation of inter-layer excitons in $MoS_2/MoSe_2$ hetero-bilayers. *Nanoscale*, 9(20):6674–6679, 2017.

[195] S. Ovesen, S. Brem, C. Linderälv, M. Kuisma, T. Korn, P. Erhart, M. Selig, and E. Malic. Interlayer exciton dynamics in van der Waals heterostructures. *Communications Physics*, 2(1):1–8, 2019.

[196] I. C. Gerber, E. Courtade, S. Shree, C. Robert, T. Taniguchi, K. Watanabe, A. Balocchi, P. Renucci, D. Lagarde, X. Marie, and B. Urbaszek. Interlayer excitons in bilayer MoS_2 with strong oscillator strength up to room temperature. *Physical Review B*, 99(3):1–8, 2019.

[197] G. Wang, L. Bouet, D. Lagarde, M. Vidal, A. Balocchi, T. Amand, X. Marie, and B. Urbaszek. Valley dynamics probed through charged and neutral exciton emission in monolayer WSe_2. *Physical Review B*, 90(7):1–6, 2014.

[198] Z. Wang, D. A. Rhodes, K. Watanabe, T. Taniguchi, J. C. Hone, J. Shan, and K. F. Mak. Evidence of high-temperature exciton condensation in two-dimensional atomic double layers. *Nature*, 574(7776):76–80, 2019.

[199] B. Debnath, Y. Barlas, D. Wickramaratne, M. R. Neupane, and R. K. Lake. Exciton condensate in bilayer transition metal dichalcogenides: Strong coupling regime. *Physical Review B*, 96(17):1–8, 2017.

[200] Z. Wang, Y.-H. Chiu, K. Honz, K. F. Mak, and J. Shan. Electrical tuning of interlayer exciton gases in WSe_2 bilayers. *Nano Letters*, 18(1):137–143, 2017.

[201] A. Ciarrocchi, D. Unuchek, A. Avsar, K. Watanabe, T. Taniguchi, and A. Kis. Polarization switching and electrical control of interlayer excitons in two-dimensional van der Waals heterostructures. *Nature Photonics*, 13(2):131–136, 2019.

[202] L. A. Jauregui, A. Y. Joe, K. Pistunova, D. S. Wild, A. A. High, Y. Zhou, G. Scuri, K. De Greve, A. Sushko, C.-H. Yu, T. Taniguchi, K. Watanabe, D. J. Needleman, M. D. Lukin, H. Park, and P. Kim. Electrical control of interlayer exciton dynamics in atomically thin heterostructures. *Science*, 366(6467):870–875, 2019.

[203] D. Unuchek, A. Ciarrocchi, A. Avsar, Z. Sun, K. Watanabe, T. Taniguchi, and A. Kis. Valley-polarized exciton currents in a van der waals heterostructure. *Nature Nanotechnology*, 14(12):1104–1109, 2019.

[204] D. Kozawa, A. Carvalho, I. Verzhbitskiy, F. Giustiniano, Y. Miyauchi, S. Mouri, A. H. Castro Neto, K. Matsuda, and G. Eda. Evidence for fast interlayer energy transfer in $MoSe_2/WS_2$ heterostructures. *Nano Letters*, 16(7):4087–4093, 2016.

[205] G. Froehlicher, E. Lorchat, and S. Berciaud. Charge versus energy transfer in atomically thin graphene-transition metal dichalcogenide van der waals heterostructures. *Physical Review X*, 8(1):1–15, 2018.

[206] H. V. Demir S. V. Gaponenko. Energy transfer processes. In *Applied Nanophotonics,*, chapter Chapter 7, pages 210–226. Cambridge University Press, 2018.

[207] M. Li, J.-S. Chen, and M. Cotlet. Light-induced interfacial phenomena in atomically thin 2d van der Waals material hybrids and heterojunctions. *ACS Energy Letters*, 4(9):2323–2335, 2019.

[208] B. Guzelturk and H. V. Demir. Near-field energy transfer using nanoemitters for optoelectronics. *Advanced Functional Materials*, 26(45):8158–8177, 2016.

[209] Th. Förster. Transfer mechanisms of electronic excitation energy. *Radiation Research Supplement*, 2:326–339, 1960.

[210] W. Xu, D. Kozawa, Y. Liu, Y. Sheng, K. Wei, V. B. Koman, S. Wang, X. Wang, T. Jiang, M. S. Strano, and J. H. Warner. Determining the optimized interlayer separation distance in vertical stacked 2d WS_2 :hBN:MoS_2 heterostructures for exciton energy transfer. *Small*, 14(13):1–10, 2018.

[211] Z. Hu, X. Liu, P. L. Hernández-Martínez, S. Zhang, P. Gu, W. Du, W. Xu, H. V. Demir, H. Liu, and Q. Xiong. Interfacial charge and energy transfer in van der Waals heterojunctions. *InfoMat*, 4(3):1–22, 2022.

[212] C. Manolatou, H. Wang, W. Chan, S. Tiwari, and F. Rana. Radiative and nonradiative exciton energy transfer in monolayers of two-dimensional group-VI transition metal dichalcogenides. *Physical Review B*, 93(15):1–12, 2016.

[213] A. Tomita, J. Shah, and R. S. Knox. Efficient exciton energy transfer between widely separated quantum wells at low temperatures. *Physical Review B*, 53(16):10793–10803, apr 1996.

[214] D. L. Dexter. A theory of sensitized luminescence in solids. *The Journal of Chemical Physics*, 21(5):836–850, 1953.

[215] D. Rhodes, S. H. Chae, R. Ribeiro-Palau, and J. Hone. Disorder in van der waals heterostructures of 2D materials. *Nature Materials*, 18(6):541–549, 2019.

[216] F. Cadiz, C. Robert, G. Wang, W. Kong, X. Fan, M. Blei, D. Lagarde, M. Gay, M. Manca, T. Taniguchi, K. Watanabe, T. Amand, X. Marie, P. Renucci, S. Tongay, and B. Urbaszek. Ultra-low power threshold for laser-induced changes in optical properties of 2D molybdenum dichalcogenides. *2D Materials*, 3(4):1–8, 2016.

[217] C. R. Dean, A. F. Young, I. Meric, C. Lee, L. Wang, S. Sorgenfrei, K. Watanabe, T. Taniguchi, P. Kim, K. L. Shepard, and J. Hone. Boron nitride substrates for high-quality graphene electronics. *Nature nanotechnology*, 5:722–6, 2010.

[218] M. K. L. Man, S. Deckoff-Jones, A. Winchester, G. Shi, G. Gupta, A. D. Mohite, S. Kar, E. Kioupakis, S. Talapatra, and K. Dani. Protecting the properties of monolayer MoS_2 on silicon based substrates with an atomically thin buffer. 6(1):20890, 2016.

[219] X. Cui, G.-H. Lee, Y. D. Kim, G. Arefe, P. Y. Huang, C.-H. Lee, D. A. Chenet, X. Zhang, L. Wang, F. Ye, F. Pizzocchero, B. S. Jessen, K. Watanabe, T. Taniguchi, D. A. Muller, T. Low, P. Kim, and J. Hone. Multi-terminal transport measurements of MoS_2 using a van der waals heterostructure device platform. 10:534–40, 2015.

[220] Z. Li, T. Wang, S. Miao, Z. Lian, and S.-F. Shi. Fine structures of valley-polarized excitonic states in monolayer transitional metal dichalcogenides. *Nanophotonics*, 9(7):1811–1829, 2020.

[221] D. Vaclavkova, J. Wyzula, K. Nogajewski, M. Bartos, A. O. Slobodeniuk, C. Faugeras, M. Potemski, and M. R. Molas. Singlet and triplet trions in WS_2 monolayer encapsulated in hexagonal boron nitride. *Nanotechnology*, 29(32):1–6, 2018.

[222] A. Arora, T. Deilmann, T. Reichenauer, J. Kern, S. Michaelis de Vasconcellos, M. Rohlfing, and R. Bratschitsch. Excited-state trions in monolayer WS_2. *Physical Review Letters*, 123(16):1–6, 2019.

[223] T. Taniguchi and K. Watanabe. Synthesis of high-purity boron nitride single crystals under high pressure by using ba-BN solvent. *Journal of Crystal Growth*, 303(2):525–529, 2007.

[224] Y. Uchiyama, A. Kutana, K. Watanabe, T. Taniguchi, K. Kojima, T. Endo, Y. Miyata, H. Shinohara, and R. Kitaura. Momentum-forbidden dark excitons in hBN-encapsulated monolayer MoS_2. *npj 2D Materials and Applications*, 3(1):1–6, 2019.

[225] H.-H. Fang, J. Yang, S. Tao, S. Adjokatse, M. E. Kamminga, J. Ye, G. R. Blake, J. Even, and M. A. Loi. Unravelling light-induced degradation of layered perovskite crystals and design of efficient encapsulation for improved photostability. *Advanced Functional Materials*, 28(21):1–11, 2018.

[226] M. Seitz, P. Gant, A. Castellanos-Gomez, and F. Prins. Long-term stabilization of two-dimensional perovskites by encapsulation with hexagonal Boron Nitride. *Nanomaterials*, 9(8):1–10, 2019.

[227] M. E. Kamminga, H.-H. Fang, M. R. Filip, F. Giustino, J. Baas, G. R. Blake, M. A. Loi, and T. T. M. Palstra. Confinement effects in low-dimensional lead iodide perovskite hybrids. *Chem. Mater.*, 28(13):4554–4562, 2016.

[228] D.B. Mitzi. A layered solution crystal growth technique and the crystal structure of $(C_6H_5C_2H_4NH_3)_2PbCl_4$. *Journal of Solid State Chemistry*, 145(2):694–704, 1999.

[229] J. Zhou, J. Lin, X. Huang, Y. Zhou, Y. Chen, J. Xia, H. Wang, Y. Xie, H. Yu, J. Lei, D. Wu, F. Liu, Q. Fu, Q. Zeng, C.-H. Hsu, C. Yang, L. Lu, T. Yu, Z. Shen, H. Lin, B. I. Yakobson, Q. Liu, K. Suenaga, G. Liu, and Z. Liu. A library of atomically thin metal chalcogenides. *Nature*, 556(7701):355–359, 2018.

[230] D. B. Mitzi, C. A. Feild, W. T. A. Harrison, and A. M. Guloy. Conducting tin halides with a layered organic-based perovskite structure. *Nature*, 369(6480):467–469, 1994.

[231] J. D. Ziegler, J. Zipfel, B. Meisinger, M. Menahem, X. Zhu, T. Taniguchi, K. Watanabe, O. Yaffe, D. A. Egger, and A. Chernikov. Fast and anomalous exciton diffusion in two-dimensional hybrid perovskites. *Nano Lett.*, 20(9):6674–6681, 2020.

[232] D. B. Mitzi. Synthesis, crystal structure, and optical and thermal properties of $(C_4H_9NH_3)_2MI_4$ (M = Ge, Sn, Pb). *Chemistry of Materials*, 8(3):791–800, 1996.

[233] A. Castellanos-Gomez, L. Vicarelli, E. Prada, J. O. Island, K. L. Narasimha-Acharya, S. I. Blanter, D. J. Groenendijk, M. Buscema, G. A. Steele, J. V. Alvarez, H. W. Zandbergen, J. J. Palacios, and H. S. J. van der Zant. Isolation and characterization of few-layer black phosphorus. *2D Mater.*, 1(2):1–19, 2014.

[234] S. Hayashida, R. Saitoh, K. Watanabe, T. Taniguchi, K. Sawano, and Y. Hoshi. Reduced inhomogeneous broadening in hexagonal Boron Nitride-encapsulated $MoTe_2$ monolayers by thermal treatment. *ACS Appl. Electron. Mater.*, 2(9):2739–2744, 2020.

[235] R. Frisenda, Y. Niu, P. Gant, A. J. Molina-Mendoza, R. Schmidt, R. Bratschitsch, J. Liu, L. Fu, D. Dumcenco, A. Kis, D. P. De Lara, and A. Castellanos-Gomez. Micro-reflectance and transmittance spectroscopy: a versatile and powerful tool to characterize 2D materials. *Journal of Physics D: Applied Physics*, 50(7):1–8, 2017.

[236] Y. Li and T. F Heinz. Two-dimensional models for the optical response of thin films. *2D Materials*, 5(2):1–15, 2018.

[237] S. J. Orfanidis. *Electromagnetic Waves and Antennas*. Rutgers University, 2004.

[238] G. Plechinger, P. Nagler, A. Arora, R. Schmidt, A. Chernikov, A. G. del Águila, P. C. M. Christianen, R. Bratschitsch, C. Schüller, and T. Korn. Trion fine structure and coupled spin-valley dynamics in monolayer tungsten disulfide. *Nature Communications*, 7(1):1–9, 2016.

[239] Y. Cho and T. C. Berkelbach. Environmentally sensitive theory of electronic and optical transitions in atomically thin semiconductors. *Physical Review B*, 97(4):1–6, 2018.

[240] A. Laturia, M. L. Van de Put, and W. G. Vandenberghe. Author correction: Dielectric properties of hexagonal boron nitride and transition metal dichalcogenides: from monolayer to bulk. *2D Materials and Applications*, 4(1):1–4, 2020.

[241] B. Zhu, X. Chen, and X. Cui. Exciton binding energy of monolayer WS2. *Scientific Reports*, 5(1):1–5, 2015.

[242] X. Hong, T. Ishihara, and A. V. Nurmikko. Dielectric confinement effect on excitons in PbI_4-based layered semiconductors. *Physical Review B*, 45(12):6961–6964, 1992.

[243] X. Zhu, Z. Xu, S. Zuo, J. Feng, Z. Wang, X. Zhang, K. Zhao, J. Zhang, H. Liu, S. Priya, S. F. Liu, and D. Yang. Vapor-fumigation for record efficiency two-dimensional perovskite solar cells with superior stability. *Energy & Environmental Science*, 11(12):3349–3357, 2018.

[244] A. L. Powell and A. E. Martell. The properties of tetraethylammonium and tetra-n-butylammonium picrates in anisole-nitrobenzene solutions. *Journal of the American Chemical Society*, 79(9):2118–2123, 1957.

[245] S.-S. Chee, C. Oh, M. Son, G.-C. Son, H. Jang, T. J. Yoo, S. Lee, W. Lee, J. Y. Hwang, H. Choi, B. H. Lee, and M.-H. Ham. Sulfur vacancy-induced reversible doping of transition metal disulfides via hydrazine treatment. *Nanoscale*, 9(27):9333–9339, 2017.

[246] P. Nagler, M. V. Ballottin, A. A. Mitioglu, M. V. Durnev, T. Taniguchi, K. Watanabe, A. Chernikov, C. Schüller, M. M. Glazov, P. C. M. Christianen, and T. Korn. Zeeman splitting and inverted polarization of biexciton emission in monolayer WS_2. *Physical Review Letters*, 121(5):1–6, 2018.

[247] P. V. Kolesnichenko, Q. Zhang, T. Yun, C. Zheng, M. S. Fuhrer, and J. A. Davis. Disentangling the effects of doping, strain and disorder in monolayer WS_2 by optical spectroscopy. *2D Materials*, 7(2):1–11, 2020.

[248] S. Tongay, J. Suh, C. Ataca, W. Fan, A. Luce, J. S. Kang, J. Liu, C. Ko, R. Raghunathanan, J. Zhou, F. Ogletree, J. Li, J. C. Grossman, and J. Wu. Defects activated photoluminescence in two-dimensional semiconductors: interplay between bound, charged and free excitons. *Scientific Reports*, 3(1):1–5, 2013.

[249] M. R. Molas, K. Nogajewski, A. O. Slobodeniuk, J. Binder, M. Bartos, and M. Potemski. The optical response of monolayer, few-layer and bulk tungsten disulfide. *Nanoscale*, 9(35):13128–13141, 2017.

[250] J. Krustok, R. Kaupmees, R. Jaaniso, V. Kiisk, I. Sildos, B. Li, and Y. Gong. Local strain-induced band gap fluctuations and exciton localization in aged WS_2 monolayers. *AIP Advances*, 7(6):1–11, 2017.

[251] G. Moody, C. K. Dass, K. Hao, C.-H. Chen, L.-J. Li, A. Singh, K. Tran, G. Clark, X. Xu, G. Berghäuser, E. Malic, A. Knorr, and X. Li. Intrinsic homogeneous linewidth and broadening mechanisms of excitons in monolayer transition metal dichalcogenides. *Nature Communications*, 6(1):1–6, 2015.

[252] H. Liu, J. Lu, K. Ho, Z. Hu, Z. Dang, A. Carvalho, H. R. Tan, E. S. Tok, and C. H. Sow. Fluorescence concentric triangles: A case of chemical heterogeneity in WS_2 atomic monolayer. *Nano Letters*, 16(9):5559–5567, 2016.

[253] J. M. Urban, G. Chehade, M. Dyksik, M. Menahem, A. Surrente, G. Trippé-Allard, D. K. Maude, D. Garrot, O. Yaffe, E. Deleporte, P. Plochocka, and M. Baranowski. Revealing excitonic phonon coupling in $(PEA)_2(MA)_{n-1}PbnI_{3n-1}$ 2D layered perovskites. *The Journal of Physical Chemistry Letters*, 11(15):5830–5835, 2020.

[254] M. Dyksik, H. Duim, D. K. Maude, M. Baranowski, M. A. Loi, and P. Plochocka. Brightening of dark excitons in 2d perovskites. *Science Advances*, 7(46):1–7, 2021.

[255] K. Posmyk, N. Zawadzka, M. Dyksik, A. Surrente, D. K. Maude, T. Kazimierczuk, A. Babiński, M. R. Molas, W. Paritmongkol, M. Mączka, W. A. Tisdale, P. Płochocka, and M. Baranowski. Quantification of exciton fine structure splitting in a two-dimensional perovskite compound. *The Journal of Physical Chemistry Letters*, 13(20):4463–4469, 2022.

[256] J. D. Ziegler, Y. Cho, S. Terres, M. Menahem, T. Taniguchi, K. Watanabe, O. Yaffe, T. C. Berkelbach, and A. Chernikov. Mobile trions in electrically tunable 2D hybrid perovskites. *Advanced Materials*, 35(18):1–8, 2023.

[257] D. Ghosh, D. Acharya, L. Pedesseau, C. Katan, J. Even, S. Tretiak, and A. J. Neukirch. Charge carrier dynamics in two-dimensional hybrid perovskites: Dion-jacobson vs. ruddlesden-popper phases. *Journal of Materials Chemistry A*, 8(42):22009–22022, 2020.

[258] O. Yaffe, A. Chernikov, Z. M. Norman, Y. Zhong, A. Velauthapillai, A. van der Zande, J. S. Owen, and T. F. Heinz. Excitons in ultrathin organic-inorganic perovskite crystals. *Physical Review B*, 92(4):1–7, 2015.

[259] A. G. Ricciardulli, S. Yang, J. H. Smet, and M. Saliba. Emerging perovskite monolayers. *Nature Materials*, 20(10):1325–1336, 2021.

[260] H. Zahra, A. Hichri, and S. Jaziri. Comparative study of the exciton binding energies of thin and ultrathin organic-inorganic perovskites due to dielectric mismatch effects. *Journal of Applied Physics*, 122(1), 2017.

[261] F. Yang, M. Wilkinson, E. J. Austin, and K. P. O'Donnell. Origin of the stokes shift: A geometrical model of exciton spectra in 2D semiconductors. *Physical Review Letters*, 70(3):323–326, 1993.

[262] W. Tao, C. Zhang, Q. Zhou, Y. Zhao, and H. Zhu. Momentarily trapped exciton polaron in two-dimensional lead halide perovskites. *Nature Communications*, 12(1):1–8, 2021.

[263] Y. Guo, O. Yaffe, T. D. Hull, J. S. Owen, D. R. Reichman, and L. E. Brus. Dynamic emission stokes shift and liquid-like dielectric solvation of band edge carriers in lead-halide perovskites. *Nature Communications*, 10(1):1–8, 2019.

[264] D. B. Straus and C. R. Kagan. Electrons, excitons, and phonons in two-dimensional hybrid perovskites: Connecting structural, optical, and electronic properties. *The Journal of Physical Chemistry Letters*, 9(6):1434–1447, 2018.

[265] H.-H. Fang, J. Yang, S. Adjokatse, E. Tekelenburg, M. E. Kamminga, H. Duim, J. Ye, G. R. Blake, J. Even, and M. A. Loi. Band-edge exciton fine structure and exciton recombination dynamics in single crystals of layered hybrid perovskites. *Advanced Functional Materials*, 30(6):1–9, 2019.

[266] K. Lee, J. Kim, H. Yu, J. Woo Lee, C.-M. Yoon, S. K. Kim, and J. Jang. A highly stable and efficient carbon electrode-based perovskite solar cell achieved via interfacial growth of 2d PEA_2PbI_4 perovskite. *Journal of Materials Chemistry A*, 6(47):24560–24568, 2018.

[267] A. Arora, T. Deilmann, P. Marauhn, M. Drüppel, R. Schneider, M. R. Molas, D. Vaclavkova, S. M. de Vasconcellos, M. Rohlfing, M. Potemski, and R. Bratschitsch. Valley-contrasting optics of interlayer excitons in Mo- and W-based bulk transition metal dichalcogenides. *Nanoscale*, 10(33):15571–15577, 2018.

[268] G. Scuri, Y. Zhou, A. A. High, D. S. Wild, C. Shu, K. De Greve, L. A. Jauregui, T. Taniguchi, K. Watanabe, P. Kim, M. D. Lukin, and H. Park. Large excitonic reflectivity of monolayer $MoSe_2$ encapsulated in hexagonal boron nitride. *Physical Review Letters*, 120(3):1–6, 2018.

[269] E. Courtade, B. Han, S. Nakhaie, C. Robert, X. Marie, P. Renucci, T. Taniguchi, K. Watanabe, L. Geelhaar, J. M. J. Lopes, and B. Urbaszek. Spectrally narrow exciton luminescence from monolayer MoS_2 and $MoSe_2$ exfoliated onto epitaxially grown hexagonal BN. *Applied Physics Letters*, 113(3):1–5, 2018.

[270] T. Goldstein, Y.-C. Wu, S.-Y. Chen, T. Taniguchi, K. Watanabe, K. Varga, and J. Yan. Ground and excited state exciton polarons in monolayer $MoSe_2$. *The Journal of Chemical Physics*, 153(7):1–6, 2020.

[271] D. Beret, I. Paradisanos, H. Lamsaadi, Z. Gan, E. Najafidehaghani, A. George, T. Lehnert, J. Biskupek, U. Kaiser, S. Shree, A. Estrada-Real, D. Lagarde, X. Marie, P. Renucci, K. Watanabe, T. Taniguchi, S. Weber, V. Paillard, L. Lombez, J.-M. Poumirol, A. Turchanin, and B. Urbaszek. Exciton spectroscopy and unidirectional transport in mose2-wse2 lateral heterostructures encapsulated in hexagonal boron nitride. *npj 2D Materials and Applications*, 6(1):84, 2022.

[272] M. Li, S. Biswas, C. U. Hail, and H. A. Atwater. Refractive index modulation in monolayer molybdenum diselenide. *Nano Letters*, 21(18):7602–7608, 2021.

[273] F. Cadiz, E. Courtade, C. Robert, G. Wang, Y. Shen, H. Cai, T. Taniguchi, K. Watanabe, H. Carrere, D. Lagarde, M. Manca, T. Amand, P. Renucci, S. Tongay, X. Marie, and B. Urbaszek. Excitonic linewidth approaching the homogeneous limit in MoS_2 -based van der Waals heterostructures. *Phys. Rev. X*, 7(2):1–12, 2017.

[274] H. H. Fang, B. Han, C. Robert, M. A. Semina, D. Lagarde, E. Courtade, T. Taniguchi, K. Watanabe, T. Amand, B. Urbaszek, M. M. Glazov, and X. Marie. Control of the exciton radiative lifetime in van der waals heterostructures. *Physical Review Letters*, 123(6):1–6, 2019.

[275] J. Wierzbowski, J. Klein, F. Sigger, C. Straubinger, M. Kremser, T. Taniguchi, K. Watanabe, U. Wurstbauer, A. W. Holleitner, M. Kaniber, K. Müller, and J. J. Finley. Direct exciton emission from atomically thin transition metal dichalcogenide heterostructures near the lifetime limit. *Scientific Reports*, 7(1):1–6, 2017.

[276] E. V. Calman, L. H. Fowler-Gerace, D. J. Choksy, L. V. Butov, D. E. Nikonov, I. A. Young, S. Hu, A. Mishchenko, and A. K. Geim. Indirect excitons and trions in $mose_2/wse_2$ van der Waals heterostructures. *Nano Letters*, 20(3):1869–1875, 2020.

[277] O. A. Ajayi, J. V. Ardelean, G. D. Shepard, J. Wang, A. Antony, T. Taniguchi, K. Watanabe, T. F. Heinz, S. Strauf, X.-Y. Zhu, and J. C. Hone. Approaching the intrinsic photoluminescence linewidth in transition metal dichalcogenide monolayers. *2D Materials*, 4(3):283–288, 2017.

[278] T. Schmidt, K. Lischka, and W. Zulehner. Excitation-power dependence of the near-band-edge photoluminescence of semiconductors. *Physical Review B*, 45(16):8989–8994, 1992.

[279] N. Zhang, A. Surrente, M. Baranowski, D. Dumcenco, Y.-C. Kung, D. K. Maude, An. Kis, and P. Plochocka. Impact of photodoping on inter- and intralayer exciton emission in a $MoS_2/MoSe_2/MoS_2$ heterostructure. *Applied Physics Letters*, 113(6):1–5, 2018.

[280] D. B. Straus, S. Hurtado Parra, N. Iotov, J. Gebhardt, A. M. Rappe, J. E. Subotnik, J. M. Kikkawa, and C. R. Kagan. Direct observation of electron-phonon coupling and slow vibrational relaxation in organic-inorganic hybrid perovskites. *Journal of the American Chemical Society*, 138(42):13798–13801, 2016.

[281] C.-W. Lin, F. Liu, T.-Y. Chen, K.-H. Lee, C.-K. Chang, Y. He, T. L. Leung, A. M. Ching Ng, C.-H. Hsu, J. Popović, A. Djurišić, and H. Ahn. Structure-dependent photoluminescence in low-dimensional ethylammonium, propylammonium, and

butylammonium lead iodide perovskites. *ACS Applied Materials & Interfaces*, 12(4):5008–5016, 2019.

[282] A. Yang, J.-C. Blancon, Wei J., H. Zhang, J. Wong, E. Yan, Y.-R. Lin, J. Crochet, M. G. Kanatzidis, D. Jariwala, T. Low, A. D. Mohite, and H. A. Atwater. Giant enhancement of photoluminescence emission in WS_2-two-dimensional perovskite heterostructures. *Nano Letters*, 19(8):4852–4860, 2019.

[283] K. Persson. Materials data on WS_2 by Materials Project, 2016. An optional note.

[284] K. Momma and F. Izumi. VESTA or three-dimensional visualization of crystal, volumetric and morphology data. *Journal of Applied Crystallography*, 44(6):1272–1276, 2011.

[285] J. H. Park, A. Sanne, Y. Guo, M. Amani, K. Zhang, H. C. P. Movva, J. A. Robinson, A. Javey, J. Robertson, S. K. Banerjee, and A. C. Kummel. Defect passivation of transition metal dichalcogenides via a charge transfer van der waals interface. *Science Advances*, 3(10):1–6, 2017.

[286] Q. Liang, Q. Zhang, X. Zhao, M. Liu, and A. T. S. Wee. Defect engineering of two-dimensional transition-metal dichalcogenides: Applications, challenges, and opportunities. *ACS Nano*, 15(2):2165–2181, 2021.

[287] X. Sang, X. Li, W. Zhao, J. Dong, C. M. Rouleau, D. B. Geohegan, F. Ding, K. Xiao, and R. R. Unocic. In situ edge engineering in two-dimensional transition metal dichalcogenides. *Nature Communications*, 9(1):1–7, 2018.

[288] A. Branny, S. Kumar, R. Proux, and B. D. Gerardot. Deterministic strain-induced arrays of quantum emitters in a two-dimensional semiconductor. *Nature Communications*, 8(1):1–7, 2017.

[289] X. He, H. Li, Z. Zhu, Z. Dai, Y. Yang, P. Yang, Q. Zhang, P. Li, U. Schwingenschlogl, and X. Zhang. Strain engineering in monolayer WS_2, MoS_2, and the WS_2/MoS_2 heterostructure. *Applied Physics Letters*, 109(17):1–5, 2016.

[290] A. Castellanos-Gomez, R. Roldán, E. Cappelluti, M. Buscema, F. Guinea, H. S. J. van der Zant, and G. A. Steele. Local strain engineering in atomically thin MoS_2. *Nano Letters*, 13(11):5361–5366, 2013.

[291] H. Li, A. W. Contryman, X. Qian, S. M. Ardakani, Y. Gong, X. Wang, J. M. Weisse, C. H. Lee, J. Zhao, P. M. Ajayan, J. Li, H. C. Manoharan, and X. Zheng.

Optoelectronic crystal of artificial atoms in strain-textured molybdenum disulphide. *Nature Communications*, 6(1):1–6, 2015.

[292] Y. Wang, C. Cong, . Yang, J. Shang, N. Peimyoo, Y. Chen, J. Kang, J. Wang, W. Huang, and T. Yu. Strain-induced direct-indirect bandgap transition and phonon modulation in monolayer WS_2. *Nano Research*, 8(8):2562–2572, 2015.

[293] G. Wang, X. Marie, I. Gerber, T. Amand, D. Lagarde, L. Bouet, M. Vidal, A. Balocchi, and B. Urbaszek. Giant enhancement of the optical second-harmonic emission of WSe_2 monolayers by laser excitation at exciton resonances. *Physical Review Letters*, 114(9):1–6, 2015.

[294] I. Paradisanos, K. M. McCreary, D. Adinehloo, L. Mouchliadis, J. T. Robinson, Hsun-Jen Chuang, A. T. Hanbicki, V. Perebeinos, B. T. Jonker, E. Stratakis, and G. Kioseoglou. Prominent room temperature valley polarization in WS_2/graphene heterostructures grown by chemical vapor deposition. *Applied Physics Letters*, 116(20):1–6, 2020.

[295] W. Li, S. Yang, B. Guo, X. Fu, X. Zeng, C. Yan, J. Cao, Q. Wang, and W. Yang. Decoupling excitons behavior of two-dimensional ruddlesden-popper PEA_2PbI_4 nanosheets. *Journal of Alloys and Compounds*, 936:1–7, 2023.

[296] T. Krisnanda, Q. Zhang, K. Dini, D. Giovanni, T. C. H. Liew, and T. C. Sum. Room temperature light-mediated long-range coupling of excitons in perovskites. *Advanced Optical Materials*, 9(9):1–7, 2021.

[297] M. Ferrera, A. Sharma, I. Milekhin, Y. Pan, D. Convertino, S. Pace, G. Orlandini, E. Peci, L. Ramò, M. Magnozzi, C. Coletti, G. Salvan, D. R. T. Zahn, M. Canepa, and F. Bisio. Local dielectric function of hBN-encapsulated WS2 flakes grown by chemical vapor deposition. *Journal of Physics: Condensed Matter*, 35(27):1–8, 2023.

[298] The Materials Project. Materials data on $MoSe_2$ by Materials Project. 2020.

[299] C. Choi, J. Huang, H.-C. Cheng, H. Kim, A. K. Vinod, S.-H. Bae, V. O. Özçelik, R. Grassi, J. Chae, S.-W. Huang, X. Duan, K. Kaasbjerg, T. Low, and C. W. Wong. Enhanced interlayer neutral excitons and trions in trilayer van der Waals heterostructures. *2D Materials and Applications*, 2(1):1–9, 2018.

[300] L. Zhang, R. Gogna, G. William Burg, J. Horng, E. Paik, Y.-H. Chou, K. Kim, E. Tutuc, and H. Deng. Highly valley-polarized singlet and triplet interlayer excitons in van der waals heterostructure. *Physical Review B*, 100(4):1–6, 2019.

[301] P. Nagler, F. Mooshammer, J. Kunstmann, M. V. Ballottin, An. Mitioglu, A. Chernikov, A. Chaves, F. Stein, N. Paradiso, S. Meier, G. Plechinger, C. Strunk, R. Huber, G.Seifert, D. R. Reichman, P. C. M. Christianen, C. Schüller, and T. Korn. Interlayer excitons in transition-metal dichalcogenide heterobilayers. *Physica Status Solidi (b)*, 256(12):1–7, 2019.

[302] M. Baranowski, S. J. Zelewski, M. Kepenekian, B. Traoré, J. M. Urban, A. Surrente, K. Galkowski, D. K. Maude, A. Kuc, E. P. Booker, R. Kudrawiec, S. D. Stranks, and P. Plochocka. Phase-transition-induced carrier mass enhancement in 2D ruddlesden-popper perovskites. *ACS Energy Letters*, 4(10):2386–2392, 2019.

[303] B. Miller, A. Steinhoff, B. Pano, J. Klein, F. Jahnke, A. Holleitner, and U. Wurstbauer. Long-lived direct and indirect interlayer excitons in van der waals heterostructures. *Nano Letters*, 17(9):5229–5237, 2017.